

Justus Constantin Hildebrand

**Acid Mine Drainage and Tailing
Monitoring using Satellite Imagery
for VMS-type deposits in the
Republic of Cyprus**

Scientific Technical Report STR22/08

Recommended citation of the publication

Hildebrand, J. C. (2022): Acid Mine Drainage and Tailing Monitoring using Satellite Imagery for VMS-type deposits in the Republic of Cyprus, Master Thesis, (Scientific Technical Report STR; 22/08), Potsdam: GFZ German Research Centre for Geosciences.
<https://doi.org/10.48440/GFZ.b103-22083>

Imprint

Helmholtz Centre Potsdam
GFZ German Research Centre for Geosciences
Telegrafenberg
D-14473 Potsdam

Published in Potsdam, Germany
2022

DOI: <https://doi.org/10.48440/gfz.b103-22083>
URN: urn:nbn:de:kobv:b103-22083

This work is published in the GFZ series Scientific Technical Report STR and electronically available via our repository GFZpublic: <https://tinyurl.com/GFZ-ST-Reports>



This work is licensed under a Creative Commons Attribution 4.0 International License.
(CC BY 4.0) <https://creativecommons.org/licenses/by/4.0/>

Acid Mine Drainage and Tailing Monitoring using Satellite Imagery for VMS-type deposits in the Republic of Cyprus

Justus Constantin Hildebrand 

Masterarbeit

Zur Erlangung des akademischen Grades Master of Science

Thema der Arbeit

Acid Mine Drainage and Tailing Monitoring using Satellite Imagery for VMS-type deposits in the Republic of Cyprus

eingereicht von: Justus Constantin Hildebrand

Gutachter/innen: Prof. Dr. Dagmar Haase
Dr. Karl Segl

Eingereicht am Geographischen Institut der Humboldt-Universität zu Berlin

Table of contents

Table of contents.....	I
List of figures	III
List of tables.....	V
Abbreviations.....	VI
Acknowledgements	VII
Abstract	1
Zusammenfassung.....	2
1 Introduction.....	1
1.1 Motivation	1
1.2 State of the Art	4
1.2.1 Geology of mine tailings: Acid producing reactions.....	4
1.2.2 Geology of mine tailings: Formation of secondary iron minerals (SIMs)	6
1.2.2 Spectroscopy	10
1.2.3 Spectral response of surfaces and spectral features	12
1.2.4 Spectral identification of Minerals	14
1.2.5 Spectral Properties of iron minerals.....	14
1.2.6 Remote sensing indices	16
1.2.7 Research groups and predominant methodology.....	17
1.2.8 Research Objectives	19
2 Methods	20
2.1 Study region	20
2.1.1 Skouriotissa	22
2.1.2 Apliki.....	24
2.2 Study design	25
2.2.1 Data sampling.....	25
2.2.2 Data processing	32
2.3 Analyses.....	32
2.3.1 Overview of applied workflow	32
2.3.2 Detailed workflow description	34
3 Results	42
3.1 Accuracy Assessment of the RF-models.....	42
3.2 Classification of the Laboratory Field Sample Validation Mosaic	43
3.3 Classification of Satellite Field Data	49
4 Discussion	52

4.1 Quality and impacts of the SIM indices	52
4.1 Classification of the Laboratory Field Sample Validation Mosaic	53
4.2 Classification results of the Skouriotissa mining area	55
4.2.1 Phoenix	55
4.2.2 Phoukasa	55
4.2.3 Three Hills	56
4.2.4 Mine dumps.....	56
4.2.5 Field data from the Skouriotissa mine	57
4.3 Classification results of the Apliki mining area.....	59
4.4 Challenges and Implications.....	60
4.5 The use of different wavelength ranges: VNIR vs. SWIR.....	62
4.6 The use of data from different dates (WorldView-3).....	62
5 Conclusion	64
6 Outlook.....	66
6.1 Application on Sentinel Time series	66
7 Literature	67
8 Appendix.....	74
8.1 Further Methods	74
8.1.1 The HySpex camera system.....	74
8.1.2 Principle of X-ray diffractometry (XRD).....	76
8.1.3 XRD diffractograms of validation samples	77
8.2 Additional Datasets	82
8.3 Additional Data (Results).....	83
8.4 Additional Data (Outlook)	85

List of figures

Figure 1 Photo showing the aftermath of the Brumadinho dam burst. _____	2
Figure 2 Schematic of the so-called "AMD engine". _____	6
Figure 3 Overview of selected minerals and their pH-range occurrence. _____	7
Figure 4 Overview of the overall sequence of mineral reactions in pyrite oxidation. _____	7
Figure 5 Schematic representation of the band positions. _____	10
Figure 6 Jarosite spectra displayed in three different spectral resolutions. _____	11
Figure 7 Material specific reflectance spectra for selected minerals and vegetation. _____	13
Figure 8 Hyperspectral representation of the reflectance of various SIMs. _____	15
Figure 9 Stratigraphic cross-section of the Troodos ophiolite complex. _____	20
Figure 10 Geological map of the Troodos ophiolite showing locations of major sulphide deposits. _	21
Figure 11 Geological map of the Skouriotissa area. _____	22
Figure 12 Left: Position of the different samples in the mosaic. Abbreviations of the individual minerals, to be found in Table 4. Middle: RGB representation of the laboratory data set. Right: Color-coded differentiation by sample type. _____	25
Figure 13 Left: Short-names of the samples. Right: RGB representation of the samples in Mosaic. The samples named AM and KM come from the island of Cyprus. AM are from the Agropia mine and KM from the Kokkinopezoula mine. The samples beginning starting with L are from Lausitz, Germany. _____	26
Figure 14 RGB representation of the WorldView-3 satellite image. _____	29
Figure 15 RGB representation of the Sentinel-2A satellite image. _____	31
Figure 16 Overview of applied workflow. _____	33
Figure 17 Left: NDVI plot of the data set. Right: RGB image after the threshold masking. _____	34
Figure 18 Comparison of the calculated iron-indices. _____	35
Figure 19 Spectrum of a Jarosite mineral. _____	36
Figure 20 Iron Feature Band Ratio index. _____	36
Figure 21 Visualisation of the Laboratory Reference Sample Mosaic. _____	37
Figure 22 Boxplots of the reflectance of the different sensor bands and indice layers _____	38
Figure 23 Classification visualization of the mosaic (Datasets 1) _____	41
Figure 24 Classification results of the validation laboratory dataset (Datasets 2). _____	43
Figure 25 Results of the classification for this sample (long description) _____	44
Figure 26 Results of the classification for this sample (long description) _____	44
Figure 27 Results of the classification for this sample (long description) _____	45
Figure 28 Results of the classification for this sample (long description) _____	45

Figure 29 Results of the classification for this sample (long description)	46
Figure 30 Results of the classification for this sample (long description)	47
Figure 31 Results of the classification for this sample (long description)	47
Figure 32 Results of the classification for this sample (long description)	48
Figure 33 Results of the classification for this sample (long description)	48
Figure 34 Classification results of the WorldView-3 image.	50
Figure 35 Classification results of the Sentinel-2 image.	51
Figure 36 From left to right: original data set, data set after vegetation and dark pixel masking (1), Ferric Iron masking (2) and Iron Feature Band Ratio (IFBR) (3) applied.	52
Figure 37 Classified satellite images from WorldView-3 (left) and Sentinel-2 (right) satellites.	55
Figure 38 Visualization of the classification result of the WorldView-3 data	57
Figure 39 Location of the XRD measurements within the mine.	58
Figure 40 Classified satellite images from WorldView-3 (left) and Sentinel-2 (right).	59
Figure 41 Left: VNIR dataset from 2019, Right: SWIR dataset from 2020	63
Figure 42 Time series analysis of Sentinel-2 images (in a 2-year sequence).	66
Figure 43 Laboratory setup of the spectrometer with HySpex sensor technology.	74
Figure 44 Principle of diffractometry.	76
Figure 45 XRD results of sample AM5	77
Figure 46 XRD results of sample KM-w2	77
Figure 48 XRD results of sample AM1	78
Figure 47 XRD results of sample AM4	78
Figure 49 XRD results of sample L-s4	79
Figure 50 XRD results of sample L-s3	79
Figure 51 XRD results of sample Km-w2	80
Figure 52 XRD results of sample AM2	80
Figure 53 XRD results of sample L-w2	81
Figure 54 Digital Elevation Model (DEM) of the Skouriotissa mine. From: Charalambos, 2016a	82
Figure 55 Digital Elevation Model (DEM) of the Apliki mine. From: Charalambos, 2016b	82
Figure 56 Boxplots of the reflectance of the different sensor bands and indice layers.	83
Figure 57 NDVI of the Sentinel-2 images from the years 2015, 2017, 2019 and 2021	84

List of tables

Table 1 Description of the most important minerals related to Acid mine Drainage. _____	8
Table 2 Overview of various relevant and used indices in this work. _____	16
Table 3 Overview of Skouriotissa pits. _____	23
Table 4 Overview of Apliki pits. _____	24
Table 5 Overview of mineral samples used. _____	26
Table 6 Results of the XRD analysis [%]. _____	27
Table 7 Summary of WorldView-2 and WorldView-3 SWIR sensor characteristics. _____	28
Table 8 Further metadata of the WorldView-2 (VNIR) and WorldView-3 (SWIR) images. _____	29
Table 9 Overview of the Sentinel-2A bands and specifications. _____	30
Table 10 Summary of different selected thresholds for different Datasets for WorldView-3 and Sentinel-2 resolution. _____	36
Table 11 Listing of the most informative layers of the two Datasets. _____	38
Table 12 Accuracy Assessment of the RF-models from both Datasets. _____	42
Table 13 Overview of estimated area sizes of the different classes and sensors. _____	49
Table 14 XRD results of the five points investigated within the mine. _____	58
Table 15 List of Challenges and Implications regarding this work _____	60
Table 16 Overview of estimated area sizes of the different classes and sensors. _____	84
Table 17 List of metadata for the Sentinel-2 satellite images used in the time series analysis. _____	85

Abbreviations

Terms	Abbreviation	Description
Abbreviations	AMD	Acid Mine Drainage
	SIM, SIMs	Secondary iron mineral, Secondary iron minerals
	VMS	Volcanogenic Massive Sulphide
	VNIR	Visible and near infrared
	SWIR	Short wave infrared
	LWIR	Long wave infrared
	TIR	Thermal infrared
	HSI	Hyperspectral Imagery
	UAV	Unmanned Aerial Vehicle
Spectral analytical terms	RF	Random Forest
	SVM	Support Vector Machine
	MICA	Material identification and characterization algorithm (Kokaly, 2011)
	SAM	Spectral Angle Mapper
	HySpex	Hyperspectral camera brand by Norsk Elektro Optikk AS
	XRD	x-ray diffraction
	IFBR	Iron feature band ratio
Software and System	ENVI®	ENVI ® image analysis software
	R Studio	R 3.6.2, RStudio 1.2.5033
	QGIS	Quantum GIS, QGIS3, version 3.14.0
	Google Earth	Google Earth Pro (version 7.3.4.8573 (64-bit))
Research and federal institutes or governmental funded projects	USGS	United States Geological Survey
	GSD	Geological Survey Department, Ministry of Agriculture, Rural Development and Environment, Republic of Cyprus
	HCM	Hellenic Copper Mines
	CMC	Cyprus Mine Cooperation
	HyMap	Airborne hyperspectral imaging sensor (T. Cocks, R. Jenssen, A. Stewart, 1998)
	UP	University of Potsdam
	HU	Humboldt University of Berlin
	GFZ	Helmholtz Centre Potsdam German Research Centre for Geoscience
	IMA	International Mineralogical Association
	CNMNC	Commission on new Minerals Nomenclature and Classification

Acknowledgements

I would like to thank Prof. Dr. Dagmar Haase and Dr. Karl Segl for providing the structural foundation for writing this master thesis and for the great communication.

I would like to give special thanks to Nicole Koellner and Dr. Friederike Körting, who took over a huge part of the supervision.

I would like to thank Kolja, Annika, Georgianna, Momo and Lisa for their support in and outside of this work.

I would like to thank the University of Potsdam and the Geological Survey for providing data that contributed to this work.

Abstract

Global growth of industry and population leads to increasing demand of industrial and consumer goods. This necessitates an increase in mining activities and resource extraction. Resulting mine waste, and tailings serve as a repository for unused overburden and for the accumulation of processed waste-products. It is typical for so-called secondary iron minerals (SIMs) to be formed during the weathering of these materials under different pH-value conditions. Acid mine drainage (AMD) can result from rainwater infiltration and chemical processes within the deposited mass. Therefore, mine tailings must be spatially separated from their surroundings and monitored. The emergence of remote sensing methods provides new opportunities to survey large areas.

In this work a remote sensing approach was used to discriminate SIMs from surrounding material and minerals and subsequently classify different SIMs on the surface. This allows to reconstruct (/comprehend the former) the acidic environments that prevailed during the formation of these minerals and gives indication of the occurrence of AMD. Various SIMs have pH-values ranging from strongly acidic (<1.5, i.e., Schwertmannite and Copiapite) to neutral (>7, i.e., Hematite). Classifying these SIMs, leads to the identification of contaminated areas.

This method was developed based on a laboratory dataset with different minerals and vegetation samples. The datasets were originally acquired with hyperspectral HySpex cameras in the laboratory and were resampled to WorldView-3 (WV3) and Sentinel-2 (S2) band characteristics for analysis. A combination of different filter methods made pixel-based separation of SIMs possible. The results were subsequently classified using a RF-model to distinguish between different SIMs. In this training dataset, the RF model achieved an overall accuracy of 94.44% for the WV3 and S2 datasets (the area-adjusted overall accuracy was 93.45% and 93.62%, respectively). Subsequently, a second laboratory dataset with field samples was analysed using the same technique and the classification results were compared with XRD analyses of the samples.

Satellite images from WV3 and S2 sensors were then analysed using this methodology. The results for the study area of volcanogenic massive sulphide deposits in the Republic of Cyprus, namely Skouriotissa and Apliki, were then compared. The results for the Skouriotissa mine region showed a potential area of 17.22 to 45.58 ha of strongly acidic environment (by classification of Jarosite, pH~2.4) and 8.86 to 26 ha of moderately acidic environment/ contamination (by classification of Goethite/Limonite, pH~5) based on the WV3 satellite image. 27.32 to 87.04 ha and 6.12 to 38.24 ha for the S2 image, respectively.

Keywords: *Acid Mine Drainage, Tailings, Monitoring, Secondary Iron Minerals, Spectral, XRD, WorldView-3, Sentinel-2*

Zusammenfassung

Das Wachstum von Industrie und Bevölkerungszahl weltweit sowie technologische Fortschritte und Entwicklungen führen zu einer steigenden Nachfrage von Industrie- und Konsumgütern. Als Folge entstehen eine erhöhte Rohstoffnachfrage und ein Ausbau der Ressourcengewinnung sowie des Bergbaus. Abfallprodukte des Bergbaus und nicht genutztes Material (Abraum) werden meist in oder um den Abbaustandort aufgeschüttet. Diese sind natürlichen Degradationsprozessen ausgesetzt, bei denen saure Abwässer entstehen können. Dies geschieht durch die Verwitterung des Pyrit Minerals infolge der Infiltration von Regenwasser durch das Material. In unterschiedlichen pH-Wertumgebungen bilden sich unterschiedliche Minerale aus. Typisch sind die sogenannten sekundären Eisenminerale (SIMs – secondary iron minerals). Ein Auftreten dieser kann daher zu einer pH-Wert Abschätzung genutzt werden und mögliche saure Grubenwässer aufzeigen. Fernerkundungsmethoden bieten die Möglichkeit große Areale oberflächlich zu erfassen und abzubilden, was zu einer weitreichenden Überwachung genutzt werden kann.

In dieser Arbeit wurde eine Methode auf Grundlage von multispektralen Fernerkundungsdaten (Satellitenbilder von WorldView-3 und Sentinel-2) entwickelt, welche sekundäre Eisenminerale identifiziert und klassifiziert. Die Identifikation wurde durch den Einsatz von Masken erreicht. So fand eine Unterscheidung zwischen Pixeln statt, die und die keine typische spektrale Signale von SIMs aufweisen. Die Klassifikation wurde mit Hilfe eines RF-Modells durchgeführt. Dieses wurde anhand synthetischer Labordatensätze entwickelt und validiert. Im Trainingsdatensatz erreichte das RF-Modell eine Gesamtgenauigkeit von 94,44 % für die WorldView-3 und Sentinel-2 Datensätze. Es wurden drei Klassen mit verschiedenen pH-Wert-Identifikationen unterschieden: Hämatit ($\text{pH} > 7$), Goethit/ Limonit ($\text{pH} \sim 5$) und Jarosit ($\text{pH} \sim 2.4$).

Die Methodik wurde anschließend auf Satellitenbilder aus der Republik Zypern angewendet. Dabei standen die Minengebiete Skouriotissa und Apliki im Fokus, welche zu den vulkanogenen Massivsulfid-Lagerstätten (VMS-type) zählen. Die Ergebnisse für das Skouriotissa-Minengebiet ergaben auf der Grundlage des WV3-Satellitenbildes eine potenzielle Fläche von 17,22 bis 45,58 ha in stark saurem Milieu (Jarosit) und 8,86 bis 26 ha in mäßig saurem Milieu (Goethit/ Limonit) bzw. 27,32 bis 87,04 ha und 6,12 bis 38,24 ha für das Sentinel-2 Satellitenbild.

1 Introduction

1.1 Motivation

The Global demand for mining products is increasingly rising (Humphreys, 2020). This is due to a rapidly growing world population and technological developments in many areas around the world (Prior et al., 2012). Extraction of ores through mining poses a risk to humans and the environment due to various factors (Blahwar et al., 2012; Flores et al., 2021; Hadjipanagiotou et al., 2020; Jackisch et al., 2018a; Swayze et al., 2000; Yucel et al., 2014). On the one hand, there are the geomechanical risks, on the other the geochemical risks (Byrne et al., 2012). Significant impacts include vegetation clearance, soil sealing due to construction of new infrastructure, waste tailings, land subsidence, high water consumption, disturbance of natural habitats or cultural sites, emission of heat, radioactivity and noise, and release of solid, liquid or gaseous pollutants into other ecosystems (Lottermoser, 2010). The *Ernst & Young report of risks and opportunities for mining and metals in 2022* stated that environment and social issues are the number one risk for miners, including the environmental perspective as a serious business risk for the first time (Ernst & Young Global Limited, 2018).

An intensification of the operations of the mining industry, namely the extraction, mineral processing and metallurgical extraction will be observed with rising global demand. All three operations produce waste, which means that this issue will have to be dealt with even in larger scale in the future (Lottermoser, 2010).

Almost no waste is produced in the extraction of clay, sand or gravel. In contrast to this, a metal-bearing mineral resource where only a few percent of copper, lead or zinc concentrations or even parts per million in case of gold are extracted. Thus, only a very small fraction is extracted from the metal-bearing ores during processing and metallurgical extraction. Most of the extracted mass is gangue, which ends up as processing and smelter waste. Coal mining and processing therefore generate the largest quantities of waste, followed by the mining of non-ferrous ore, iron ores and industrial minerals (Lottermoser, 2010). Since no quantitative data is collected on how much waste is produced, this can only be broadly estimated. Lottermoser et al. estimated in 2010 that about 20,000-25,000 Mt of solid mine wastes are produced annually worldwide (Lottermoser, 2010). Nicholas LePan has published a descriptive visualisation of the Size of Mine Tailings in 2021 (Elements.visualcapitalist.com/, 2022), which is based on the Global Tailings Review of 2020 (Global Tailings Review, 2020). The annual tailings growth is estimated at 12.3 km³ and the total amount at 217 km³ of waste tailings. This amount would equal a cube with a side length and height of 6 km. The main contributors are copper (46%), gold (21%), iron (9%) and coal (8%) mining. Furthermore, it is highlighted that the amount of waste material is increasing, due to a declining of ore grades (Global Tailings Review, 2020).

Not all by-products of the mining industry are waste, a few can be reprocessed. Some waste rocks, sediments and soils can be used for the construction of roads and buildings for example. However, mine wastes that contain hazardous substances pose a huge risk potential. Depending on the type of mine and industry, these may include heavy metals, acids, metalloids, radioactivity and chemicals (Lottermoser, 2010). In addition to occurring during or shortly after extraction, hazardous substances can also arise over a longer period of time as a result of chemical processes in mine waste tailings (Hadjipanagiotou et al., 2020). The long-term release of pollutants depends mainly on the mineralogical composition and added reagents of the tailings (Lottermoser, 2010).

One effect that can be observed is the so-called Acid Mine Drainage (AMD). Sulphide-bearing minerals such as pyrite oxidise when exposed to atmospheric oxygen and rainwater. The dissolution leads to the formation of acids and the pH value in the material decreases. Various SIMs are formed, depending on the pH, redox potential, degree of oxidation, temperature and mineral content of the solution (Jackisch et al., 2018b). AMD not only poses a health risk to miners and technical equipment (Jackisch et al., 2018b), but also affects the stability of tailings piles (Byrne et al., 2012). An example of this is the disastrous failing of the mining dam consisting of iron ore tailings in Brumadinho, in Brazil in 2019. The dam breach caused more than $11 \times 10^6 \text{ m}^3$ of mining waste to be spread over 10 km downhill causing loss of life and environmental damage (Lumbroso et al., 2021; Silva Rotta et al., 2020). The economic consequences were devastating for both the operating company, Vale S.A., and the region. The company lost 9 billion US dollars in market capitalisation (Laier, 2019). In 2021, the government and Vale S.A. agreed to repair all environmental damage and an estimated payment of 7 billion US dollars for the communities in the region concerned (BBC news, 2021).

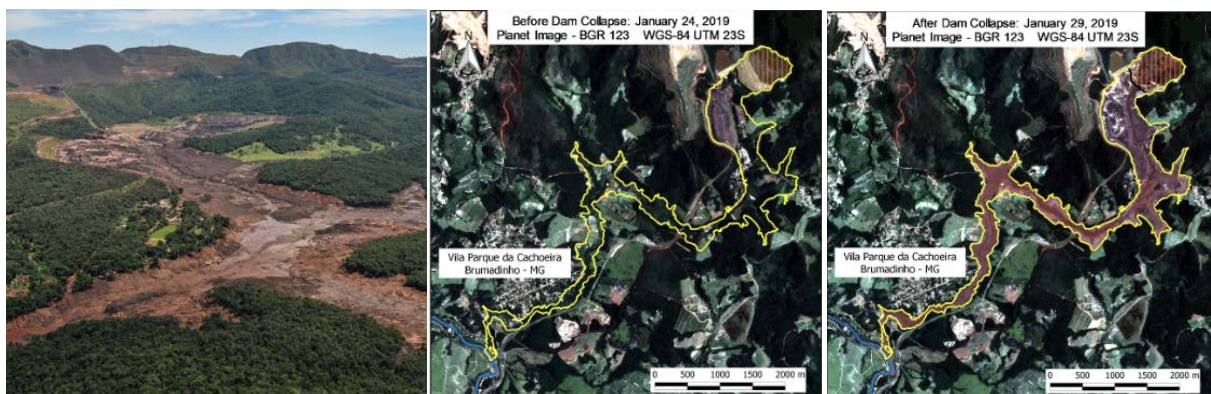


Figure 1 **Left:** This photo taken on 1 February 2019 shows the aftermath of the Brumadinho dam burst just downstream of the site (from Lumbroso et al., 2021) **Middle:** before and **Right:** after images of the dam collapse, indicating the dam location and the area directly affected by the mud wave (from Silva Rotta et al., 2020)

Furthermore, an accumulation of these acid substances into groundwater can occur (Byrne et al., 2012), putting entire human and environmental systems at risk. Therefore, monitoring and treatment of tailings is of great importance (Byrne et al., 2012; Lottermoser, 2010).

According to Lottermoser (2010), increased hydrogen concentrations and acid production in mining waste can be the result of:

- Oxidation of Fe-rich sulphides;
- Precipitation of Fe^{3+} and Al^{3+} hydroxides; and
- Dissolution of soluble Fe^{2+} , Mn^{2+} , Fe^{3+} and Al^{3+} sulphate salts.

The degree of hazard and the level of contamination of tailings were initially determined by sequential extraction techniques using chemical analysis (Byrne et al., 2012). This technique was able to identify contaminated sediment areas. However, the accuracy and reliability of these techniques can be questioned. The emerging of new technical capabilities led to the use of X-ray assisted spectroscopy (XAS), which provided direct detection of surface conditions at the molecular level. This method provided more accurate results in terms of metallic toxicity, mobility and bioavailability in the tailings than geochemical studies (Byrne et al., 2012). Remote sensing techniques already play different roles in mining activities. Satellite and aerial photographs are evaluated, mapped, and at a smaller scale, laboratory-based drill core and sample scans are classified, all to enhance existing deposit models and for exploration purposes for further mine development (short review of techniques in Koerting, 2021b).

Traditionally, multispectral and hyperspectral imaging has been carried out using field spectrometers, airborne systems or satellites (Aasen et al., 2014). With the advent of UAVs, and the construction of smaller and lighter sensor technologies, methods are developed to simplify and improve areal data collection. The advantages over satellite imagery are the higher spatial resolution, to collect data below the cloud cover and the temporal flexibility of the deployment (Aasen et al., 2014).

Monitoring tailings regarding AMD is an increasingly evolving field. Different approaches have emerged such as AMD detection and mapping with multi- and hyperspectral imagery in addition to classical methods such as satellite imagery, airborne surveys and conventional on-ground explorations with handheld spectrometers (Jackisch et al., 2018b). Many of these methods are scientific case studies and concepts. They refer to individual test areas due to their methodology or focus. A close look at the methods and developing a more universally applicable method, which can be incorporated into the everyday life of mining companies, is therefore desirable.

1.2 State of the Art

1.2.1 Geology of mine tailings: Acid producing reactions

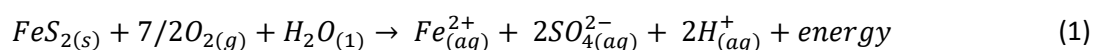
Potentially hazardous substances may increase in mine tailings over time due to various processes. As long as sulphides are in a reducing environment, they remain stable. Exposure to oxidising conditions destabilises them and the sulphides decompose in various oxidation processes. These sulphides are e.g., pyrite (FeS_2), galena (PbS), sphalerite (ZnS) and chalcopyrite (CuFeS_2). The scientific focus has been on the oxidation of pyrite as it is the most abundant sulphide mineral and appears in all types of geological environments. Pyrite can often be found in coal and metal ore deposits (Lottermoser, 2010; Nordstrom, 2015).

Depending on its mineralogical properties, the rate at which pyrite weathers is influenced by external chemical, physical and biological factors. Mineralogical properties include particle size, porosity, surface area, crystallography and trace element content of the mineral. The presence of other sulphides, the presence or absence of microorganisms, and the oxygen and carbon dioxide concentration, temperature, pH and $\text{Fe}^{2+}/\text{Fe}^{3+}$ ratio of the weathering solution are considered external factors. Oxidation reactions occur on the surfaces of the individual pyrite particles. The reactivity of pyrite is increased due to small particle sizes and large surface areas. Maximum oxidation occurs along pits, cracks, pores, and solid and liquid inclusions. Mining, crushing and grinding of pyrite-bearing rock for metal extraction to fine particle size significantly increases the surface area of pyrite and potentially exposes more pyrite to oxidation and weathering (Lottermoser, 2010).

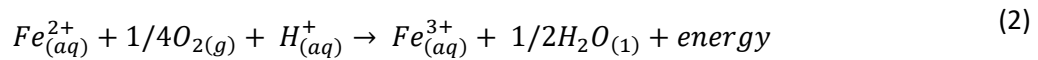
Lottermoser (2010) summarised these oxidation processes in four groups:

1. direct abiotic oxidation by oxygen
2. direct biotic oxidation by oxygen under the influence of microorganisms
3. indirect abiotic oxidation by oxygen and iron
4. indirect biotic oxidation by oxygen, iron and microorganisms

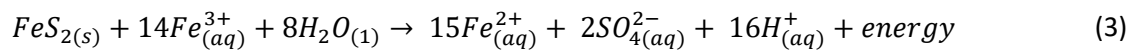
In the case of direct oxidation (both biotic and abiotic), pyrite oxidises with oxygen to form sulphurous acid:



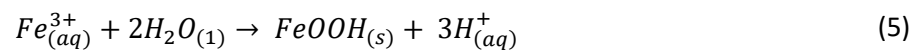
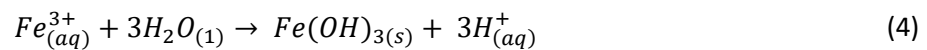
It is commonly assumed that pyrite oxidation occurs mainly by indirect oxidation. This oxidation is exothermic and release energy. It passes through three reaction stages. The first step is similar to the reaction of direct oxidation (formula 1). The second step (formula 2) represents the oxidation of iron(II) (Fe^{2+}) to iron(III) (Fe^{3+}) by oxygen and takes place at a low pH-values.



Within the third reaction (formula 3), pyrite is oxidised with the help of the Fe^{3+} previously formed in formula 2. This reaction results in the generation of Fe^{2+} . It is then again available for the reaction from formula 2. The reactions (formula 2 and 3) thus form a continuous cycle of the transformation of Fe^{2+} into Fe^{3+} and the subsequent oxidation of pyrite by Fe^{3+} to produce Fe^{2+} . This process continues until the supply of pyrite or Fe^{3+} to the reaction system is exhausted (Lottermoser, 2010).



The pH of the weathering material determines the abundance of the oxidant Fe^{3+} . In neutral and alkaline waters, the solubility of Fe^{3+} is very low and therefore the concentration is low. Thus, pyrite oxidation by Fe^{3+} in neutral to alkaline waters is slow and rather marginal. Furthermore, the concentration of dissolved Fe^{3+} decreases with increasing pH-value. Fe^{3+} dissolution is limited by the precipitation of iron hydroxides ($Fe(OH)_3$, respectively ferrihydrite) and oxyhydroxides ($FeOOH$, respectively goethite or lepidocrocite). If the pH value rises above 3, the following reaction occurs (formula 4 and 5). This can happen, for example, due to carbonate minerals in the material (Lottermoser, 2010).



The dissolved Fe^{3+} leads to a high acidity of the material due to the release of hydrogen ions into water. The lowered pH allows more Fe^{3+} to remain in the solution. In turn, this is then involved in the oxidation of pyrite (formula 3), which leads to a further lowering of the pH-value. The chemical reactions of pyrite are also called the AMD motor (Figure 2). Pyrite, Fe^{3+} and oxygen are the fuel, oxygen also is the starter and Fe^{3+} -hydroxides, sulphuric acid and heat of the sulphidic waste come out of the exhaust pipe (Lottermoser, 2010).

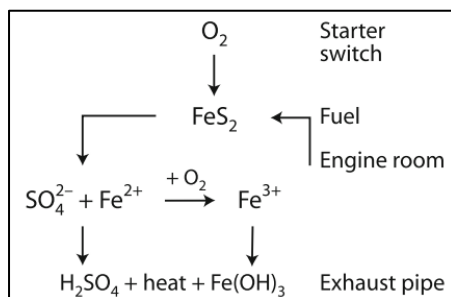


Figure 2 Schematic of the so-called "AMD engine" (self-sustaining, cyclic destruction of pyrite) from Lottermoser, 2010. The oxidation of pyrite is triggered by oxygen ("starter switch"). Pyrite, oxygen and iron ("fuel") burn in the waste ("engine room") and release Fe^{3+} hydroxides, sulphuric acid and heat into the mine water ("exhaust").

1.2.2 Geology of mine tailings: Formation of secondary iron minerals (SIMs)

Fe^{2+} and Fe^{3+} are each surrounded by water molecules. Dissociation of a proton of these water molecules results in a reduction of the charge of the dissolved species. This process is called *hydrolysis* (formula 4 and 5). In further steps, Fe-OH and Fe-O linkages may occur and crystalline iron oxides may form (Blume et al., 2010). Figure 3 displays the pH-value ranges at which some of the minerals are forming. Figure 4 shows the transformations between different SIMs and associated minerals which are discussed in the following.

Ferrihydrite can transform in two parallel reactions to Hematite and to Goethite, which has been the result of synthesis experiments under ground-level conditions. Both reactions take place in a solution, which makes water necessary for this process (Blume et al., 2010). Compared to Goethite, Hematite is formed at lower water contents and higher temperatures. For this reason, large quantities of Hematite are found mainly in tropical and subtropical latitudes. The formation of Goethite is located in the neutral pH range (6-8). Lepidocrocite can be formed by a slow oxidation of Fe^{2+} at a low concentration of carbonates. Lepidocrocite is very stable and takes a long time to transform into Goethite. Through thermal transformation, Goethite and Lepidocrocite can form Hematite (Figure 4) (Blume et al., 2010). Many rocks contain small amounts of lithogenic Magnetite (Fe_3O_4). It is also very resistant to weathering. Though, it can thermally transform into Hematite via Maghemite (Blume et al., 2010).

In pyrite, not only Fe^{2+} but also the sulphide ions are oxidised. This leads to the formation of Goethite ($FeOOH$) and sulphuric acid (H_2SO_4). If pH conditions are lower than 3, the Fe^{2+} can only be oxidised bacterially, e.g. by *Thiobacillus ferrooxidans* (Nordstrom, 2015). Moreover, at these pH values, the Fe^{3+} ions do not hydrolyse completely and no Fe(III) oxides are formed, but Fe(III) hydroxysulphates, such as Schwertmannite and Jarosite. Jarosite is stable in lower pH conditions (Nordstrom, 2015) and therefore a good indicator for acid environments and AMD. When the pH changes back to more alkaline values, Schwertmannite can hydrolyse back into Goethite (Blume et al., 2010).

The distribution of SIMs allows conclusions to be drawn about the conditions that must have existed during their formation. For example, the relative pH value can be estimated, which plays a decisive

1 Introduction

1.2 State of the Art

role in the formation of various secondary minerals. Large-scale occurrence of SIMs therefore also indicates an increased risk of AMD and, as a consequence, possible destabilisation of mine tailings. As already mentioned, the pH conditions differ significantly between different SIMs. Therefore, not only the detection of SIMs but also a differentiation would be preferable.

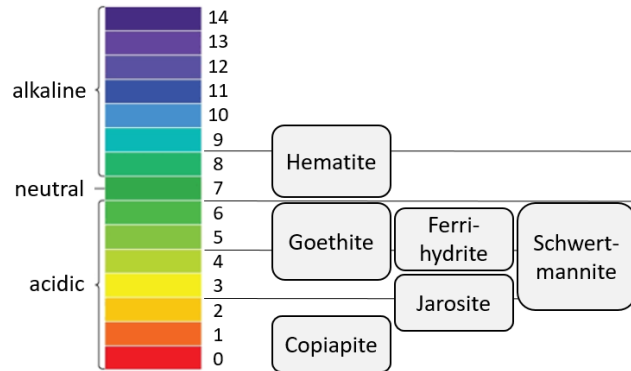


Figure 3 Overview of selected minerals and their pH-range occurrence.

Secondary minerals are divided into sulphates, oxides, hydroxides and arsenates, carbonates, silicates and native elements (Lottermoser, 2010). Examples are listed in

Table 1. For the investigation of this work, the initial focus was on five SIMs: Hematite, Limonite, Goethite, Jarosite and Copiapite, going from a neutral to high acidic pH environment as indicators for changes in pH-value.

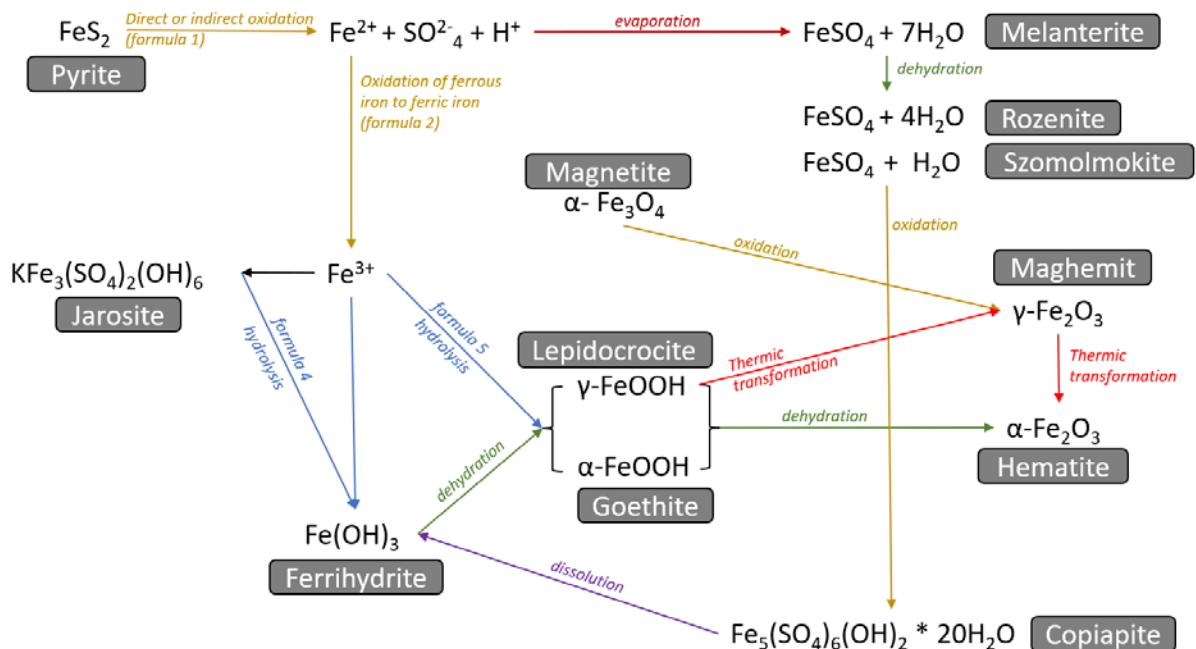


Figure 4 Overview of the overall sequence of mineral reactions in pyrite oxidation. Modified after Blume et al., 2010; Jordanova, 2017 and Nordstrom, 2015

1 Introduction

1.2 State of the Art

Table 1 Description of the most important minerals related to AMD, their common formulas, as far as known the pH ranges to be expected, and characteristic spectral absorption ranges. Adapted from Hermann et al. 2018 (based on publications by Hunt & Ashley (1979), Crowley et al. (2003) and Bishop & Murad (2005)).

Mineral	Formula	pH	Characteristic absorption features (nm)	Type ⁶
Alunite	$\text{KAl}_3(\text{SO}_4)_2(\text{OH})_6$	*	430, 910, 1850, 2270, 2630, 4900, 8000 – 10000, 15000 – 24000	Al hydroxysulphate
Copiapite	$\text{Fe}_5(\text{SO}_4)_6(\text{OH})_2 \cdot 20\text{H}_2\text{O}$	< 1.5	431, 541, 868, 1178, 1453, 1768, 1941 ¹	Mixed divalent-trivalent hydrous metal sulphates
Ferricopiapite	$\text{Fe}_{2/3}^{3+}\text{Fe}_4^{3+}(\text{SO}_4)_6(\text{OH})_2 \cdot 20\text{H}_2\text{O}$	*	432, 550, 871, 1425, 1768, 1942 ¹	Mixed divalent-trivalent hydrous metal sulphates
Ferrihydrite	$5\text{Fe}^{3+}\text{O}_3 \cdot 9\text{H}_2\text{O}$	> 4.5	910 – 930 ³ 1450, 1940 ¹	Hydroxide
Fibroferrite	$\text{Fe}^{3+}(\text{SO}_4)(\text{OH}) \cdot 5\text{H}_2\text{O}$	*	428, 543, 827, 1175, 1490, 1930 ¹	Sulphate
Goethite	$\alpha\text{-FeOOH}$	4.5 - 6.1	480, 674, 939, 1450, 1940 ¹ 910 – 940 ³ +-1000, 940, 650 ⁴	Hydroxide
Halotrichite	$\text{Fe}^{2+}\text{Al}_2(\text{SO}_4)_4 \cdot 22\text{H}_2\text{O}$	*	(436), 994, 1180, 1445, 1945 ¹	Mixed divalent-trivalent hydrous metal sulphates
Hematite	$\alpha\text{-Fe}_2\text{O}_3$	> 7	674 ² 872 ¹ 850 – 885 ³ 850 ⁴	Hydroxide
Jarosite	$\text{KFe}_3(\text{SO}_4)_2(\text{OH})_6$	2.3-2.6	437, 911, 1467, 1850, 1936, 2264 ¹ 435, 650, 900 -925 ³ 430 ⁴	Fe hydroxysulphate
Lepidocrocite	$\gamma\text{-FeOOH}$	*	*	Hydroxide

1 Introduction

1.2 State of the Art

Mineral	Formula	pH	Characteristic absorption features (nm)	Type ⁶
Melanterite	$\text{Fe}^{2+} \cdot \text{SO}_4 \cdot 7 \text{H}_2\text{O}$	*	432, 892, 1150, 1475, 1972 ¹	Simple hydrous metal sulfates with divalent metal cations
Paracoquimbite	$\text{Fe}_2^{3+}(\text{SO}_4) \cdot 9\text{H}_2\text{O}$	*	429, 558, 785, 1157, 1412, 1480, 1910, 1976 ¹	Fe^{3+} sulphates
Pickeringite	$\text{Mg}^{2+}\text{Al}_2(\text{SO}_4)_4 \cdot 22\text{H}_2\text{O}$	*	1440, 1940 ¹	Mixed divalent-trivalent hydrous metal sulphates
Rhomboklase	$(\text{H}_5\text{O}_2)^{1+}\text{Fe}^{3+}(\text{SO}_4) \cdot 2\text{H}_2\text{O}$	*	428, 513, 793, 2002 ¹	Fe^{3+} sulfates
Rozenite	$\text{Fe}^{2+}\text{SO}_4 \cdot 4\text{H}_2\text{O}$	*	432, 978, 1170, 1448, 1954, 1980 ¹	Fe^{2+} sulfates
Schwertmannite	$\text{Fe}_8\text{O}_8(\text{SO}_4)(\text{OH})_6$	2.8 – 6.5	911, 1450, 1950 ¹	Fe hydroxysulfate
Szomolnokite	$\text{Fe}^{2+} \cdot \text{SO}_4 \cdot \text{H}_2\text{O}$	*	430, 940, 1328, 1520, 1990, 2098, 2403 ¹	Simple hydrous metal sulfates with divalent metal cations
Sources: ¹ Crowley et al., 2003, ² Jackisch et al., 2018a, ³ Bishop and Murad, 2005, ⁴ Hunt and Ashley, 1979, ⁵ Herrmann et al., 2018, ⁶ Lottermoser, 2010 *No references found in literature				

1.2.2 Spectroscopy

Spectroscopy is generally understood to be the study of light as a function of wavelength (Clark, 1999a). In spectroscopy, the electromagnetic spectrum is generally divided into defined wavelength ranges: Ultraviolet (UV): 0.001 - 0.4 μm , Visible: 0.4 - 0.7 μm , Near Infrared (NIR): 0.7 - 1.4 μm , Shortwave Infrared (SWIR): 1.4 - 3.0 μm , Mid Infrared (MIR): 3.0 - 30 μm and Far Infrared (FIR): 30 μm - 1 mm. Remote sensing covers methods and techniques for imaging surface information of a wide variety of objects and surfaces from a long or immediate distance (Van der Meer and De Jong, 2001). A measurement refers to the recording of the physical conditions of electromagnetic radiation present as emission, reflection, absorption or transmission from surfaces (Clark, 1999a). Knowledge of characteristic absorption wavelengths allows conclusions to be drawn about specific chemical elements or compounds in the medium under investigation.

Remote sensing sensors are able to measure wavelength ranges that cannot be detected by the human eye. Usually these are passive sensors that detect reflected sunlight from surfaces. A multispectral image consists of several, defined channels, where each channel covers a wider range of the wavelength region. Hyperspectral data works similarly, except that a large number of consecutive channels are recorded, with each channel containing information of a very narrow wavelength range (Figure 5). This fine spectral resolution allows to retrieve material-specific information (Köllner and Volkmer, 2021). Multispectral sensors record the incoming reflected or emitted radiation using individual setups, that differ e.g., in the number of bands, bandwidth and spatial resolution. This also applies to the sensors used in this work with WorldView-3 and Sentinel-2 (Figure 5).

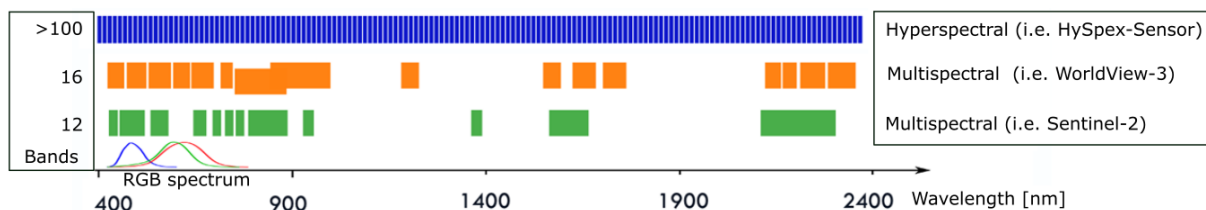


Figure 5 Schematic representation of the band positions and width of the multispectral Sentinel-2A and WorldView-3 data in comparison to the hyperspectral HySpex system (modified from Koerting, 2021b).

In an imaging spectrum, the absorption, transmission, reflection or emission intensity of a surface can be represented in relation to the wavelength or frequency and energy level (Hunt, 1989). Depending on the material, different absorption bands, so-called absorption features, can be found in a spectrum plot. Their formation is explained in the next section. Depending on the number of bands of the sensor/satellite, the graph of the spectrum is more or less continuous. Figure 6 shows a spectrum of a jarosite mineral displayed in the three sensor resolutions. It becomes visible how the amount of information decreases when the number of bands is reduced. Moreover, at a certain reduction, it is

no longer possible to show all absorption features. This requires measurements at at least three points, the left and right shoulder and the absorption maximum of the feature.

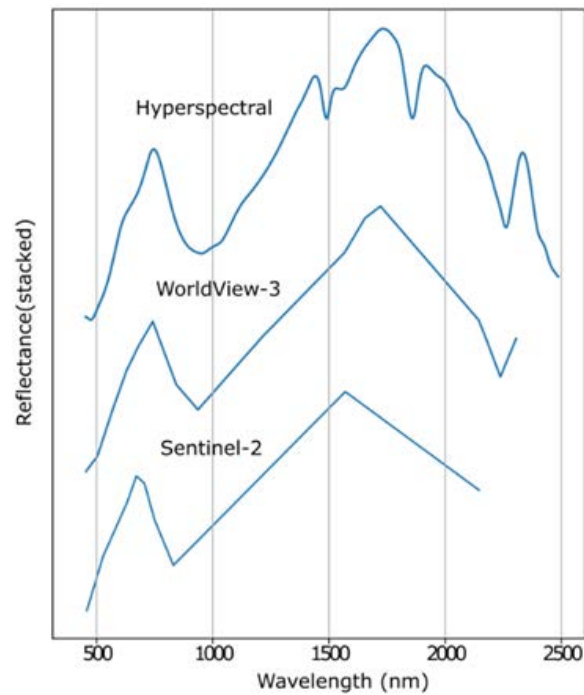


Figure 6 Jarosite spectra from a laboratory sample displayed in three different spectral resolutions. Sample was measured with the HySpex sensor and spectrally resampled to WorldView-3 and Sentinel-2 resolution.

1.2.3 Spectral response of surfaces and spectral features

When photons of electromagnetic radiation interact with matter, the energy levels of individual atoms are changed (Gupta, 2003). In solid materials, radiation is absorbed or emitted as a result of changes in the total energy content of the material. An absorption of photons leads to a transition to a higher energy level, an emission of photons to a transition to a lower energy level. Through an interaction of absorption and emission, and a change between different energy levels, so-called features, are generated in specific wavelengths (Hunt, 1989; Pieters and Englert, 1994). For electronic energy levels, the detection in the form of spectral features is typically in the visible and near infrared, for vibrational energy levels in the infrared range (Hunt, 1989). There are mainly four different electronic processes that lead to spectral features in natural minerals (Hunt, 1989), described in the following:

- The *crystal field effect* is an electron transition in mineral spectra that results from incompletely occupied orbitals in transition elements such as scandium (Sc), titanium (Ti), vanadium (Va), chromium (Cr), manganese (Mn), iron (Fe), cobalt (Co), nickel (Ni), copper (Cu) or zinc (Zn) (Borsdorf, 1996; Clark, 1999b). The energy levels of atoms in the crystal field are split and a transition to a higher energy level occurs through the absorption of a photon from incoming energy (Pieters and Englert, 1994).
- *Charge transfer* takes place between neighbouring ions when the transition of an electron in the crystal system takes place through the absorption of a photon (Pieters and Englert, 1994). Such a transition can occur between the same metals with different valence states, e.g., Fe^{2+} and Fe^{3+} . Compared to the crystal field transition, charge exchange produces bands that are much more prominent (Clark, 1999b).
- Electrons that are tightly bound to an atom are called valence bands, while electrons that are moving freely are called conduction bands. The transition between the two is defined as a *conduction band transition* (Pieters and Englert, 1994). As a result of these processes, bands are formed in the visible wavelength range (Van der Meer and De Jong, 2001). Absorption features caused by transition of electrons are typically found in the shorter wavelengths, in the VNIR.
- When a naturally occurring grid system has defects, absorption can occur. Discrete energy levels are generated and electrons can be bound. These so-called *colour centres* are responsible for e.g., the different colours of fluorites (Clark, 1999b).

Another cause of the production of absorption features are *vibrational oscillations* at the molecular level, in which the bending and stretching of molecular bonds is triggered by incident electromagnetic radiation (Gupta, 2003; Van der Meer and De Jong, 2001). The binding energy and mass of the individual atoms determine the frequency of the oscillation (Clark, 1999b). Several types of vibration can be distinguished. The fundamental tones are defined as straight-line motion caused by the vibration of individual isolated molecules (Pieters and Englert, 1994). An overtone of several fundamental tones can occur. Combination tones occur when several different fundamental vibrations are added together (Clark, 1999b; Van der Meer and De Jong, 2001). These vibrational oscillations typically cause absorption features in the SWIR wavelength range and at longer wavelengths e.g., LWIR. Figure 7 shows example Minerals showing different of these absorption features occurring in different wavelength ranges.

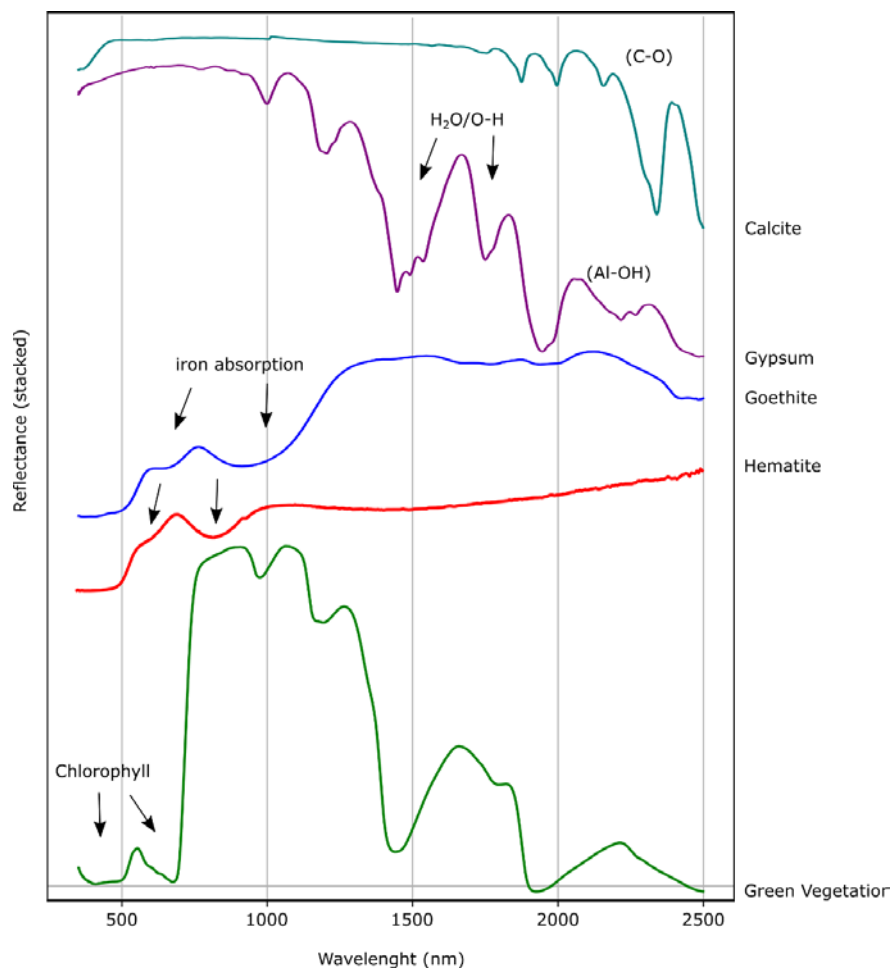


Figure 7 Material specific reflectance spectra for selected minerals and vegetation with identification of their absorption characteristics, shown in the wavelength range 400-2500 nm; Illustration from (Köllner and Volkmer, 2021) with spectra from the USGS Spectral Library Version 7 (Kokaly et al., 2017).

1.2.4 Spectral identification of Minerals

Imaging spectrometers have been in use since the 1980s and are typically applied to map minerals for exploration purposes (Swayze et al., 2000). Swayze et al. were the first to use imaging spectrometers in a mining district to collect data aimed at remediating mining waste (Swayze et al., 1996, 2000).

Existing studies used very different data bases and methods. Spaceborne data were used in Kopačková et al., 2012; Pour and Hashim, 2012; Safari et al., 2018 and van der Werff and van der Meer, 2015, whereas airborne data were used by Kopačková, 2014; Kopačková and Koucká, 2017; Kruse et al., 2011; Mielke et al., 2014; Notesco et al., 2014 and van der Meer et al., 2018. Flores et al., 2021 and Jackisch et al., 2018a worked with UAV data. Ground based imaging of mine faces on the other hand were investigated in Krupnik and Khan, 2019; Lorenz et al., 2018; Murphy et al., 2015. In many of the studies mentioned, laboratory-based measurements of samples were also used, mostly for validation. Dalm et al., 2017 can be mentioned as an example of intensive use of these data. Other data collections also included classical on-site surveys with handheld devices such as handheld field spectrometers (Dalm et al., 2014; Kopačková et al., 2012), laser induced breakdown spectroscopy (LIBS) or X-ray fluorescence (XRF) (Dalm et al., 2017).

Monitoring, i.e., the detection and mapping of AMD using remote sensing methods, is gaining popularity. This is done by differentiating SIMs as proxies for pH-value, which are identified by means of multi- and hyperspectral image data.

1.2.5 Spectral Properties of iron minerals

Individual mineral spectra differ in their absorption characteristics. The spectrum of a rock is a combination of spectra of the minerals it contains (Hunt, 1989). If several ferrous minerals are compared, a common feature in the VNIR range around 900 nm is important. The absorption band minimum shifts within ± 50 nm depending on the mineral, and therefore it can be used for discrimination. For example, the absorption maximum of hematite is at a wavelength of about 850 nm and that of goethite at about 930 nm (Figure 8). However, a high spectral bandwidth resolution of at least 10 nm is needed to measure these fine shifts (Cudahy, 2016). This can most likely be achieved by using hyperspectral sensors (Jensen, 2010). But there is the problem that there is a water band in this area. This is further explained in the chapter 4.4 Challenges and Implications (page 60).

In general, it seems that iron is spectrally dominant and small quantitative fractions are sufficient for this (Kirsch et al., 2018). It can therefore happen that iron features are spectrally visible, but investigations e.g., by XRD (X-ray diffraction) do not yield any results. It should also be noted that iron features occur when iron is generally present in the material, regardless of whether it is a SIM or

another iron-bearing mineral (e.g., Magnetite). Iron absorptions therefore indicate the general occurrence of iron as an elemental proxy in the crystal structure and are therefore very important for the crystal field (Kurz, 2011).

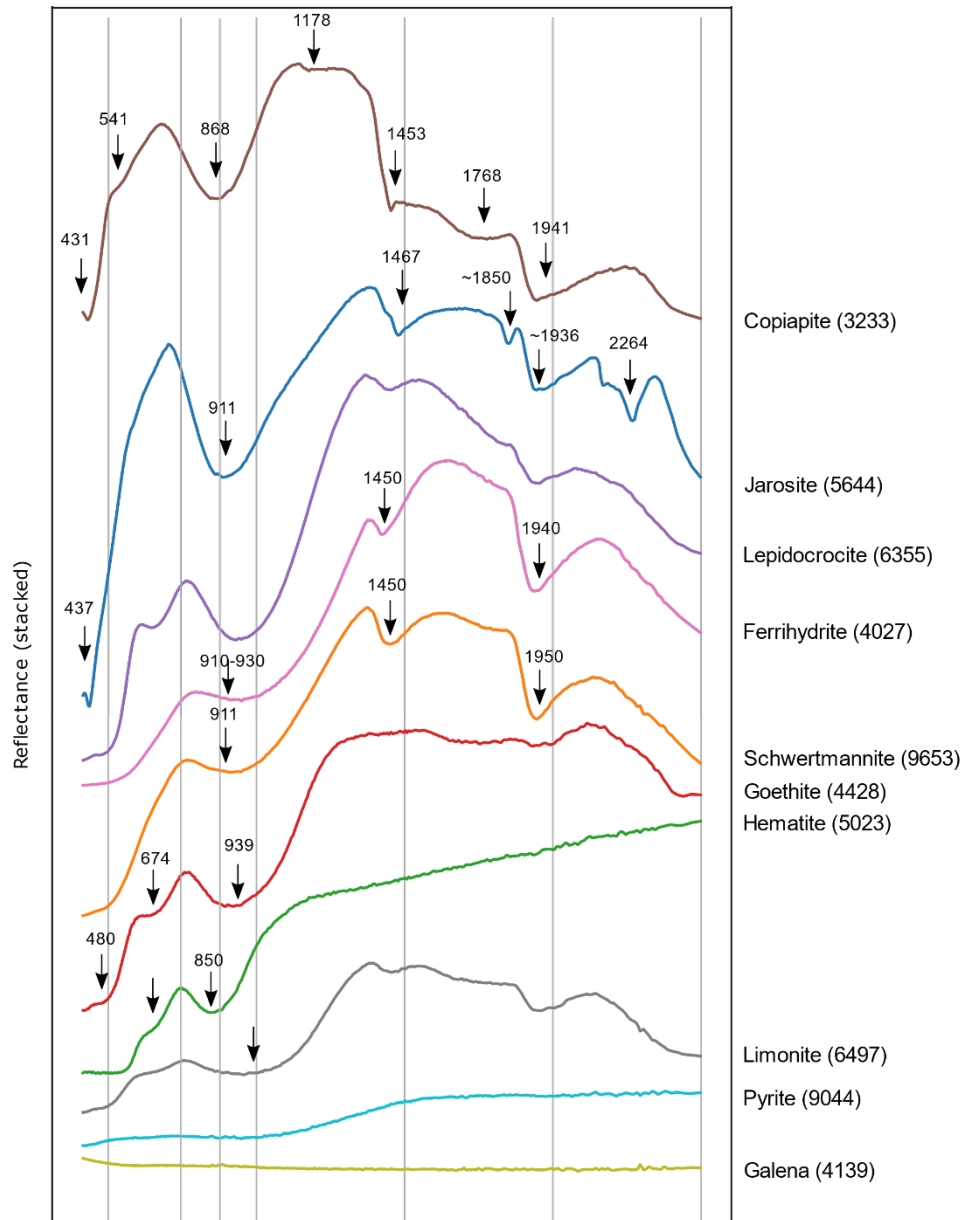


Figure 8 Hyperspectral representation of the reflectance of various SIMs. Based on USGS database, abbreviation of internal USGS IDs in brackets (Kokaly et al., 2017). Typical and known absorption features and their wavelengths are marked, based on (Bishop and Murad, 2005; Crowley et al., 2003; Hunt, 1989; Hunt and Ashley, 1979; Jackisch et al., 2018b).

1.2.6 Remote sensing indices

In the field of remote sensing, it is possible to create so-called indices by combining different bands from different wavelength ranges. Vegetation indices such as the NDVI are probably the most well-known, but indices exist for many more application areas. The website of the Index Data Base, which lists various indices for different sensors, currently provides a list of 519 different indices (Indexdatabase.de/, 2022). Also in this work, the use of indices was applied, described in the following.

The Normalised Difference Vegetation Index (NDVI) makes use of the characteristic property of the chlorophyll of plants to predominately absorb electromagnetic radiation in a wavelength range from approximately 600 - 700 nm (red) and to reflect from 700 - 1300 (NIR) nm. A typical reflectance spectrum of a plant shows a clear increase in intensity between these two ranges (see Figure 7). Consequently, the NDVI is defined as the difference of these intensities divided by their sum (Table 2). Using this formula per pixel the NDVI values are between -1 and 1. A dense vegetation has at least a value of > 0.3 (Herrmann et al., 2018). Since the underlying spectral properties can be traced back to chlorophyll, the NDVI can also provide information on the vitality or stress of the plant (Rouse et al., 1973).

Furthermore, the Iron Feature Band Ratio (IFBR) is used as a type of index for this work. The absorption minimum of iron-containing minerals at approximately 900 nm is generally broad and causes a drop in reflectance beginning at approximately 730 nm. The negative increase observed from this range onwards can be used to obtain an indication of the presence of iron minerals. To achieve a normalisation similar to NDVI, the same formula is used but with modified bands (Table 2).

Table 2 Overview of various relevant and used indices in this work. Specification of the wavelengths used for the calculation and which bands they represent for the sensors of WorldView-3 and Sentinel-2. Based on (Rowan and Mars, 2003), Index Data Base (IDB). (Dogan, 2008) and (Herrmann et al., 2018)

#	Indices	Wavelengths [nm]	Sentinel-2 bands	WorldView-3 bands
1	Ferrous iron (Ferric iron, Fe ²⁺)	$\frac{(2145:2185)}{(760:860)} + \frac{(520:600)}{(630:690)}$	$\frac{(Band\ 12)}{(Band\ 8)} + \frac{(Band\ 3)}{(Band\ 4)}$	$\frac{(Band\ 13)}{(Band\ 7)} + \frac{(Band\ 3)}{(Band\ 5)}$
2	Ferric iron, Fe ³⁺	$\frac{(630:690)}{(520:600)}$	$\frac{(Band\ 4)}{(Band\ 3)}$	$\frac{(Band\ 5)}{(Band\ 3)}$
3	Ferric Oxides	$\frac{(1600:1700)}{(760:860)}$	$\frac{(Band\ 11)}{(Band\ 8A)}$	$\frac{(Band\ 11)}{(Band\ 7)}$
4	Ferrous Silicates	$\frac{(2145:2185)}{(1600:1700)}$	$\frac{(Band\ 12)}{(Band\ 11)}$	$\frac{(Band\ 13)}{(Band\ 11)}$
5	Normalized Difference Vegetation Index (NDVI)	$\frac{(800 - 620:700)}{(800 + 620:700)}$	$\frac{(Band\ 8 - Band\ 4)}{(Band\ 8 + Band\ 4)}$	$\frac{(Band\ 7 - Band\ 5)}{(Band\ 7 + Band\ 5)}$
6	Iron Feature Band Ratio (IFBR)	$\frac{(\sim 730 - \sim 950)}{(\sim 730 + \sim 950)}$	$\frac{(Band\ 5 - Band\ 7)}{(Band\ 5 + Band\ 7)}$	$\frac{(Band\ 6 - Band\ 8)}{(Band\ 6 + Band\ 8)}$

1.2.7 Research groups and predominant methodology

Various working groups are engaged in the research around geological-related spectroscopy. Some of them have a focus on iron mineralogy and/or acid drainage. In the following, a number of them are presented. Due to the variety in research, only a small number of representative research in the field will be discussed and the entire spectrum of research cannot be given the room it deserves.

1. As one of the first representatives of geological hyperspectral mapping, the **United States Geological Survey (USGS)** the group around and including Swayze, Kokaly and Clark must be mentioned. They were among the first to venture into geological hyperspectral mapping. The USGS also developed MICA, the Material Identification and Classification Algorithm (Kokaly, 2011), and the Tetracorder (Clark et al., 2003). These tools enabled the mapping of minerals and surfaces of VNIR-SWIR data in the laboratory and airborne, as well as SWIR ground-based data (Swayze et al., 1996, 2000).

Swayze et al. published a study in 2000 that mapped pH-acidic areas of mine tailings in Leadville, Colorado using hyperspectral aircraft data. SIMs were selected and classified using the Tetracorder algorithm. The spectra were measured based on field samples and validated with XRD analyses. It was possible to detect changes in the mineral assemblage, especially on the slopes of tailings. Zones with Jarosite and Goethite could be differentiated, Jarosite served as an acidic identifier (Swayze et al., 2000).

2. As part of the remote sensing department of the Czech surveying authority, **Veronika Kopačková** studies soil parameters using airborne or spaceborne multi- and hyperspectral data. Her work includes several studies on mineral mapping and pH-value investigations. In 2014, she was able to estimate pH ranges by mineral mapping using HyMap data in the area of the opencast mining lakes of the Sokolov region (Czech Republic). Pyrite, Jarosite and Lignite were taken as indicators for a pH value of 3 and less, Jarosite together with Goethite corresponds to a pH-value range of 3 - 6.5 and Goethite alone corresponds to a pH-value range of more than 6.5. Jarosite and Goethite were then distinguished by a spectral shift in the range between 900 and 1000 nm. A shift to shorter wavelengths corresponded to Jarosite and a shift to longer wavelengths corresponded to Goethite. In addition, small and narrow absorption features were used to distinguish the other minerals (Kopačková, 2014).

3. In 2018, the working group around **Robert Jackisch** and **Richard Gloaguen** from the Helmholtz-Zentrum Dresden-Rossendorf investigated an area in Sokolov with UAVs (Jackisch et al., 2018a). Using UAVs equipped with RGB and hyperspectral cameras, a detailed mapping with spatial resolutions in the range of a few centimetres was achieved. A three-dimensional digital surface model was created and an estimation of the pH-value ranges was carried out using the SIMs Jarosite and Goethite. Indices were used to estimate the iron content in the materials represented by the pixels. They attributed

certain limits to specific minerals. A validation was carried out by use of reference spectra recorded from samples. These ground truth data were also analysed in the laboratory for pH-values, with XRD and XRF. The classification was performed with the Spectral Angle Mapper (SAM), which uses a spectral angle error metric to compare two or more spectra (Dennison et al., 2004; Kruse et al., 1993). The result was a model representing a temporal and morphological change of the area (Jackisch et al., 2018a).

In a feasibility study of the working group led by **Erik Herrmann et al.**, two test areas near Hoyerswerder (City in Saxony, Germany) were investigated. Multispectral, hyperspectral and thermal cameras were used. The first area was examined for heavy metal contamination. Since heavy metal concentrations only occur as trace elements, proxies were used instead of direct detection. Studies showed that changes in the absorption behaviour of the hydroxyl groups of clay minerals can be detected in the SWIR range. However, the study was conducted with a sensor in the VNIR range, which is why the vegetation and plant stress was taken as a proxy. They conclude that vegetation shows reduced chlorophyll activity when heavy metal concentrations reach harmful levels, but that other factors such as summer drought or irrigation have a stronger influence on vegetation stress. In the second area, the iron contents of a lake and a re-habilitated lake were compared. For this purpose, an iron index was calculated from multi- and hyperspectral data. It uses the decline in reflectance between 730 and 900 nm and is as such comparable to the IFBR mentioned in this work. It was possible to point out clear differences between the water bodies, indicating a change in the pH balance of the water bodies (Herrmann et al., 2018).

The working group published a study on UAV-based hyperspectral environmental monitoring of AMD effects in 2021 by **Hernan Flores et al.** The study area is around the Rio Tinto mine and river outlet in Spain, where water drains from the western part of the Rio Tinto massive sulphide deposit releases large volumes of acidic water with high levels of dissolved metals (Fe, Al, Cu, Zn) into the Odiel River. Using UAV data, they were able to capture high-resolution images of the area with a spectral range of 504 to 900 nm. The area was divided into two classes using a Support Vector Machine (SVM) classification. The water pixels were then classified into a hydrogeochemical map using RF regression. The soil pixels were used to classify a mineral map using the SAM. Field samples were used as ground-truth and training data. They were able to generate maps that successfully estimated the concentration of dissolved metals in the water and classified associated iron species (e.g. Jarosite, Goethite) in the sediments (Flores et al., 2021).

1.2.8 Research Objectives

Based on the motivation described above and previous research, the following research objectives emerge:

- Develop a method to detect secondary iron minerals in multispectral satellite data.
- Carry out a classification to distinguish between different secondary iron minerals.
- Infer areas of low pH and associated hazard zones.

2 Methods

2.1 Study region

The sulphide deposits on Cyprus belong to the mafic type of volcanogenic massive sulphide deposits (VMS). The host lithology is basaltic. These sulphide deposits are located in the Pillow Lava Series of the Troodos ophiolite, which is a fragment of the Mesozoic ocean floor. It formed about 91 million years ago and was moved and placed in its present position by the collision of the Eurasian and African tectonic plates (Adamides, 2010a; Antivachis, 2015). The exhalative deposits occur at different stratigraphic levels, from the Upper Pillow Lavas to the Sheeted Dikes Complex (Adamides, 2010a). The Troodos ophiolite covers an area of about 3000 km on the island of Cyprus. This section of the oceanic crust includes all lithologies between the upper mantle and the Cretaceous marine sediments (Figure 9). In the lower sequence, ultramafic lithologies include harzburgites, dunites, chromitites. These were extensively serpentinised and overlain by gabbro and a sheeted dyke complex. On top are Upper Pillow lavas that have not been overlain by hydrothermal alteration (Fonseca et al., 2017).

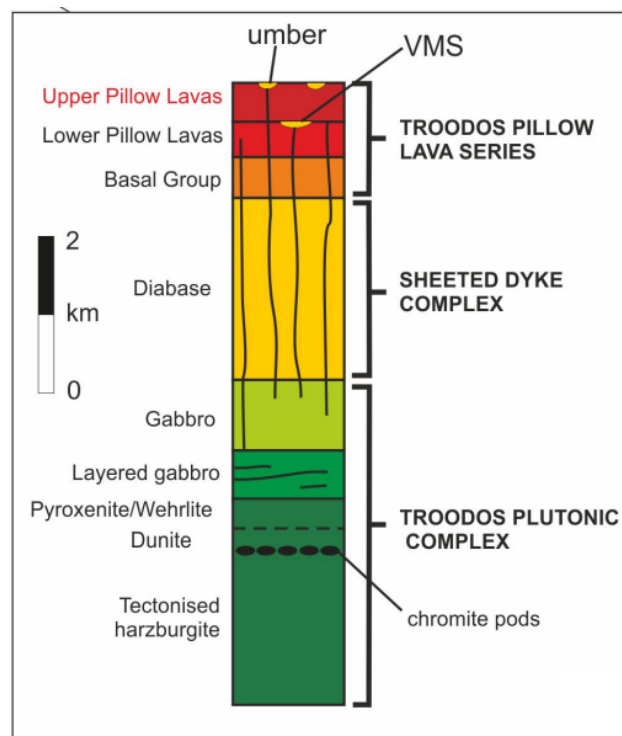


Figure 9 Stratigraphic cross-section of the Troodos ophiolite complex, from its mantle section to the uppermost pillow lava units. From (Fonseca et al., 2017)

2 Methods

2.1 Study region

Copper in particular has been mined from sulphide deposits since ancient times on the island of Cyprus. These sulphide deposits are divided into five major mining districts, namely Skouriotissa, Limni, Kalavassos, Mitsero and Tamassos. The deposits on Cyprus have been exploited economically to varying degrees over time. As the reserves depleted and a collapse in commodity prices set in, the mining industry began to decline in the 1980s (Adamides, 2010a).

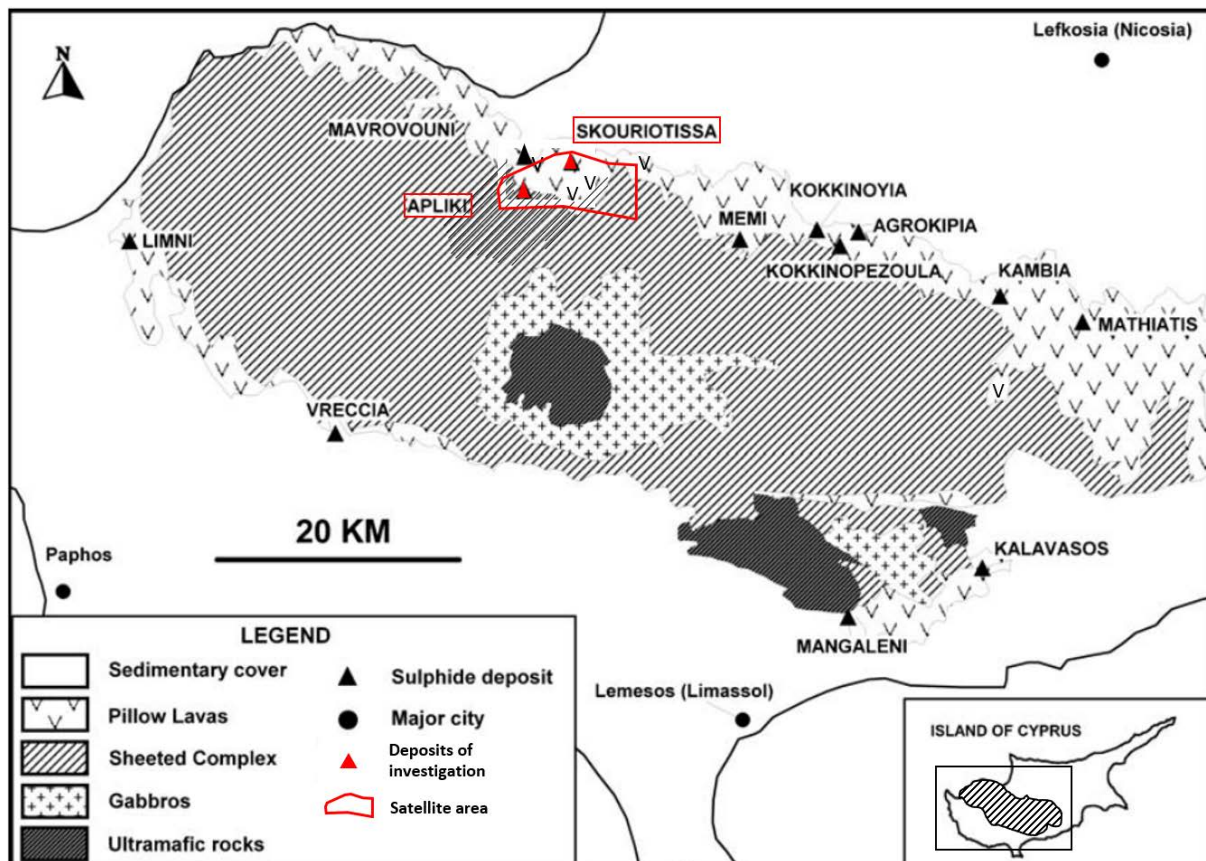


Figure 10 Geological map of the Troodos ophiolite showing locations of major sulphide deposits. Adapted from Adamides, 2010a.

2 Methods

2.1 Study region

2.1.1 Skouriotissa

The Skouriotissa open pit mining area includes the pits Phoenix, Phoukasa and Three Hills (Figure 11).

The deposits on the island of Cyprus can be divided into two main classes. Those that show clear evidence that hydrothermal fluids have reached the seabed, resulting in the formation of massive sulphides in the form of exhalative lenses. Phoukasa is a representative of this. Indications of exhalative formation are provided by sedimentary structures as well as signs of weathering of the sulphide on the seabed. In addition, remains of bottom-dwelling organisms such as gastropods and vestigial worms can provide indications.

The second type of deposit is usually surrounded by extensive zones of hydrothermally altered rock, which are then filled inwards with mineralised rock. The Three Hills and West Apliki pits provide indications of this type of formation. There was an interaction between the hydrothermal fluids and the surrounding seawater, which led to sulphide mineralisation.

In addition to these two classes, there are also deposits that were formed differently. This is the case with Phoenix, which is assumed to have been formed during supergene enrichment of an originally copper-poor zone by submarine mining of part of the Phoukasa massive sulphide lens.

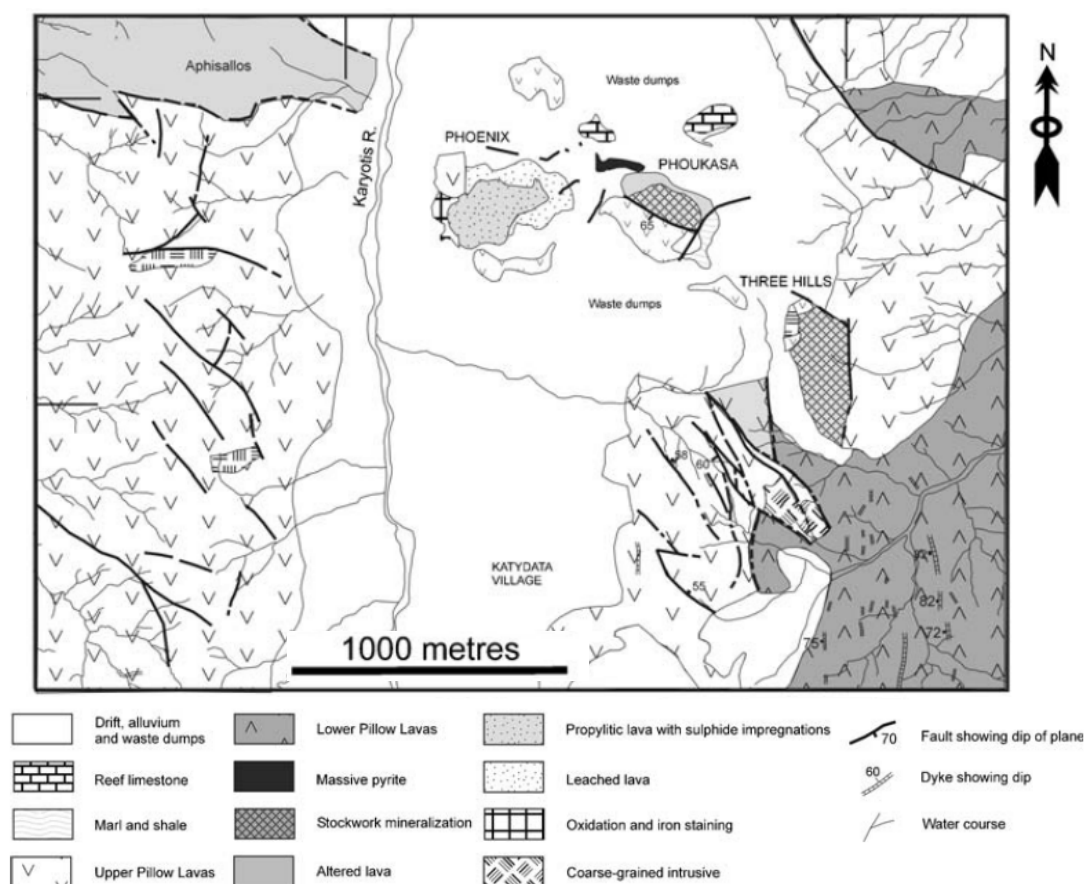


Figure 11 Geological map of the Skouriotissa area. Marked locations of the pits Phoenix, Phoukasa and Three Hills and fault zone location from Adamides, 2010b.

2 Methods

2.1 Study region

Table 3 Overview of Skouriotissa pits from Adamides, 2010b, 2010a

Deposit	Phoenix
History	Outlined by Cyprus Mine Cooperation (CMC) during development drilling in the 1960s. Initial test exploitation by CMC using pressure leaching. Followed hydrometallurgical exploitation by Hellenic Copper Mining Ltd. (HCM). 40 mt geological resource, 0.4%Cu
Tonnage and grade Mineralization Type	Disseminated and vein-type mineralisation in chlorite-bearing pillowed lavas, with copper mainly represented by secondary minerals, particularly chalcocite, native copper and delafossite (Cu, Fe oxide). Pyrite is commonly coated by chalcocite. None apparent
Structural control	Upper part of the Upper Pillow Lavas. The deposit was partly overlain by
Stratigraphic position	sedimentary rocks
Geographical signature	Located within region of low magnetic intensity
Deposit	Phoukasa
History	Detected by drilling in 1914. The deposit was mined by underground methods until 1960, thereafter followed by open-cut mining. Mining of the stockwork zone of the deposit was planned by HMC (as Adamides, 2010b, 2010a)
Tonnage and grade Mineralization Type	6 mt, 2.25%Cu, 46%S Massive sulphide lens composed of pyrite and chalcopyrite, overlain by pyritic chert, with limited supergene enrichment at the upper levels associated with submarine weathering and formation of ochre. A pipe-like stockwork zone underlies the deposit which laterally away
Structural control	None apparent
Stratigraphic position	Top of the Upper Pillow Lavas
Geographical signature	Located within region of low magnetic intensity
Deposit	Three Hills
History	Detected by drilling in area of alteration and weak oxidation. Explored by adit and cross-cut. Presently mined by HCM (as Adamides, 2010b, 2010a)
Tonnage and grade Mineralization Type	6.2mt, 0.37% Cu Vein type deposit composed of pyrite and chalcopyrite, with limited supergene enrichment at the upper levels (chalcocite and covellite)
Structural control	North-northwest-striking structures
Stratigraphic position	Within Upper Pillow Lavas surrounded by chloritic alteration envelope
Geographical signature	Located within region of low magnetic intensity

2.1.2 Apliki

The Apliki copper deposit is part of the Skouriotissa mining district. In the 1960s, open-pit mining of this deposit began, operated by Cyprus Mines Corporation (CMC), which stopped in 1974 due to the Turkish invasion. The abandonment of the mine left a deep crater in which an acid mine lake is now present (Adamides, 2010a). This is supplied by surface runoff and has inputs from the surrounding mineralised zone and the adjacent basaltic pillow lavas. The bottom of the open pit is at an elevation of about 200m a.s.l., the mineralised zone at about 330m a.s.l..

The main magmatic mineral components are plagioclase, Pyroxene (Augite), Magnetite and Ilmenite, and rarely Olivine. Celadonite, Calcite, Analcime and Quartz occur in the rock matrix as secondary minerals. The predominant ore minerals are Pyrite, Marcasite and Chalcopyrite, the main gangue minerals are Bornite, Sphalerite, Galena and Barite together with Quartz. Goethite, Hematite, Chalcocite, Covellite and Fe, Cu, Pb, Al and Ca- sulphates also occur, which were formed in the supergene environment (Antivachis, 2015).

Table 4 Overview of Apliki pits from Adamides, 2010b, 2010a

Deposit	Apliki
History	Detected by CMC during gold exploration in the 1930s. Mined initially underground, followed later by opencut mining. Operations ceased in 1973, however low-grade resource remains.
Tonnage and grade	1.65 mt, 1.8%Cu, 36.0%S
Mineralization Type	Massive sulphide, with underlying stockwork in chlorite-bearing and silicified lavas
Structural control	Graben structure defined by two north-striking faults
Stratigraphic position	Contact between Lower and Upper Pillow Lavas Minor north-striking magnetic low
Geographical signature	Minor north-striking magnetic low
Deposit	West Apliki
History	Detected and explored by CMC by drilling on gossans (as Adamides, 2010b, 2010a)
Tonnage and grade	3.6 mt, 0.34%Cu (Geological resource)
Mineralization Type	Stockwork-type mineralisation of pyrite and chalcopyrite with significant supergene minerals, particularly chalcocite at higher levels. The deposit is surrounded by silicified and brecciated chlorite-rich lavas with abundant jasper and epidote veining and cavity fillings Intersection between north- and east-trending structures
Structural control	Intersection between north- and east-trending structures
Stratigraphic position	Within the Lower Pillow Lavas, close to the contact with the Basal Group
Geographical signature	Within region of low magnetic intensity

2.2 Study design

2.2.1 Data sampling

Dataset 1: Laboratory Reference Sample Mosaic

Dataset 1 is a laboratory mosaic which consist of 40 hyperspectral measured mineral scans, each 50 by 50 pixels (Figure 12). 5 different SIMs are represented in 25 mosaic tiles to capture mineral heterogeneity. Also included are 7 minerals, each with 1 to 2 samples, which are typical of the island of Cyprus and are not SIMs. Dry, fresh, and heavy metal contaminated vegetation samples are also included to train and excluded for vegetation in the classification process. The mosaic forms the laboratory data set on which the identification and classification method is developed and tested. Figure 12 shows the arrangement of each sample in the mosaic and Table 5 provides more information about the samples. The samples were provided by the University of Potsdam (UP) and the mineral archive of the Federal Institute for Geosciences and Natural Resources (BGR).

The images were taken with the HySpex cameras system. The line scanner generates an image, which in each pixel represents the spectrum of the wavelength range from 400 - 2500 nm. Detailed and further information about the system and usage of the sensor can be found in Herrmann, 2019; Körting, 2016; Rogass et al., 2017. A short introduction is also given in the appendix.

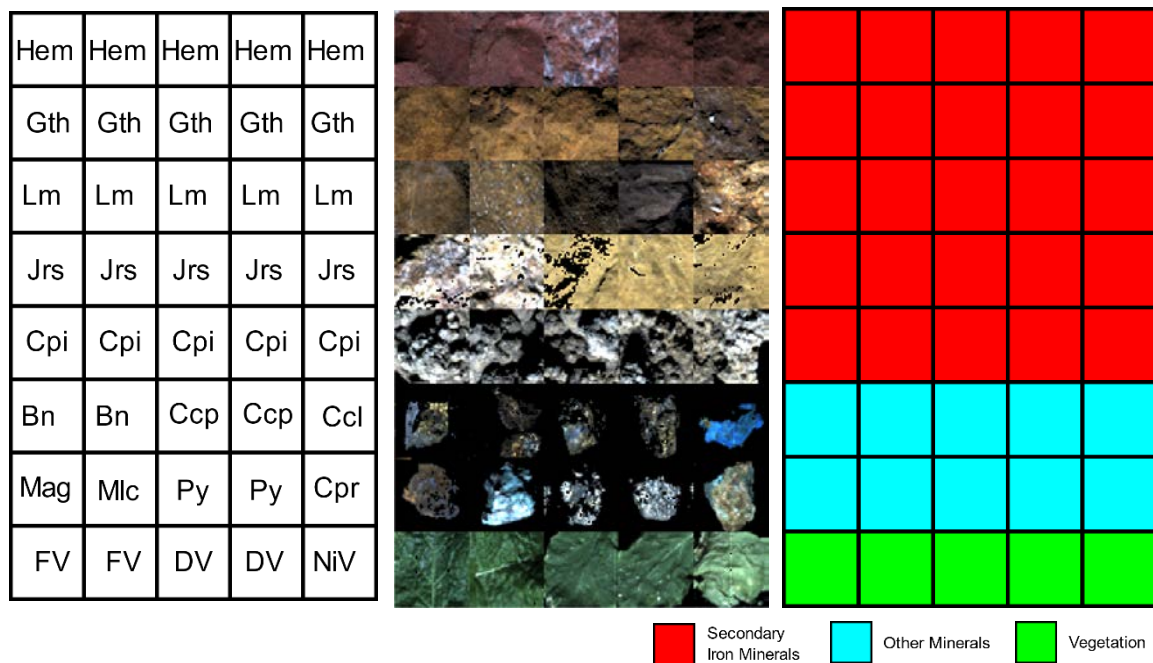


Figure 12 **Left:** Position of the different samples in the mosaic. Abbreviations of the individual minerals, to be found in Table 5. **Middle:** RGB representation of the laboratory data set. **Right:** Color-coded differentiation by sample type.

2 Methods

2.2 Study design

Table 5 Overview of mineral samples used. Abbreviations according to International Mineralogical Association – Commission on new Minerals Nomenclature and Classification (IMA-CNMNC) approved mineral symbols and formular. SIMs are highlighted in red, other minerals in blue and vegetation samples in green.

Name	Abbreviation	Formula	Chemical elements (Mass in %)
Goethite	Gth	$\alpha\text{-FeOOH}$	Fe (63.9), O (36), H (1.1)
Limonite	Lm*	FeO(OH)	Fe (52.3), O (44.9), H (2.8)
Hematite	Hem	Fe_2O_3	Fe (69.9), O (30)
Jarosite	Jrs	$\text{KFe}_3(\text{SO}_4)_2(\text{OH})_6$	O (44.7), Fe (33.5), S (12.8), K (7.8), H (1.2)
Copiapite	Cpi	$\text{Fe}^{2+}\text{Fe}_4^{3+}(\text{SO}_4)_6(\text{OH})_2$	O (58.9), Fe (22.3), S (15.4), H (3.4)
Pyrite	Py	FeS_2	S (53.5), Fe (46.6)
Magnetite	Mag	$\text{Fe}^{2+}\text{Fe}_2^{3+}\text{O}_4$	Fe (72.4), O (27.6)
Malachite	Mlc	$\text{Cu}_2(\text{CO}_3)(\text{OH})_2$	Cu (57.5), O (36.2), C (5.4), H (0.9)
Cuprite	Cpr	Cu_2O	Cu (88.8), O (11.2)
Chrysocolla	Ccl	$(\text{Cu}_{2-x}\text{Al}_x)\text{H}_{2-x}\text{Si}_2\text{O}_5(\text{OH})_4$	O (48), Cu (28.6), Si (16.9), Al (4.1), H (2.4)
Chalcopyrite	Ccp	CuFeS_2	S (34.9), Cu (34.6), Fe (30.4)
Bornite	Bn	Cu_5FeS_4	Cu (63.3), S (25.6), Fe (11.1)
Fresh Vegetation	FV		C, H, O
Dry Vegetation	DV		C, H, O
Vegetation	NiV		C, H, O (contaminated with heavy metal nickel)

Dataset 2: Laboratory Field Sample Validation Mosaic

For validation purposes, a mosaic was created with samples for which the mineral composition was determined using X-ray diffraction (XRD). The composition of the different mineral phases is summarised in Table 6. The samples, sample scans and XRD results are subjects of a current doctoral thesis and were made available by Nicole Köllner as part of this work. They are field samples that realistically represent unconsolidated rocks that can be found on mining site in the Republic of Cyprus (Figure 13).

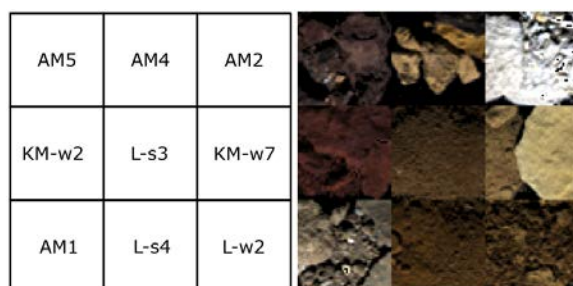


Figure 13 **Left:** Short-names of the samples. **Right:** RGB representation of the samples in Mosaic. The samples named AM and KM come from the island of Cyprus. AM are from the Agropikia mine and KM from the Kokkinopezoula mine. The samples beginning starting with L are from Lausitz, Germany.

2 Methods

2.2 Study design

Table 6 Results of the XRD analysis [%]. Distribution of the volume percentages among the minerals Hematite, Goethite and Jarosite. For the analysis and assessment, the mineral phases Jjarosite, Natrojarosite and Hydroniumjarosite were added together.

Sample	AM5	KM-w2	AM1	AM4	L-s3	L-s4	AM2	KM-w7	L-w2
Hematite	14.1	33.8	1.2						
Goethite	57.1		12.6	78.8	67.7	80.3			56.5
Jarosite			3.4	5.3	27.6		60.1	99.1	39.8
Pyrite			5.7						
Quartz	10	1.4	20.1	15.9	4.8	5.7	1.3	0.9	3.7
Clinochlore			36.5						
Microcline			10.1						
Gypsum			10.5				11.5		
Natrojarosite		35.2					27.1		
Montmorillonite									
Cristobalite		29.6							
Hydronium-jarosite						14.0			

Dataset 3: Satellite Field Data

In the following section, the two satellite sensors used in this work are described. The sensor itself and its properties are briefly explained, and the datasets used in this work are presented.

WorldView-3

After the launch of WorldView-1 in 2007, WorldView-2 launched 2009 and had a high resolution 8-band (VNIR) multispectral sensor equipped (Qian et al., 2014). WorldView-3 (launched in 2014) improved the spatial resolution of the 8 VNIR bands of WorldView-2 and also had 8 bands in the SWIR wavelength region on board. The exact specifications of the sensors are summarised in Table 7.

Table 7 Summary of WorldView-2 and WorldView-3 SWIR sensor characteristics after (Qian et al., 2014).

WorldView-2 (VNIR)				
Band		Central wavelength [nm]	Bandwidth [nm]	Spatial resolution [m]
Number	Name			
1	Coastal	425	50	1.8
2	Blue	480	60	1.8
3	Green	545	70	1.8
4	Yellow	605	40	1.8
5	Red	660	60	1.8
6	Red Edge	725	40	1.8
7	NIR 1	832.5	125	1.8
8	NIR 2	950	180	1.8
WorldView-3 (SWIR)				
9	SWIR 1	1210	30	3.7
10	SWIR 2	1570	40	3.7
11	SWIR 3	1660	40	3.7
12	SWIR 4	1730	40	3.7
13	SWIR 5	2165	40	3.7
14	SWIR 6	2205	40	3.7
15	SWIR 7	2260	50	3.7
16	SWIR 8	2330	70	3.7

The WorldView-3 satellite image in this work is synthetically produced from a WorldView-2 VNIR dataset (8 bands) and a WorldView-3 SWIR dataset (8 bands). The reason for this was that the VNIR data was obtained from the archive and the SWIR data was recorded on request. The VNIR image was provided by European Space Imaging® granted within the third-party mission (TPM) with the project ID 61058 by the European Space Agency (ESA). The time of recording of the VNIR archive data was the

2 Methods

2.2 Study design

15/08/2019 at 8:58 am and the delivered pixel size is 2 m x 2 m. The SWIR image was provided within the same project. The time of recording of the newly collected SWIR data was 12/09/2020 at 8:50am and the pixel size provided is 3.7m x 3.7m.

The VNIR and SWIR data were each corrected with ATCOR version 9.3.0 © DLR/ ReSe 2019, IDL 8.5 (Richter and Schläpfer, 2011) and then stacked into one image. The data is projected in EPSG: 32636 - WGS 84 / UTM zone 36N. Further metadata of the images can be found in Table 8. An RGB representation of the satellite image is presented in Figure 14.

Table 8 Further metadata of the WorldView-2 (VNIR) and WorldView-3 (SWIR) images in comparison.

	WorldView-2 VNIR	WorldView-3 SWIR
date of acquisition	15/08/2019; 8:58	12/09/2020; 08:50
TPM project ID	61058	61058
cloud cover	0.007	0.000
solar azimuth	146.2°	154.8°
solar zenith	24.1°	33.4°
pixel size	2 m	3.7 m
projection	EPSG: 32636 - WGS 84 / UTM zone 36N	

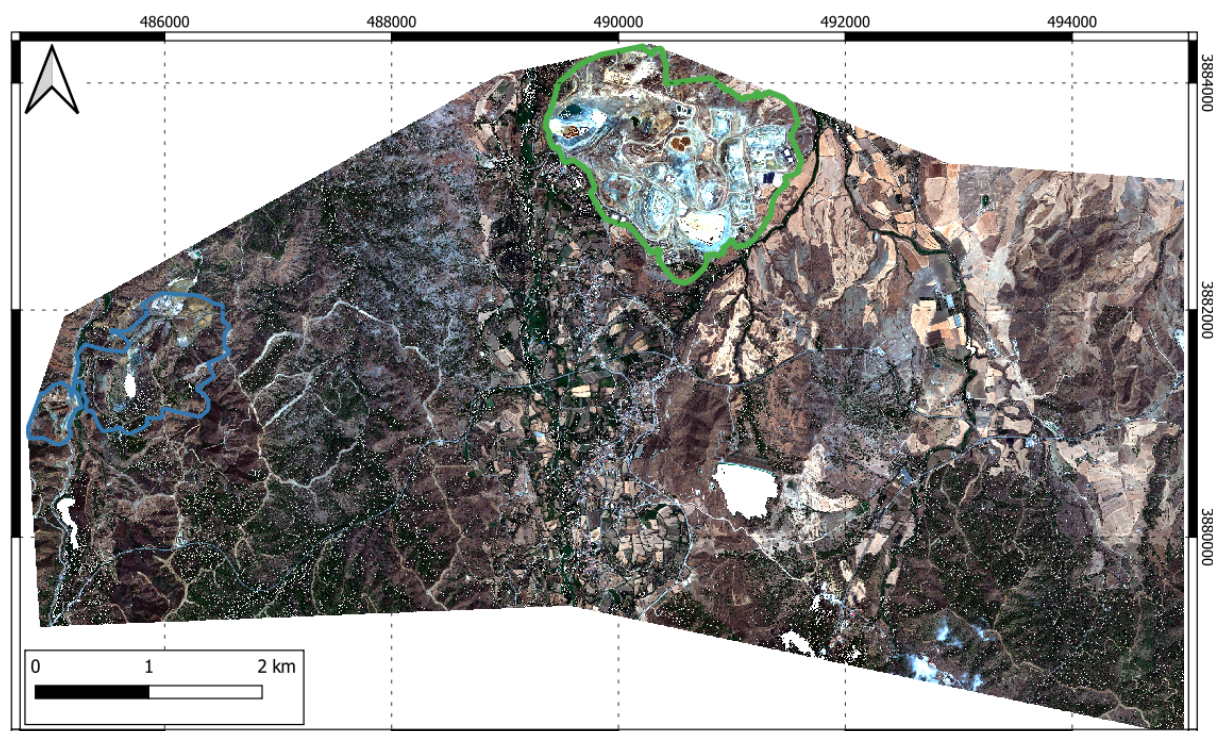


Figure 14 RGB representation of the WorldView-3 satellite image (R: band 5, G: band 3, B: band 2). Skouriotissa Mine marked in green, Apliki Mine marked in blue.

2 Methods

2.2 Study design

Sentinel 2

Sentinel 2 data is freely available via the USGS Earth Explorer (Earth Explorer; 2000) or the Copernicus Open Access Hub. Level-1C (L1C) data was acquired. With the open-source processing software Sen2Cor they were corrected from the effects of the atmosphere and converted into a Level-2A (L2A) surface reflectance product (Louis et al., 2016).

The Sentinel 2 satellite image was taken by the Sentinel-2A sensor on 12/08/2019 and cropped to the same extent as the provided WorldView-3 image. The multispectral image originally consists of a total of 12 bands, which have different resolutions, properties and functions. These 12 bands have been reduced to 9 bands with a resolution of 20x20 meters. The original and selected bands (bold) are listed in Table 9. An RGB representation of the satellite image is presented in Figure 15.

Table 9 Overview of the Sentinel-2A bands and specifications. Since not all bands are used, the layer numbers shift; these are included here for clarity. (ESA, 2022).

Sentinel 2A						
Original Number	New Number	Name	Central wavelength [nm]	Bandwidth [nm]	Spatial resolution [m]	Usage
1		Band 1 – Coastal aerosol	442.7	21	60	Aerosols
2	1	Band 2 – Blue	492.4	66	10	Aerosols, Land use, vegetation
3	2	Band 3 – Green	559.8	36	10	Land Use, Vegetation
4	3	Band 4 – Red	664.6	31	10	
5	4	Band 5 – Vegetation red edge	704.1	15	20	
6	5	Band 6 – Vegetation red edge	740.5	15	20	
7	6	Band 7 – Vegetation red edge	782.8	20	20	
8		Band 8 – NIR	832.8	106	10	Water Vapour, Land Use, Vegetation
8a	7	Band 8A – Narrow NIR	864.7	21	20	
9		Band 9 – Water vapour	945.1	20	60	Water Vapour
10		Band 10 – SWIR – Cirrus	1373.5	31	60	Cirrus Clouds
11	8	Band 11 – SWIR	1613.7	91	20	Land Use, Vegetation
12	9	Band 12 – SWIR	2202.4	175	20	Aerosols, Land Use, Vegetation

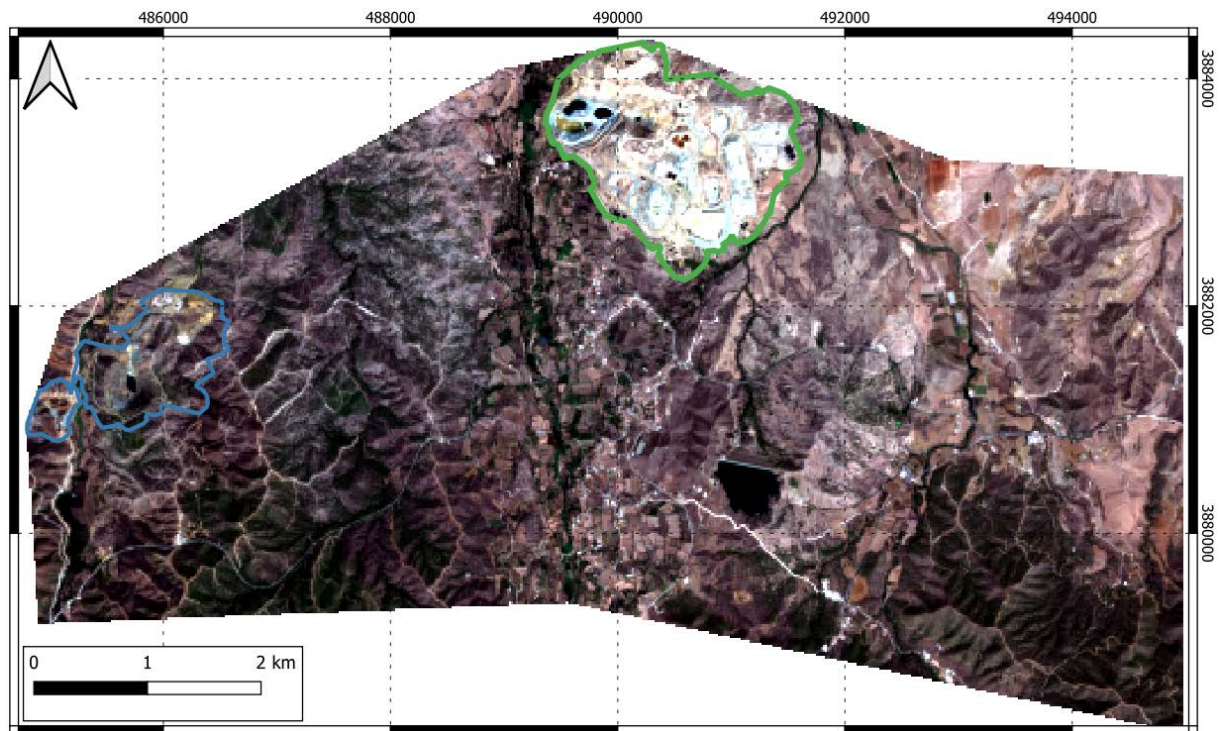


Figure 15 RGB representation of the Sentinel-2A satellite image (R: band 3, G: band 2, B: band 1). Area was cropped from the extent of the WorldView-3 section provided. Skouriotissa Mine marked in green, Apliki Mine marked in blue.

2.2.2 Data processing

The hyperspectral laboratory data (datasets 1 and 2) were all pre-processed the same extend. A so-called detector jump between VNIR and SWIR was corrected, defective bands and strong noise were interpolated and the spectral profile was slightly smoothed. These data sets were then resampled to the spectral resolutions of WorldView-3 and Sentinel-2 to simulate laboratory data of these sensors. Datasets 3 are originally top-of-atmosphere radiance data and were therefore atmospheric corrected. The software Sen2Cor version 2.10 was used for Sentinel-2, for WorldView-3 ATCOR version 9.3.0 was used. In addition to the 16 and 9 bands/layers of all three datasets, and for both sensors, 4 further layers were added, namely the output layers from the ferric iron index, ferrous iron index, ferrous silicates index and ferric oxides index. These were each calculated from their own data sets.

X-ray diffractometry was performed for the samples in Datasets 2, and they were additionally analysed semi-quantitatively with the Rietveld method. The mineralogy for each sample is presented in Table 6. The single diffractograms can be found in the appendix as images (page 77). The XRD analysis was provided and carried out at the University of Potsdam. The principles of the XRD analysis are briefly explained in the appendix (page 76).

2.3 Analyses

2.3.1 Overview of applied workflow

The methodological workflow was divided into two parts (Figure 16). The laboratory data part, consisting of the training datasets (Datasets 1) and validation datasets (Datasets 2), and the satellite image application with the satellite scenes (Datasets 3). The respective datasets existed in two spectral resolutions, namely WorldView-3 and Sentinel-2. In the first step, masks were developed (I) and then two RF models were trained with the data from datasets 1 (II). These RF models were then applied to datasets 2 and 3 in an RF classifier (III). They are explained in the following sections in detail (I-III).

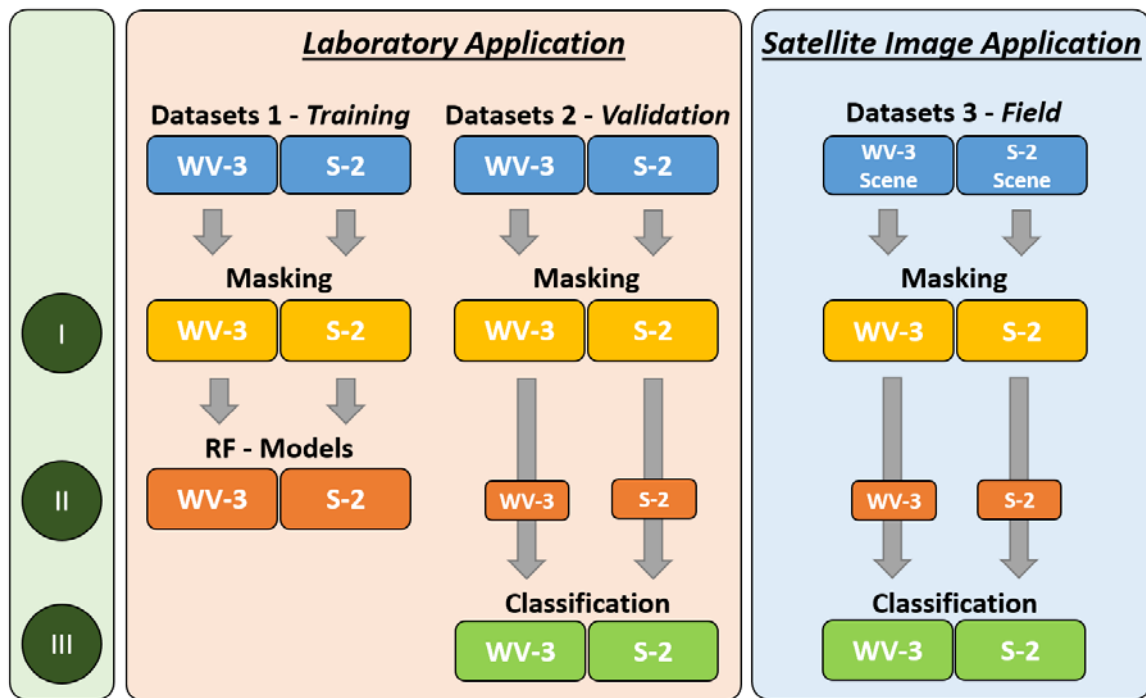


Figure 16 Overview of applied workflow. Laboratory Application highlighted in red, Application on satellite images in blue background color.

2.3.2 Detailed workflow description

[I] Masking Process

This step includes the application of indices and thresholds that are supposed to remove unwanted pixels in the image analysis. For this purpose, the data set is masked with three different masking approaches in sequence. In the following the indices and their function are explained.

1. Shadow/ Dark Pixel Removal and Vegetation Masking

In a first step all dark pixels with low signals were masked out. Then as a first index the NDVI was used to identify vegetation which was then masked out as well. Figure 17 shows the NDVI values of the dataset and the resulted image after applying the shadow mask and the NDVI threshold.

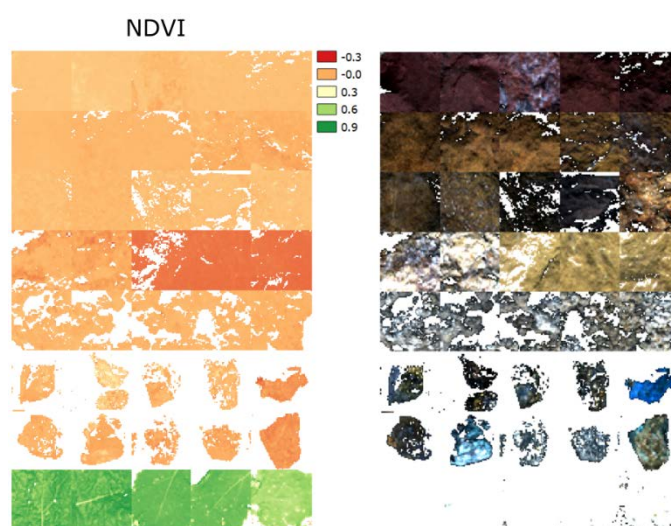


Figure 17 **Left:** NDVI plot of the data set. **Right:** RGB image after the threshold masking.

2. Iron Mask 1 (Ferric Iron Index)

After comparing different iron indices (Figure 18), the ferric iron index was selected finally as the most relevant. It provided the strongest distinction between SIMs and the other minerals in the laboratory data set. The ferric iron index was calculated from each dataset and then masked with a threshold applied.

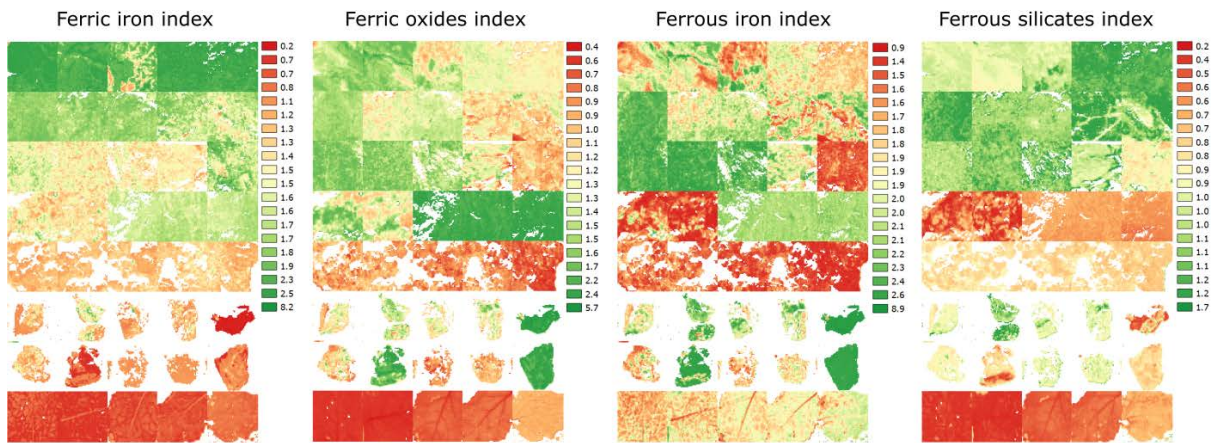


Figure 18 Comparison of the calculated iron-indices.

3. Iron Mask 2 (Iron Feature Band Ratio - IFBR)

The third index is a band ratio consisting of the left shoulder of the large iron absorption feature and the absorption maximum. Figure 19 shows the used bands for the band ratio and Figure 20 shows the calculated index values of Datasets 1 (WorldView-3 spectral resolution). This can exclude pixels that have little or no signal of iron absorption. It can detect most pixels with the spectral characteristics of SIMs. This is applicable to the laboratory datasets and even stronger to the satellite datasets. A detailed explanation of the impact of the indices can be found in the discussion section (4.1 Quality and impacts of the SIM indices, page 52). A list of the formula and bands used for the above-mentioned indices can be found in Table 2 (page 16).

Table 11 shows the thresholds of the applied indices. For each laboratory datasets (Datasets 1 & 2) a different threshold was set. Also for the field data (Datasets 3) a higher and lower value was used to test the results by masking based on a higher and lower threshold of tolerance resulting in a differentiation into low and high confidence areas.

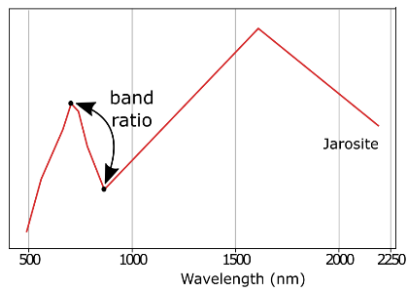


Figure 19 Spectrum of a Jarosite mineral. Marked is the left shoulder point and the absorption maximum, which are used to calculate the IFBR.

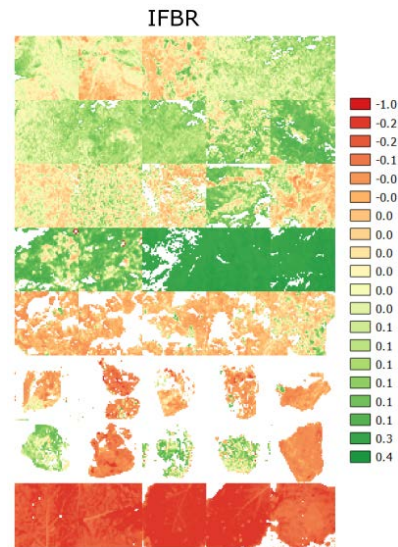


Figure 20 Iron Feature Band Ratio index.

Table 10 Summary of different selected thresholds for different data sets for WorldView-3 and Sentinel-2 resolution.

		Thresholds							
		Dataset 1		Dataset 2		Dataset 3			
		low		high		low		high	
		WV-3	S-2	WV-3	S-2	WV-3	S-2	WV-3	S-2
Filter	NDVI	0.4	0.4	0.4	0.4	0.4	0.4	0.4	0.4
	Fe Index	1.35	1.25	1.2	1.1	1.2	0.5	1.4	0.9
	IFBR	0.005	0.02	0.005	0.01	0.06	0.02	0.1	0.05

[II] Random Forest Classifier

Two random forest classifiers were used in a final analysis to distinguish between the different SIMs in WordView-3 and Sentinel-2 datasets. Due to the masking process most of the Copiapite pixels were removed. This class could not be clearly distinguished from other minerals. Therefore, this class was removed. Tests have shown that the Goethite and Limonite classes showed very similar spectral features, thus making it difficult to distinguish between them. Limonite is not a mineral of its own, rather a mineral mixture of Goethite and Lepidocrocite. For these reasons, the two classes were combined into one class. This means that this class had a total of 10 samples, but still 100 training points like the other two classes. The three remaining classes were Hematite, Goethite/ Limonite and Jarosite.

The masked laboratory data set was used to train a Random Forest (RF) classifier. For this purpose, 100 randomly distributed training points were generated per class (Figure 21). RF is a supervised machine learning algorithm that consists of a large number of individual decision trees that operate as an ensemble. Through a bootstrap aggregated sampling of the training data (with replacement), RF adds randomness to the model as the trees grow. At each node in a decision tree, a random selection of predictor variables is evaluated for their ability to divide the training data into response classes, with the variable that results in the most homogeneous separation being selected (Breiman, 2001; Gibson et al., 2020). Model training and predictions were accomplished using the *randomForest* package in R (v1.2.5033).

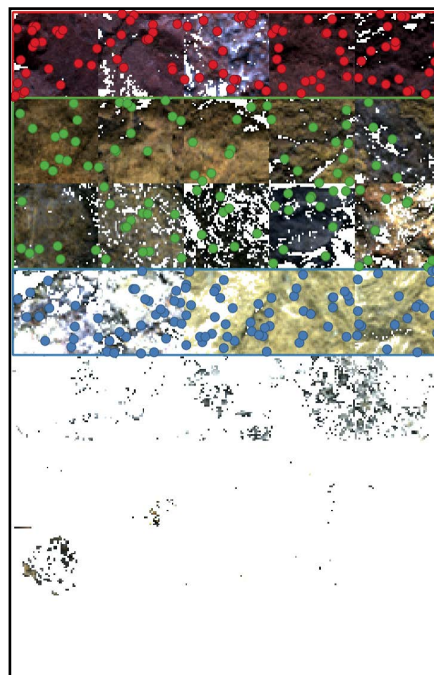


Figure 21 Visualisation of the Laboratory Reference Sample Mosaic (Datasets 1, WorldView-3 spectral resolution as RGB-representation) after applying filters. Random training point locations colored as classes Hematite (red), Goethite / Limonite (green) and Jarosite (blue)

In an initial RF model, the forest was composed of 500 trees, each grown considering the default splitting of the training data and considering 4 randomly selected explanatory variables per tree. Furthermore, the impurity importance of the variables (layers/ bands) is explored in order to assess variable importance of the input features on the classification accuracy (Nembrini et al., 2018). The Mean Decrease Gini Index (MDG) is utilized for this purpose. Based on the MDG index the number of trees was consequently modified. The selection of variables is very important for interpretation and prediction (Hong Han et al., 2016), and therefore only the most informative layers should be used (Table 11). The MDG index averages the total decrease in node impurities by splitting the variable across all trees. The larger the MDG value, the purer the variable (Hong Han et al., 2016; Nembrini et al., 2018). The layers of the indices ferric iron and ferrous iron have the most importance for the differentiation of the classes. They rank well ahead of the first bands and the other two iron indices.

Table 11 Listing of the most informative layers of the two data sets (WorldView-3 and Sentinel-2). Sorted in descending order by Mean Decrease Gini (MDG).

	WV-3	MDG		S-2	MDG
Bands / Layers (in descending order of importance)	Ferric iron	47.5		Ferric iron	53.8
	Ferrous silicates	39.2		Ferrous silicates	42.7
	Band_3	18.6		Band_2	21.4
	Band_11	9.9		Ferrous iron	13.7
	Band_2	9.2		Band_4	12.0
	Ferrous iron	9.0		Band_1	11.7
	Band_4	8.0		Band_3	11.3
	Band_6	8.0		Band_8	9.5
	Ferric oxides	7.5		Ferric oxides	7.6
	Band_5	7.4		Band_5	6.3
	Band_1	6.7		Band_9	3.6
	Band_12	5.7		Band_6	2.9
	Band_9	3.8		Band_7	2.8
	Band_10	3.2			
	Band_8	3.0			
	Band_16	3.0			
	Band_15	2.7			
	Band_14	2.3			
	Band_13	2.0			
	Band_7	2.0			

This becomes clear in the illustration of the reflectance information of the different classes in Figure 22. Shown here for the WorldView-3 resolution (Figure 22), the same illustration for Sentinel-2 resolution can be found in the appendix (Figure 56, page 83). Especially Jarosite can be easily distinguished from Goethite/ Limonite and Hematite in the first bands (shorter wavelengths). Goethite/ Limonite and Hematite are more similar, here, band 3 is the most distinguishable. These two

classes can be distinguished mainly with the ferric iron index. The graph thus illustrates well what was quantitatively registered within the MDG.

Using the `e1071` package in R studio, the optimal parameters based on the classification accuracy were determined, which resulted from the prediction of a retained portion of the training data. In order to minimise sampling bias, a 5-fold cross-validation was specified, in which the sampling, training and prediction procedure was repeated 5 times. The resulting RF-model was composed of 100 trees and considered 2 randomly selected explanatory variables per tree in the case of the WorldView-3 dataset. As a measure of accuracy, the RF algorithm estimates an out-of-bag (OOB) error (Breiman, 2001, 1996). Here, for each tree a random subset of 70% of the training data was used to build the model with the remaining 30% to test the model in a bootstrap with a replacement method (Gibson et al., 2020). The OOB error for the adjusted RF-models were 2.67% for WorldView-3 and Sentinel-2.

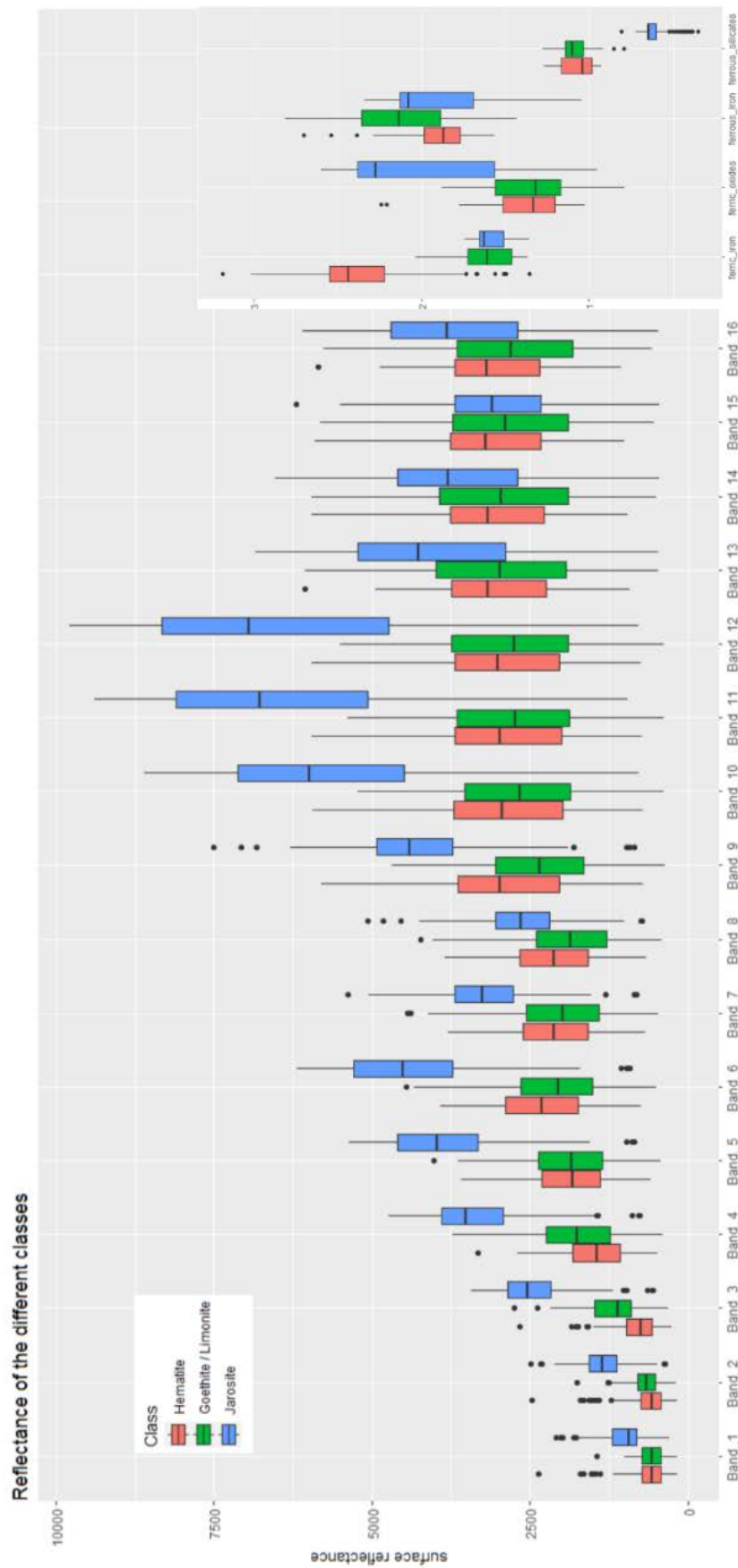


Figure 22 Boxplots of the reflectance of the different sensor bands and indice layers for the three choosen classes for WorldView-3 resolution (16 Bands + 4 layers). This illustration for Sentinel-2 resolution can be found in the appendix.

[III] Classification

The parametrized random forest classifier was applied to the dataset 1 with a predict function. The result is shown in Figure 23. Here, the classes can clearly be separated from each other. There are only some minor misclassifications in the third Hematite sample (top row) and the fourth Limonite sample (third row). It is also noticeable that the remaining Magnetite pixels are classified as Goethite/ Limonite as well as the remaining Copiapite pixels which were also recognised as Jarosite.

The RF-model was also applied to the validation laboratory scan (Datasets 2), as well as the WorldView-3 and Sentinel-2 (Datasets 3) satellite images. A statistical accuracy assessment was made for validation which will be presented in the following section.

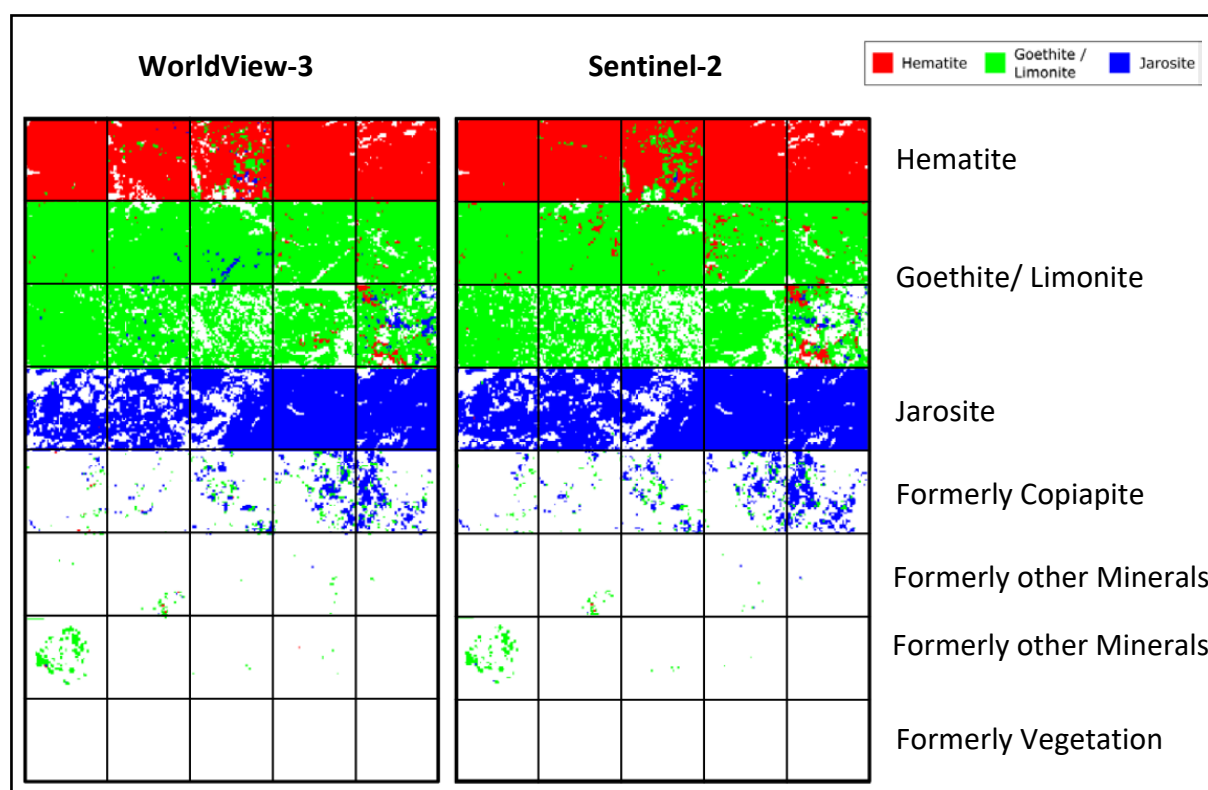


Figure 23 Classification of the mosaic (Dataset 1) to visualise the classification with the RF-model. WorldView-3 spectral resolution on the left, Sentinel-2 spectral resolution on the right. Hematite (red), Goethite/ Limonite (green) and Jarosite (blue).

3 Results

3.1 Accuracy Assessment of the RF-models

3 Results

The following chapter presents the results of the different classifications, sorted by datasets. Since there are a large number of maps and visual outcomes, the following illustrations are limited to specific parts. Additional illustrations can be found in the appendix (starting from page 74).

3.1 Accuracy Assessment of the RF-models

For validation, 30 randomly distributed pixels were chosen per class (90 in total). Accuracy assignments were performed for each of the WorldView-3 and Sentinel-2 simulated datasets. The RF models of the two sensors performed similarly and had both an overall accuracy of 94.44 %. This dropped by about 1 % when areas were taken into account. As a result, the RF-models of the sensors differed, but only very slightly. For both datasets, the same random points were distributed for validation. Although the classifications differ slightly in their results, it is the same at the validation points, which means that the area unadjusted accuracy is the same. The confusion matrix and accuracy values are shown in Table 12.

Table 12 Accuracy Assessment of the RF-models from both datasets (WorldView-3 and Sentinel-2)

		Reference			Total
		Hematite	Goethite/ Limonite	Jarosite	
Predicted	Hematite	28	2	0	30
	Goethite/ Limonite	2	28	0	30
	Jarosite	0	0	29	30
	Total	30	30	30	90
		Not adjusted overall accuracy			94.44 %
		Area adjusted overall accuracy (WorldView-3)			93.45 %
		Area adjusted overall accuracy (Sentinel-2)			93.62 %

3 Results

3.2 Classification of the Laboratory Field Sample Validation Mosaic

3.2 Classification of the Laboratory Field Sample Validation Mosaic

Figure 24 shows the results of the classification for both datasets. **A** shows the sample names as abbreviations, **B** is a RGB representation of the sample mosaic and **C** and **E** show the classified images in WorldView-3 and Sentinel-2 spectral resolution. **D** and **F** are showing the P-values for each pixel colour coded. The P-values represents how often one of the classes was chosen in the decision tree of the random forest model and lies between 0 and 1 per class. These maps represent the highest value between all three possible classification classes per pixel on a coloured scale and therefore range between 0.34 and 1. It could be assumed that the higher the value, the more accurate the classification is. The lowest value is coloured red, the highest green. The colour centre was placed at 0.5 and is yellow. The choice of colour scale does not change the actual values and is therefore only visual. The colour (green colour shift) is intended to show that at a certain point one of the three classes clearly outweighs the other two.

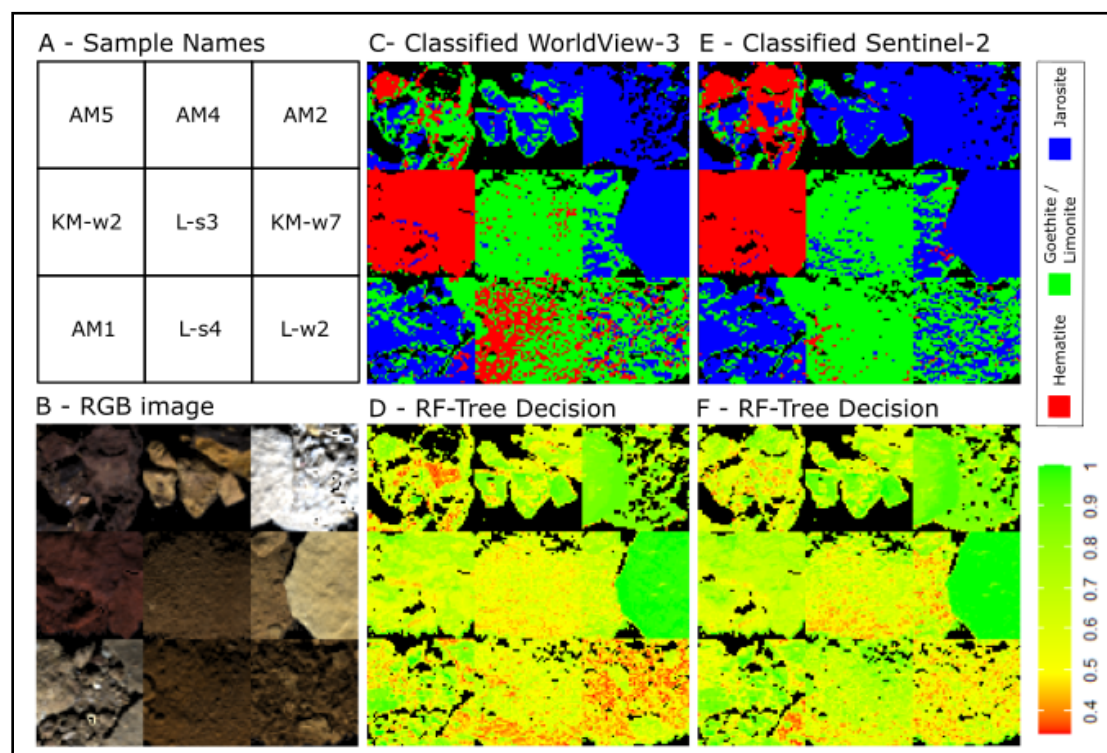


Figure 24 Classification results of the validation laboratory dataset (dataset 2). A: Sample names. B: RGB-representation of the sample mosaics. C: Classification result of the WorldView-3 spectral resolution dataset. D: Classification result of the Sentinel-2 spectral resolution dataset.

The classification results of the mosaic with 9 samples are summarised in the following. Figures of the classification results of both sensors (B & D), as well as the expected result according to the highest XRD value (F) and XRD mixture (G) are presented. In addition, two probability value (P-value) maps are shown for the classification results (C & E).

3 Results

3.2 Classification of the Laboratory Field Sample Validation Mosaic

AM5: XRD analysis of sample AM5 (Figure 25) revealed a mineral mix of Hematite (14.1%) and Goethite (57.1%). In the classification of the resampled data to WorldView-3 and Sentinel-2 characteristics, all three mineral classes (Hematite, Goethite/ Limonite and Jarosite) were classified. Even though no Jarosite was detected in the XRD, many pixels of this mineral were mapped. The proportion of Jarosite pixels is lower in the WorldView-3 dataset. In addition, significantly fewer Hematite pixels are detected here than in the Sentinel-2 dataset, where they occur in significantly higher numbers. The P-value maps show mainly high values for the two images, with the Sentinel-2 dataset showing slightly higher overall values. WorldView-3 shows the pixels with lowest values in the central right of the image. These pixels are classified as Goethite/ Limonite. In the Sentinel-2 dataset, mainly Jarosite was detected in these areas.

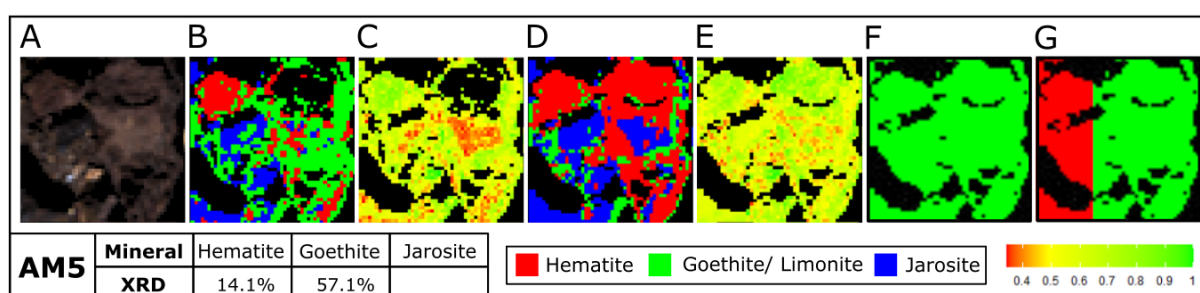


Figure 25 **A:** RGB Representation of the image, **B:** Classified image from WorldView-3 dataset, **C:** P-value Map visualisation, **D:** Classified image from Sentinel-2 dataset, **E:** P-value Map visualisation, **F:** Expected classification result based on highest amount from XRD analysis, **G:** Expected classification result according to proportions from XRD analysis, **Bottom row** (from left to right): Sample number; XRD analysis results for Hematite, Goethite and Jarosite; legend for figures B,D,F and G; legend for figures C and E.

KM-w2: For sample KM-w2 (Figure 26), the XRD analysis showed approximately equal proportions of Hematite (33.8%) and Goethite (35.2%). Both datasets showed almost exclusively as Hematite classified pixels in the classification. A few Goethite pixels were visible in the lower part of the image. A few Jarosite pixels were also detected, in the lower third (Sentinel-2 and WorldView-3), and in the centre (WorldView-3). However, these areas were classified as Hematite dominated. The P-value maps are very similar and showed mostly high to very high values (about 0.65 to 1). A few exceptions were the pixels classified as Jarosite.

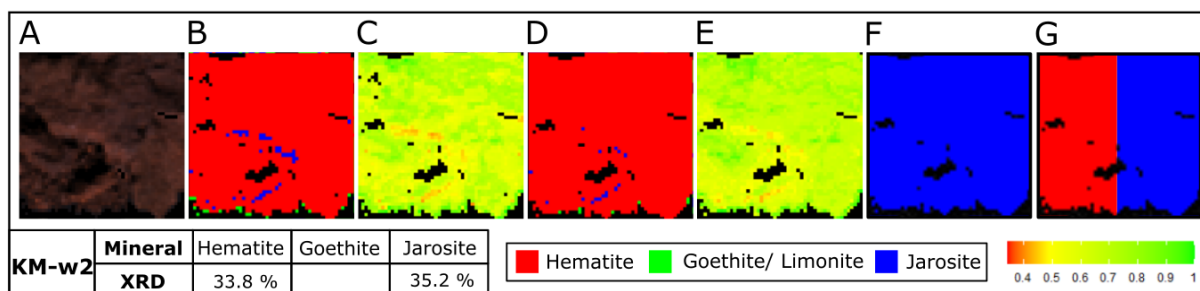


Figure 26 **A:** RGB Representation of the image, **B:** Classified image from WorldView-3 dataset, **C:** P-value Map visualisation, **D:** Classified image from Sentinel-2 dataset, **E:** P-value Map visualisation, **F:** Expected classification result based on highest amount from XRD analysis, **G:** Expected classification result according to proportions from XRD analysis, **Bottom row** (from left to right): Sample number; XRD analysis results for Hematite, Goethite and Jarosite; legend for figures B,D,F and G; legend for figures C and E.

3 Results
3.2 Classification of the Laboratory Field Sample Validation Mosaic

AM1: The XRD analysis determined the lowest proportion of all samples with 17.2 % total content of SIMs in sample AM1 (Figure 27). The remaining 82.8 % are represented by other mineral phases, including Clinochlore (36.5%), Gypsum (10.5%) and Microcline (10.1%), among others (see therefore Table 6, page 27). Goethite formed the largest proportion of the determined mineral phases of SIMs with 12.6%. Jarosite had 3.4% and Hematite 1.2%. Some areas were also identified as Goethite/ Limonite (to a greater extend for Sentinel-2), but the majority were classified as Jarosite pixels. According to the P-value maps, these Jarosite areas were also mostly very clearly identified. Rather the areas of Goethite/ Limonite show lower P-values, which means that here in the RF-model in the decision trees more often different classes were chosen. Some pixels were also classified as Hematite. In both data sets these were mainly located in the lower right part of the image. Here the P-value maps also show the lowest values (especially for Sentinel-2).

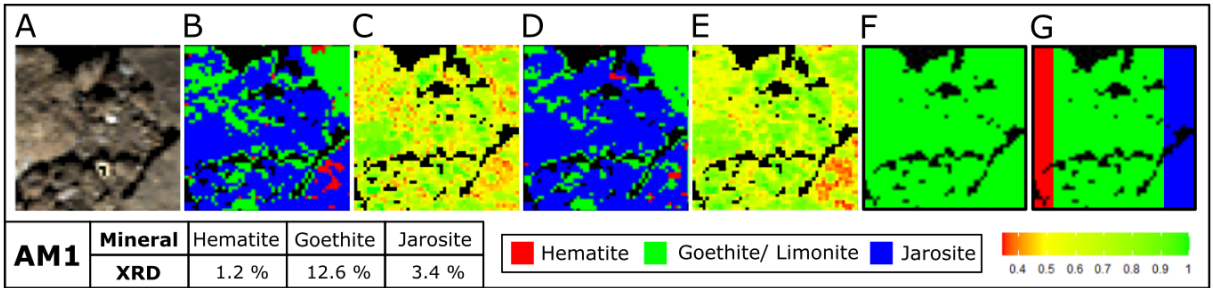


Figure 27 A: RGB Representation of the image, B: Classified image from WorldView-3 dataset, C: P-value Map visualisation, D: Classified image from Sentinel-2 dataset, E: P-value Map visualisation, F: Expected classification result based on highest amount from XRD analysis, G: Expected classification result according to proportions from XRD analysis, Bottom row (from left to right): Sample number; XRD analysis results for Hematite, Goethite and Jarosite; legend for figures B,D,F and G; legend for figures C and F.

AM4: According to XRD, 78.8% Goethite and 5.3% Jarosite were present in Sample AM4 (Figure 28). With the classification mainly Goethite/ Limonite and Jarosite were identified. As in the previous sample (AM1), there was relatively more Goethite than Jarosite in the sample (according to XRD). Both samples came from the same area. Again, the P-value maps show a very clear classification of the Jarosite pixels. Especially in two areas (in the middle part of the images) some Hematite pixels were detected (more in WorldView-3). These areas were close to shadow areas with little reflectance of the material. The P-value maps also show very low values there.

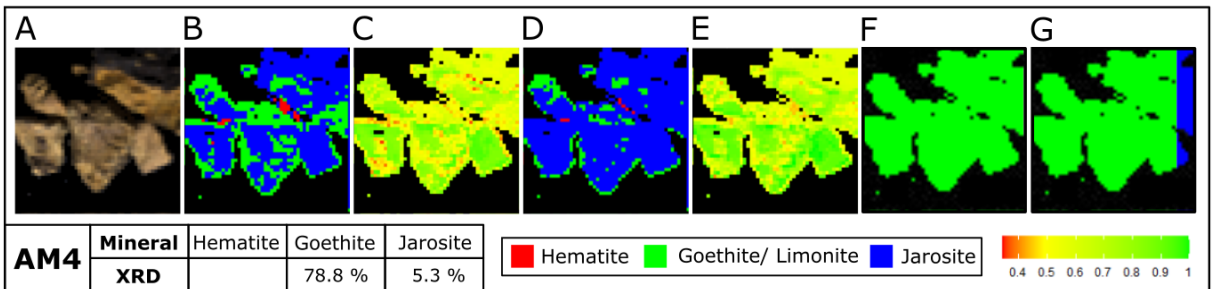


Figure 28 A: RGB Representation of the image, B: Classified image from WorldView-3 dataset, C: P-value Map visualisation, D: Classified image from Sentinel-2 dataset, E: P-value Map visualisation, F: Expected classification result based on highest amount from XRD analysis, G: Expected classification result according to proportions from XRD analysis, Bottom row (from left to right): Sample number; XRD analysis results for Hematite, Goethite and Jarosite; legend for figures B,D,F and G; legend for figures C and F.

3 Results

3.2 Classification of the Laboratory Field Sample Validation Mosaic

L-s3: The XRD analysis of sample L-s3 (Figure 29) showed an approximate distribution of 2/3 Goethite (67.7 %) and 1/3 Jarosite (27.6 %), with 4.7 % belonging to other mineral phases. The classification showed almost exclusively Goethite/ Limonite. In the Sentinel-2 data set, some Jarosite pixels were identified, especially in the lower image area. The P-value map showed the lowest values for the Jarosite pixels. Besides the P-value for Jarosite, which was responsible for the classification decision, the second highest value is interesting. In this case, this was Goethite/ Limonite. Therefore, it could be seen that the predictor oscillated between these two classes. For the WorldView-3 data set, the result was rather different. Very few Jarosite pixels were detected (P-values inconspicuous), but some Hematite pixels.

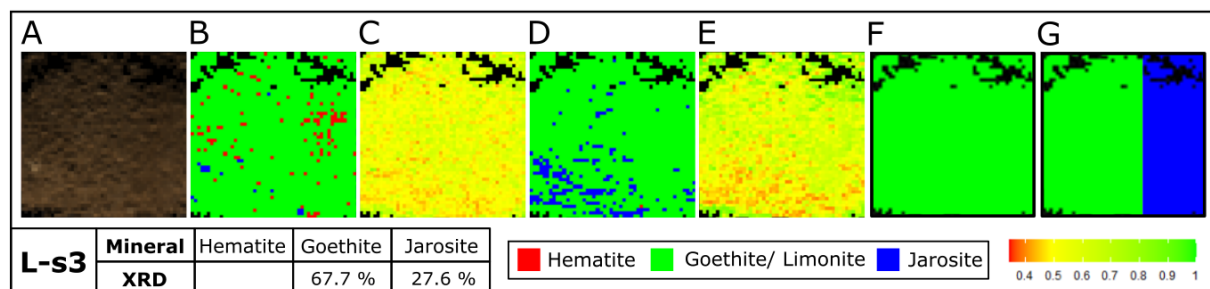


Figure 29 A: RGB Representation of the image, B: Classified image from WorldView-3 dataset, C: P-value Map visualisation, D: Classified image from Sentinel-2 dataset, E: P-value Map visualisation, F: Expected classification result based on highest amount from XRD analysis, G: Expected classification result according to proportions from XRD analysis, Bottom row (from left to right): Sample number; XRD analysis results for Hematite, Goethite and Jarosite; legend for figures B, D, F and G; legend for figures C and E.

L-s4: Sample L-s4 (Figure 31) indicated in the XRD analysis the mineral phases Goethite (80 %) and Jarosite (14 %), and 6 % other “non-SIMinerals”. This was similar to the previous sample L-s3, which according to XRD showed less Goethite and more Jarosite, but in both samples the Goethite portion predominated. Thus, both samples were clearly comparable and came from the same data set as the sample name indicates. The WorldView-3 data set showed similar classification results. However, significantly more Hematite pixels were found in this sample, which is not indicated in the XRD. Classification thus showed approximately a 50/50 ratio of classified Hematite and Goethite/ Limonite pixels. Jarosite was not classified. In sample L-s3 the Sentinel-2 data set did not show this behaviour, but in L-s4 it resembles the WorldView-3 data set. This is because Hematite pixels were also detected here, although in much smaller numbers. There were a few Jarosite pixels as well. When looking at the P-value maps, it was noticeable that pixels with low values tended to be located in the bottom part of the image in both data sets. These are not the pixels that have been classified as Hematite. In addition, this class was often chosen in the RF- model (P-value), which means that this class decision was made with a high degree of certainty.

3 Results

3.2 Classification of the Laboratory Field Sample Validation Mosaic

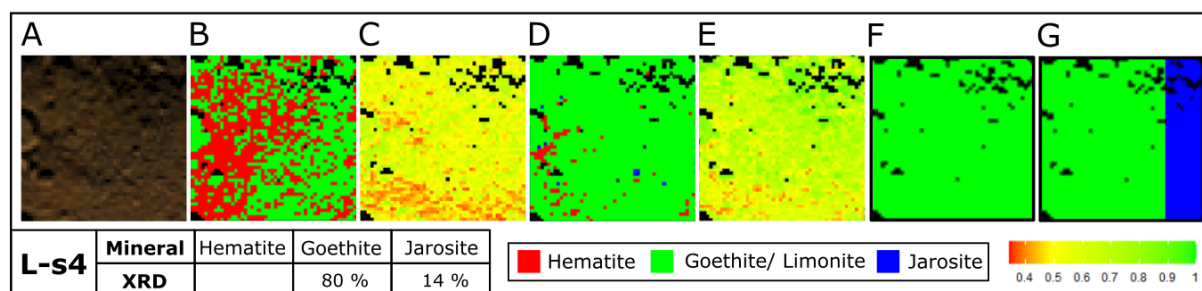


Figure 31 **A:** RGB Representation of the image, **B:** Classified image from WorldView-3 dataset, **C:** P-value Map visualisation, **D:** Classified image from Sentinel-2 dataset, **E:** P-value Map visualisation, **F:** Expected classification result based on highest amount from XRD analysis, **G:** Expected classification result according to proportions from XRD analysis, **Bottom row** (from left to right): Sample number; XRD analysis results for Hematite, Goethite and Jarosite; legend for figures B,D,F and G; legend for figures C and F.

AM2: Sample AM2 (Figure 30) had revealed only Jarosite with 87.2% in the XRD analysis. In both data sets almost exclusively Jarosite was classified, only a few pixels as Goethite/ Limonite and almost none as Hematite. The P-value maps also showed mostly high to very high values. Occasionally, lower values were found where pixels were identified as Goethite/ Limonite and Hematite. These were mainly found near areas covered in shadows.

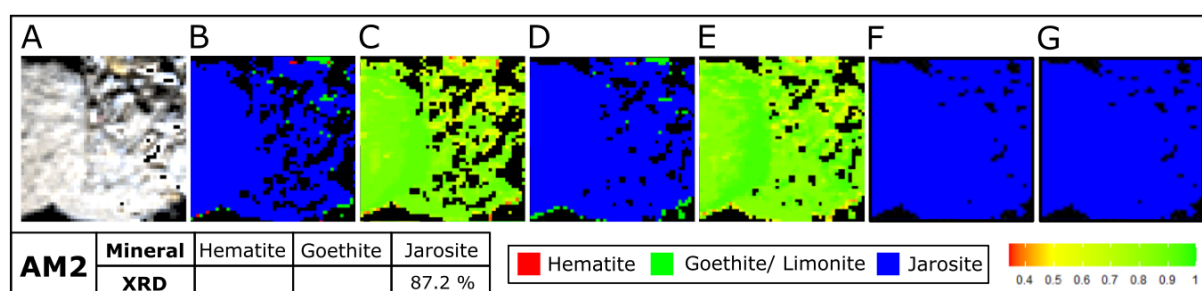


Figure 30 **A:** RGB Representation of the image, **B:** Classified image from WorldView-3 dataset, **C:** P-value Map visualisation, **D:** Classified image from Sentinel-2 dataset, **E:** P-value Map visualisation, **F:** Expected classification result based on highest amount from XRD analysis, **G:** Expected classification result according to proportions from XRD analysis, **Bottom row** (from left to right): Sample number; XRD analysis results for Hematite, Goethite and Jarosite; legend for figures B,D,F and G; legend for figures C and F.

KM-w7: Also in this sample (KM-w7) only Jarosite was detected by XRD analysis (Figure 32) with 99.1 %. In the RGB representation of the sample, it was seen that the sample could be divided into two areas, which could be distinguished by colour and albedo. The right part was completely classified as Jarosite. The P-value maps show the highest values for this area. The left part was identified as Jarosite and also as Goethite/ Limonite. In the Sentinel-2 data set, Hematite pixels were also classified in some places. Both P-value maps show high values for the Jarosite pixels, the differently classified pixels show lower values (~0.5). The sample location on which the XRD measurement took place cannot be traced back at this point of the analysis.

3 Results

3.2 Classification of the Laboratory Field Sample Validation Mosaic

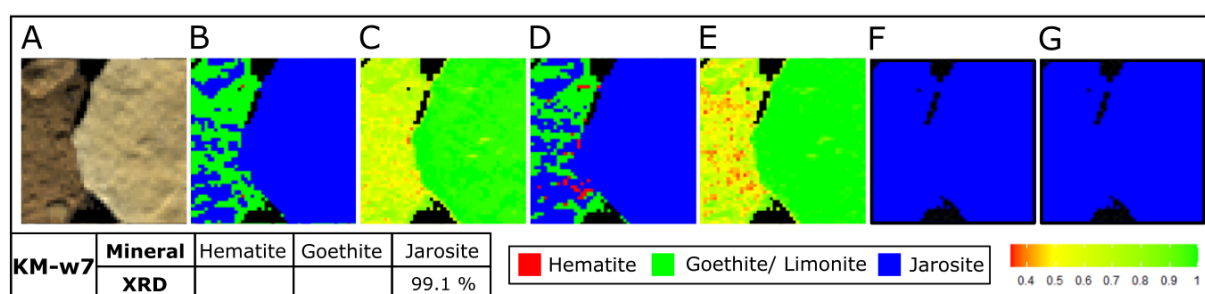


Figure 32 **A:** RGB Representation of the image, **B:** Classified image from WorldView-3 dataset, **C:** P-value Map visualisation, **D:** Classified image from Sentinel-2 dataset, **E:** P-value Map visualisation, **F:** Expected classification result based on highest amount from XRD analysis, **G:** Expected classification result according to proportions from XRD analysis, **Bottom row** (from left to right): Sample number; XRD analysis results for Hematite, Goethite and Jarosite; legend for figures B,D,F and G; legend for figures C and F.

L-w2: According to the XRD analysis, sample L-w2 (Figure 33) was composed of Goethite (56.5%) and Jarosite (39.8%). This was similar to the samples L-s4 and L-s3. Most of the image was classified as Goethite/ Limonite, and there were also many connected areas of Jarosite pixels. The P-values for the classified pixels were rather in the middle range (0.4 - 0.7). In the WorldView-3 dataset, similar areas to those in Sentinel-2 were classified as Jarosite. However, many of the pixels classified there were assigned to the Hematite class. The P-value map also shows significantly lower values overall (<0.4). The lowest values were found in the areas classified as Hematite and Jarosite. The sample (L-w2) consisted of several larger pieces and small powdery material around them. The P-values of these larger pieces are very high compared to the powder.

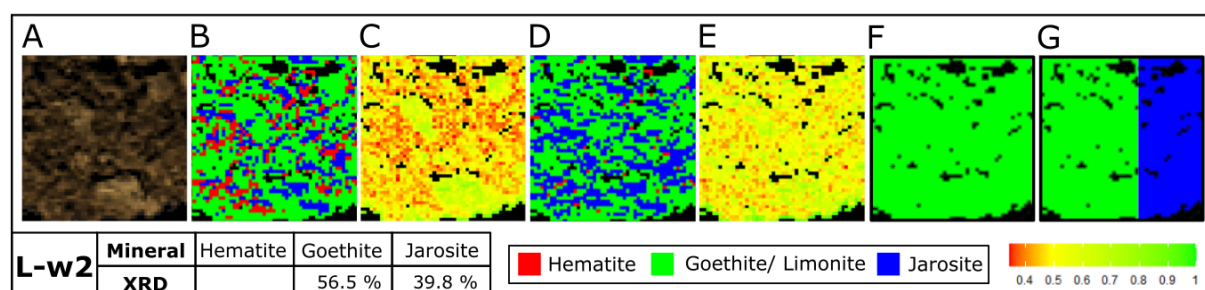


Figure 33 **A:** RGB Representation of the image, **B:** Classified image from WorldView-3 dataset, **C:** P-value Map visualisation, **D:** Classified image from Sentinel-2 dataset, **E:** P-value Map visualisation, **F:** Expected classification result based on highest amount from XRD analysis, **G:** Expected classification result according to proportions from XRD analysis, **Bottom row** (from left to right): Sample number; XRD analysis results for Hematite, Goethite and Jarosite; legend for figures B,D,F and G; legend for figures C and F.

3 Results

3.3 Classification of Satellite Field Data

3.3 Classification of Satellite Field Data

The following part will deal with the results of the satellite image classification of both satellite image scenes. Figure 34 shows the classification results from the WorldView-3 satellite and Figure 35 for Sentinel-2. Detailed views of the two study areas, Skouriotissa and Apliki, are given in the discussion section. With high confidence almost exclusively pixels in the estimated mining areas of Skouriotissa and Apliki were detected. Low confidence pixels were also mostly detected in these areas apart from a few remaining pixels outside the mining areas. After visual inspection in Google Earth Pro (version 7.3.4.8573 (64-bit)), these pixels represent mainly roads and open ground areas. At Skouriotissa Mine it could be observed that more area has been classified around the actual mining pits. These are the areas that, according to Adamides (2010b), consist mostly of mine waste. At the Apliki Mine, the classifier also finds hardly any pixels in the area of the mine pit, but more in the northern part of the mine. Whether this is mine waste remains unclear, according to the available literature and limited information. Both classifications showed similar results for the identified classes. In general, more Hematite pixels have been identified in WorldView-3.

Based on the pixel size of the different satellites and the classified maps, the areas can be calculated where SIMs and potential pH-value contamination occur. These results are listed in Table 13.

Table 13 Overview of estimated area sizes of the different classes and sensors, displayed in ha, calculated by the pixel size of the used sensors.

pH	WorldView-3	Total area			Skouriotissa area			Apliki area		
		low	high	total	low	high	total	low	high	total
>7	Hematite	15.67	7.21	22.88	10.87	5.30	16.17	2.54	0.78	3.32
4.5-6.1	Goethite/Limonite	17.14	8.86	26	11.38	7.05	18.43	3.93	1.04	4.97
2.3-2.6	Jarosite	28.36	17.22	45.58	18.90	15.25	34.15	3.23	0.61	3.84
pH	Sentinel-2	low	high	total	low	high	total	low	high	total
>7	Hematite	4.56	0.88	5.44	3.72	0.8	4.52	0.56	0.04	0.6
4.5-6.1	Goethite/Limonite	32.12	6.12	38.24	20.36	2.76	23.12	7.88	2.08	9.96
2.3-2.6	Jarosite	59.72	27.32	87.04	56.64	26.56	83.2	1.68	0.32	2

3 Results

3.3 Classification of Satellite Field Data

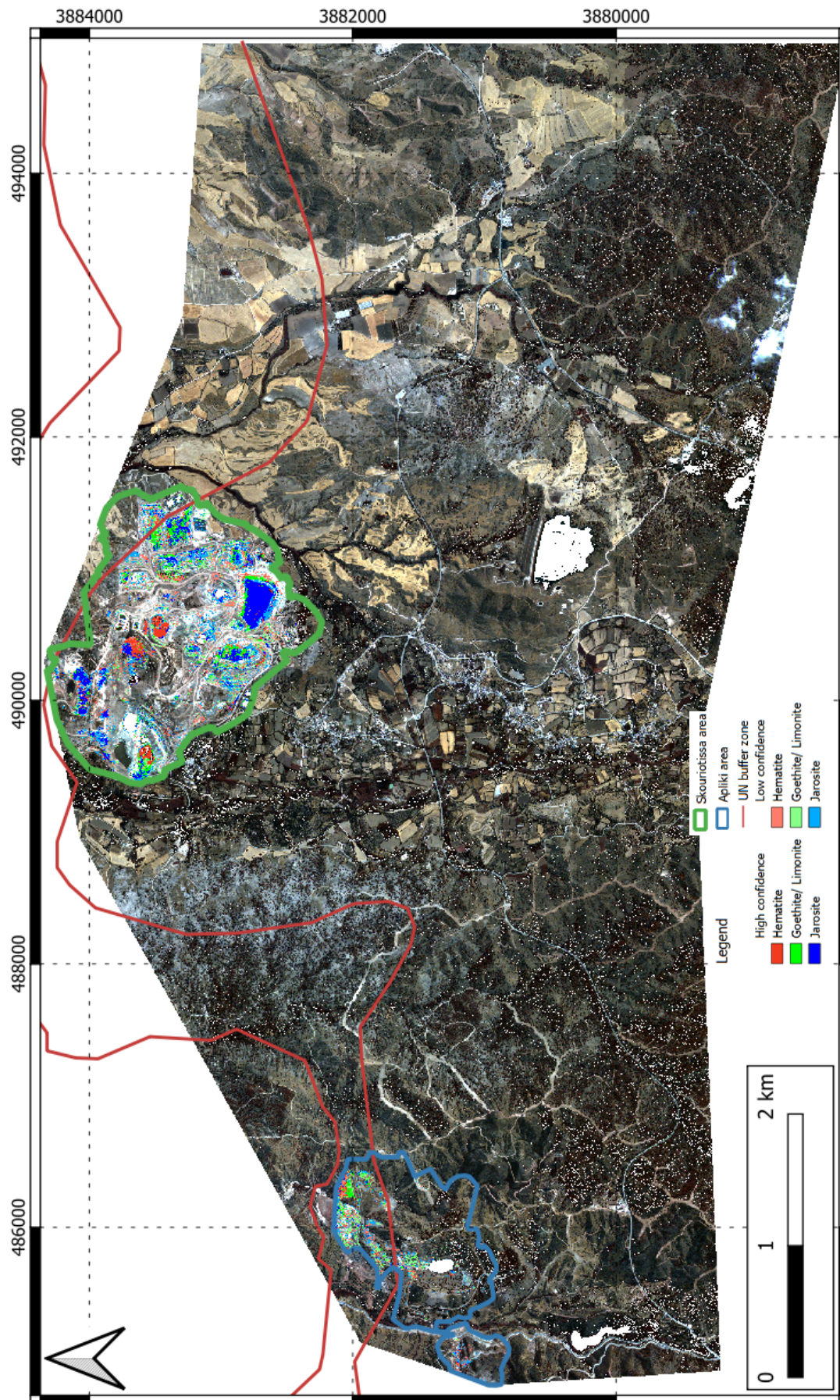


Figure 34 Classification results of the WorldView-3 image.

3 Results

3.3 Classification of Satellite Field Data

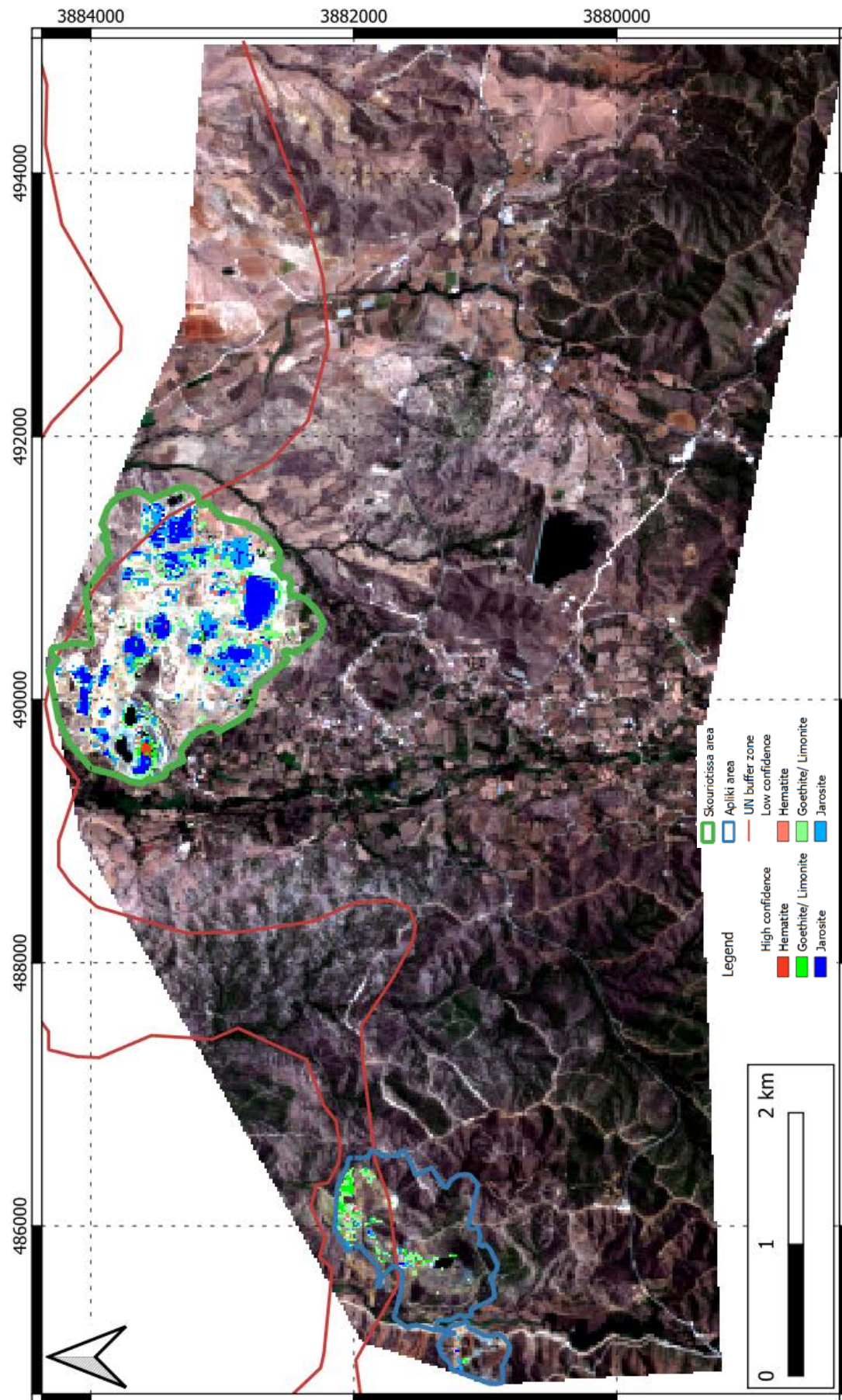


Figure 35 Classification results of the Sentinel-2 image.

4 Discussion

4.1 Quality and impacts of the SIM indices

With the use of the indices and thresholds, it was possible to remove most of the unwanted pixels and identify pixels containing spectral information of SIMs (Figure 36). In the first step, the dark pixels were well removed. The vegetation index (1) removed the vegetation pixels from the image very reliably, based on the clear spectral distinction from the other mineral samples.

Based on the ferric iron index (2), the second threshold masked many non-SIMs almost completely, including *Chrysocolla*, *Cuprite*, *Malachite* and *Pyrite*. This was to be expected since these minerals do not contain iron except for *Pyrite*. *Pyrite*, on the other hand, consists of about 50 % iron, but is not particularly active in the VNIR and SWIR wavelength region showing little to no absorption features. Therefore, the iron index calculated low pixel values, and consequently *Pyrite* was removed. *Magnetite* and *Chalcopyrite* pixels were reduced, *Bornite* was mostly still present after applying this index. However, this index also removed many pixels from the *Copiapite* mineral. The pixels of the other SIMs were mostly preserved. But, as this is an important filter for distinguishing the other four SIMs from the other minerals in the dataset, copiapite was removed as a class of further analysis.

The band ratio (3) in the third threshold removed the minerals *Chalcopyrite* completely and *Bornite* mostly. Only a few pixels of *Magnetite* remained. This is due to the fact that *Chalcopyrite* and *Bornite* do not show a prominent iron feature, which could have been recognized by this band ratio. *Magnetite*, on the other hand got a prominent iron feature, so more pixels from this mineral were not removed any further with the third mask.

In summary, the used indices were able to distinguish SIMs from other minerals. However, a few pixels of other minerals are still present, namely magnetite as non-SIM and copiapite as SIM which is not classified as a separate class. This has to be taken into account in an analysis.

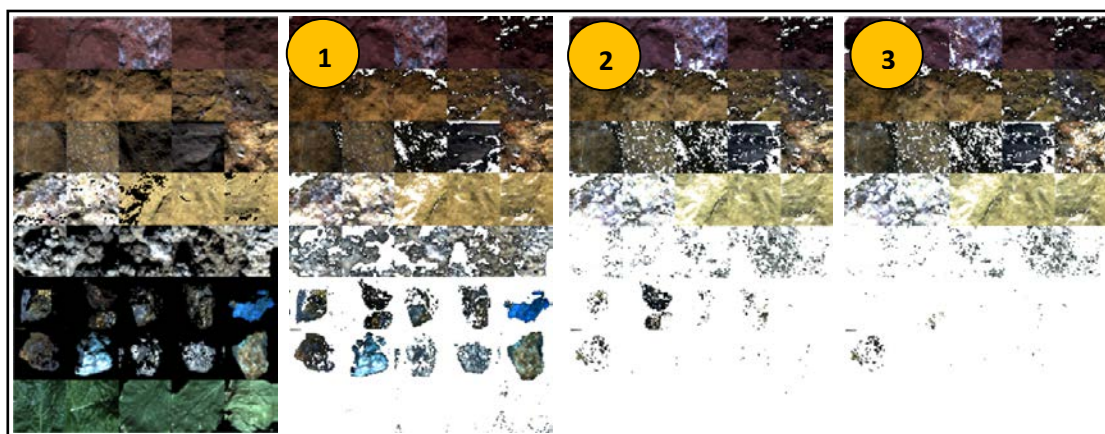


Figure 36 From left to right: original data set, data set after vegetation and dark pixel masking (1), Ferric Iron masking (2) and Iron Feature Band Ratio (IFBR) (3) applied.

4.1 Classification of the Laboratory Field Sample Validation Mosaic

The samples are explored from two different data type sites. One is the spectral information and the other one the mineral phases mapped by XRD-analysis. The XRD analysis available for the samples in dataset 2 showed the differences of mineralogy in the various samples of the validation mosaic. There were some samples where only one mineral phase of SIMs was detected, such as AM2 and KM-w7, or where one mineral phase strongly dominated, such as AM4, AM5 and L-s4. Sample KM-w2 in turn consisted of approximately half of two different SIM phases. It is not possible to draw direct conclusions from these information between the two kinds of data. But a sample with 99 % Jarosite measured by XRD and a classified sample with the majority of pixels classified as Jarosite (e.g., sample AM4) exists, it can be assumed that this corresponds and verifies each other very well. Comparing a hard classifier, namely a RF-Classifer (RFC), with XRD makes it difficult to use a classical accuracy assignment. Unmixing could be considered here to counteract this difficult. The problem is how the reference classes should be determined which is normally binary structured (class vs. not class). Should the reference class be defined as the highest percentage outcome of the XRD, even if they are not significantly different (e.g., sample KM-w2), or should all measured values form the possible reference class? Even an approach of different thresholds with multiple results of 1%, 5% or 10% would show high differences in determining accuracy values. Therefore, a qualitative evaluation of the classification results in relation to the results of the XRD analysis is the best option to explore the results so far. The classifications of the samples were described briefly in the results section. The findings are summarised and discussed in the following.

Hematite seems to be classified even at low occurrences (sample AM1 and AM5), as well as overlapping spectral information of other SIMs. This became clear with Jarosite in sample KM-w2, where mostly Hematite was classified. Furthermore, misclassifications of varying degrees seemed to occur with this mineral in particular (sample L-s4, L-w2, L-s3 and AM4). This needs to be considered for further use. False detection has the greatest negative effect when hematite overlays Jarosite without being recognised. This had to be kept in mind for the analysis results of field data application.

Large amounts of Goethite, according to XRD analysis, were mostly well recognised and classified as Goethite/ Limonite within the RFC (sample L-w2, L-s4 and L-s3). In some cases, however, this spectral signal was overlaid/displaced by small amounts of Jarosite in the material (according to XRD analysis) (sample AM1 and AM4). This was a similar behaviour as it was also the case with Hematite.

In general, the classification of the datasets 2 showed that the homogeneity of the material and the detection of an XRD result predominantly belonging to one mineral played decisive roles for the classification. It also showed possible inaccurate classification results that occur with material mixes

4 Discussion

4.1 Classification of the Laboratory Field Sample Validation Mosaic

with multiple SIMs. Areas covered by shadows and dark pixels in general tended to be often falsely classified.

4 Discussion

4.2 Classification results of the Skouriotissa mining area

4.2 Classification results of the Skouriotissa mining area

The next two sections deal with discussion of the classification results for the Skouriotissa and Apliki mines in detail. Figure 37 shows the results of the two satellite-datasets in comparison. The pit areas are relatively small in comparison to the waste dumps in the mining area. These areas contain the most classified pixels. In the following, the three pits and the waste dumps in the mine are discussed in detail. The color-coding here distinguishes between high-confidence predictions (bold colours) and low confidence predictions (light colours) which is the same colour-scheme as presented before for the different minerals.

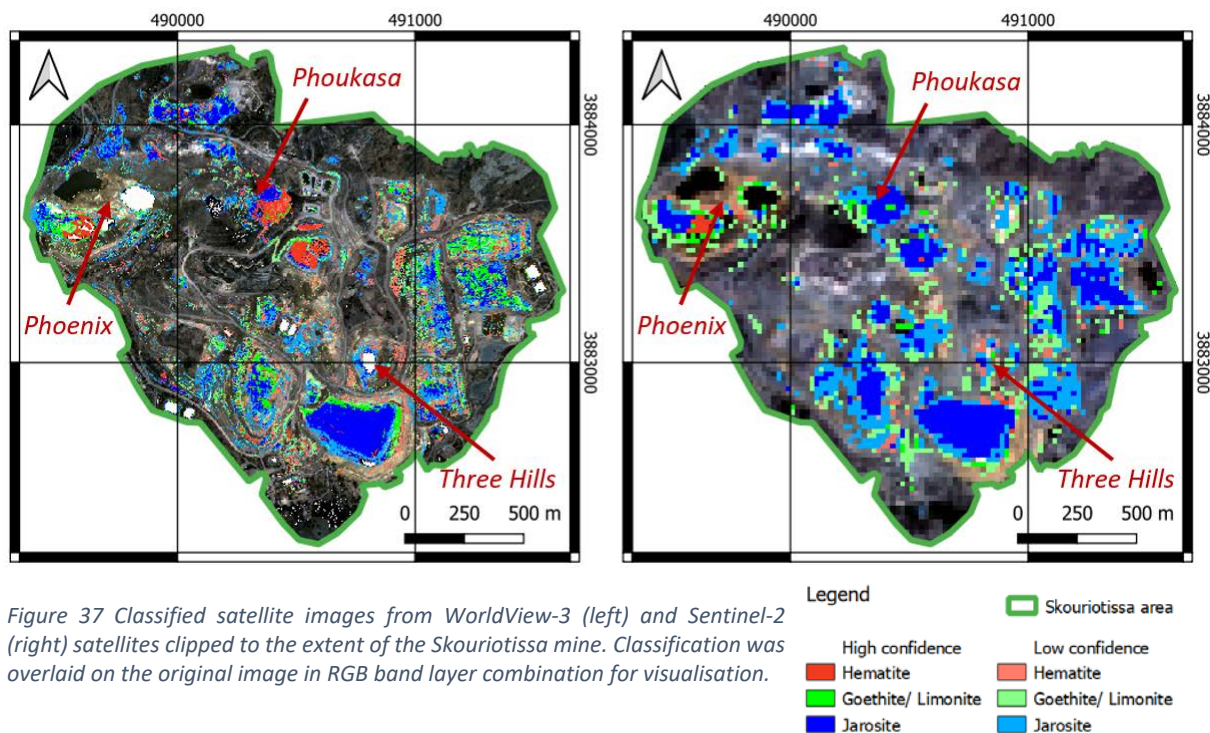


Figure 37 Classified satellite images from WorldView-3 (left) and Sentinel-2 (right) satellites clipped to the extent of the Skouriotissa mine. Classification was overlaid on the original image in RGB band layer combination for visualisation.

4.2.1 Phoenix

The Phoenix pit is the lowest point of the mine (Figure 54). There are three water bodies in the Phoenix pit, only one got classified pixels. In this area all three classes were represented. At WorldView-3, Jarosite, Goethite/ Limonite and Hematite were classified from west to east. Sentinel-2 had Jarosite in the west and Hematite in the east. Goethite/ Limonite was more distributed around this area. There is a lot of material mixed with water in this area and spatially the conditions change quickly here.

4.2.2 Phoukasa

The Phoukasa pit stretched from west to east, increasing in height, means that this area reflected a slope. At the lowest point there was also a water body, masked out in the pre-processing (WorldView-3) or had very low spectral reflectance (Sentinel-2). With increasing altitude, Jarosite and some

4 Discussion

4.2 Classification results of the Skouriotissa mining area

Hematite (low confidence) were classified on as mining terraces recognisable areas. Further above was a quarry site identified as Jarosite in the lower part and hematite in the upper part (high confidence).

4.2.3 Three Hills

On the WorldView-3 images, due to the higher resolution, it is visible that mainly the western wall of the pit was classified (mainly Jarosite). In the Sentinel-2 image this appears much more blurred, due to the lower resolution. It is also not possible to clearly identify the water body because of its size (Sentinel-2). In contrast, for the worldView-3 image these pixels were already masked out during the pre-processing.

4.2.4 Mine dumps

Apart from the three pits, most other areas in the mine are waste dumps, according to Naden et al. (2006). They showed significantly more classified pixels than the actual mining pits, but the areas are also much bigger (Figure 37, Figure 38).

In the north-western part, there is an area that was classified very similarly in both satellite images. In the centre was a large area of Jarosite (high confidence) classified, around this also Jarosite as well as Hematite (with low confidence). More western from this, two areas have also been classified as Jarosite.

Towards the centre of the image, at a higher altitude (DEM can be found in Figure 54), is an area that was largely identified as Hematite (high confidence) in the WorldView-3 image and mainly as Jarosite (low and high confidence) in the Sentinel-2 image. This is the classification result that differ the most between the two images regarding the size of adjoining pixels with different class assignment. The reason for this cannot yet be definitively explained. It may be due to the internal differences of the RF models, but also to the different resolution of the two sensors. With smaller pixels, WorldView-3 could be able to recognise Hematite, which can only be recognised as Jarosite over a large area with Sentinel-2 due to larger pixels with a mixed spectrum.

In the southwest of the image was a large area of classified mine waste (Figure 37). All three SIM classes were detected (WorldView-3), whereby Sentinel-2 had primarily Jarosite detected. Jarosite was mainly found centrally and at the highest points (Figure 54). To the east from this location, in the south of the mine, lays a kind of elevated basin (Figure 38, bottom right image), which was the largest in comparison to the other definable areas of the mine. It is not known what this elevated basin was used for. Both sensors classified Jarosite here with high confidence. At the edges there was Goethite/ Limonite and above that some Hematite classified.

4 Discussion

4.2 Classification results of the Skouriotissa mining area

To the east of the mine are areas that can be roughly be divided into 4 zones. After a visual inspection of this area, they could have been identified as an area for storage and processing of mining material.

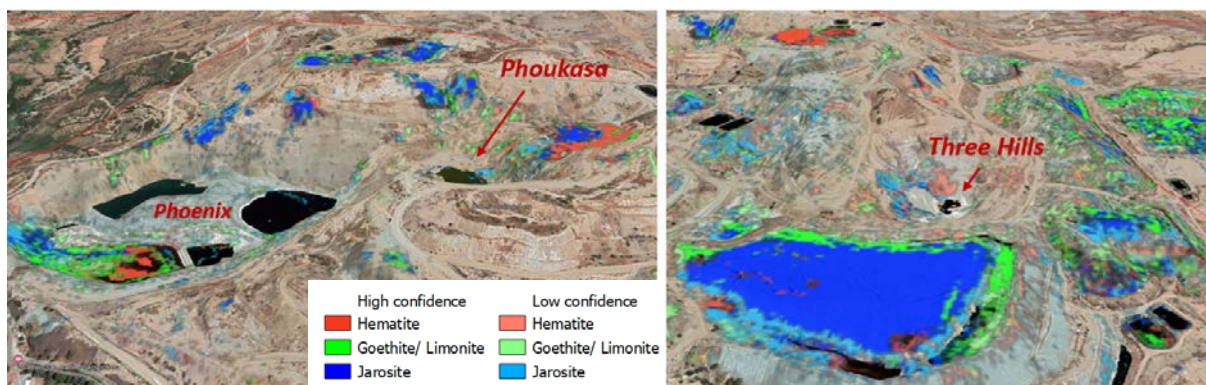


Figure 38 Visualization of the classification result of the WorldView-3 data overlaid on Google Earth RGB image from July 2019 with elevation display in Google Earth Pro (version 7.3.4.8573 (64-bit)).

Consultation with the local mining company was not possible to this time due to lack of proper communication. The Sentinel-2 image found mainly Jarosite in these areas (high and low confidence). WorldView-3 managed to differentiate spatially even further. Smaller contiguous areas of all three SIM classes were found (Figure 37).

4.2.5 Field data from the Skouriotissa mine

In 2011, five sample points (Figure 39) within the Skouriotissa mine were surveyed with XRD for the *Geochemical atlas of Cyprus* (Cohen and Rutherford, 2011). Various minerals were recorded, including Jarosite. But this is the only SIM of the XRD analysis taken by the measurement. This makes the evaluation difficult compared to the three mineral phase classes used in this work. In addition, it becomes clear that conditions in the mine have already changed over short time intervals (see Outlook, page 66). The XRD data is from 2011 and the analysis of this work with data from 2019. Position 5 (Table 14) with 0% is not applicable and positions 3 and 4 with low values are not very significant. No SIMs were mapped at position 2, which could well be due to the time interval.

At position 5 28.3% Jarosite were measured (Table 14). The classification also shows clear Jarosite pixels with high and low confidence in this region (Figure 37, Figure 39).

4 Discussion

4.2 Classification results of the Skouriotissa mining area

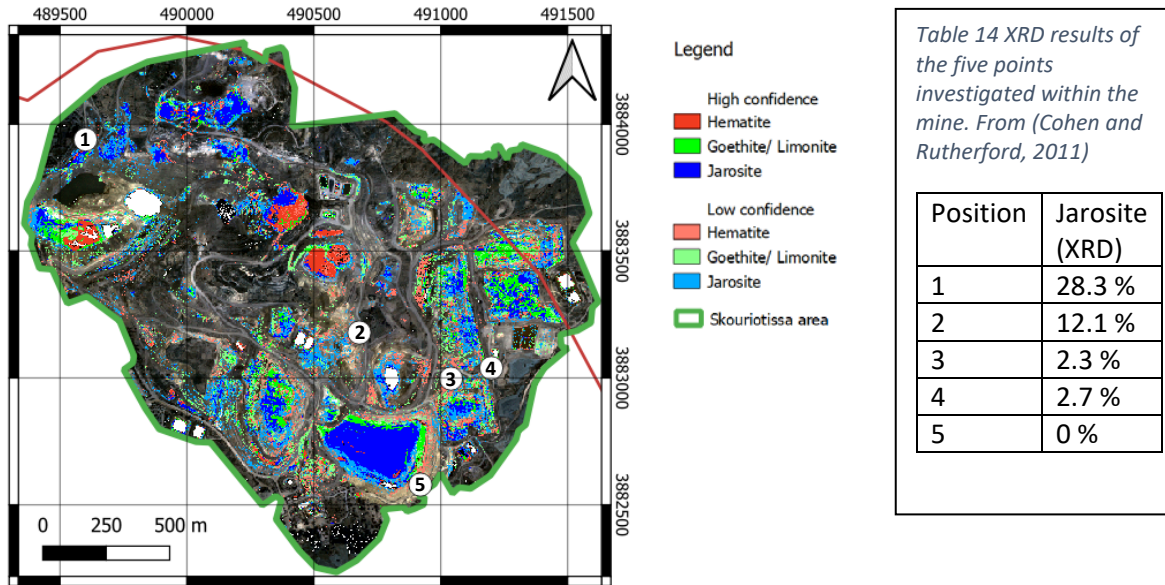


Figure 39 Location of the XRD measurements within the mine. From (Cohen and Rutherford, 2011)

4 Discussion

4.3 Classification results of the Apliki mining area

4.3 Classification results of the Apliki mining area

The indices detected approximately the same area as potentially SIMs in the satellite images of both sensors. The water body at the deepest point in this mine (Figure 40) is masked in WorldView-3 due to dark pixels and is not classified in Sentinel-2. The exploitation terraces around this water body were also only classified partly. Pixel size does not seem to be the reason as this occurred for both satellite datasets. These areas are highly vegetated, which cover the surface and therefore change the spectral signal. Sharper slopes, which are unvegetated are also not classified. This could be due to difficulties in nadir view from the sensor as well as the possibility of the material to get carried away because of the slope.

The largest areas were classified to the north of the mine and are located partly in the UN buffer zone which makes on-site investigation and interpretation of the results complicated. In general, this result makes it clear that most of the extracted material was deposited North of the open pit and SIMs formed predominantly in this mine dump area. As also for Skouriotissa, WorldView-3 detected more Hematite pixels in Apliki. It could be assumed, that due to a higher spatial resolution the sensor was able to do so. However, it cannot be guaranteed that this can partly be attributed to differences in the RF-model.

Regarding the surface elevation these areas are very low compared to the rest of the mine (Figure 55). This supports the assumption that secondarily formed material accumulates in shallower areas.

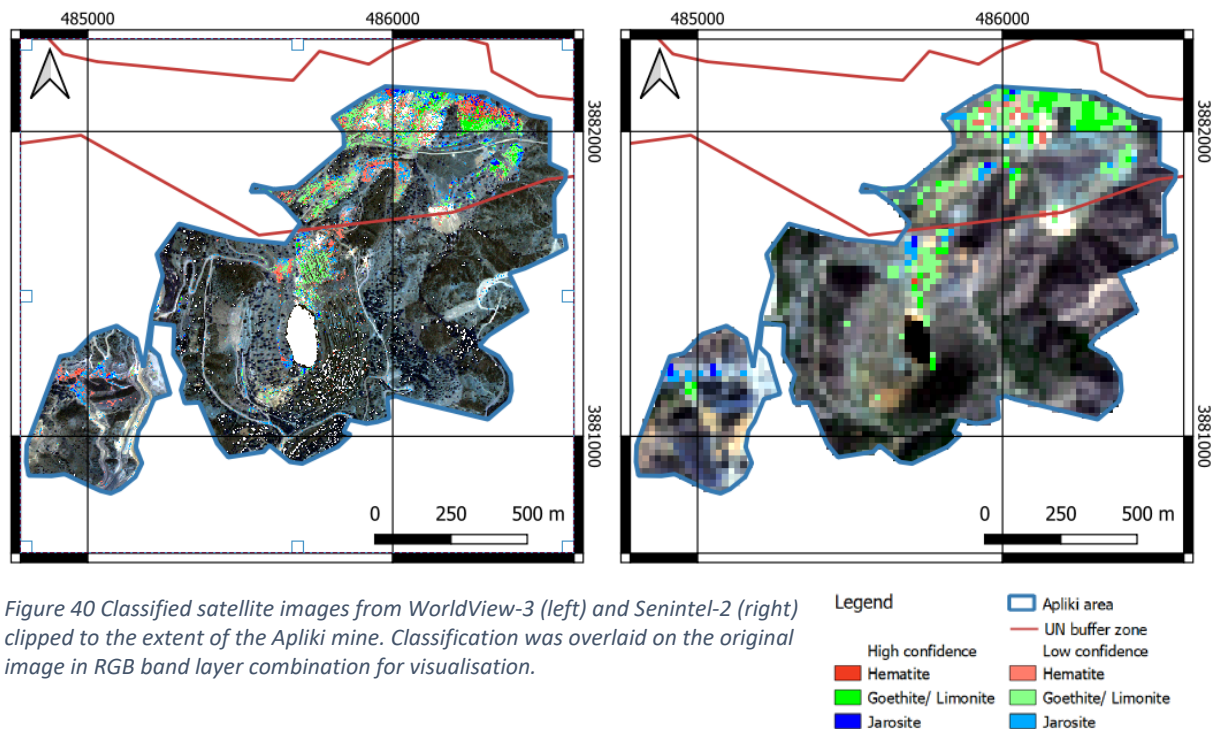


Figure 40 Classified satellite images from WorldView-3 (left) and Sentinel-2 (right) clipped to the extent of the Apliki mine. Classification was overlaid on the original image in RGB band layer combination for visualisation.

4.4 Challenges and Implications

Table 15 lists and discusses some challenges and implications regarding the outcomes of this work as well as general problems involved in the work with spectral data.

Table 15 List of Challenges and Implications regarding this work

#	Challenge	Implication
1	Cost and availability of data	Many different spectral products are available. These differ in spatial, temporal and spectral resolution, sometimes significantly. Depending on the mission and sensor, this data is available free of charge or must be purchased. The comparison in this paper with two different satellites is an example of these differences. On the one hand, Sentinel-2 data exhibits lower spatial and spectral resolution (20m pixels, 9 bands in VNIR-SWIR), but has a high temporal resolution and is freely available. On the other hand, the commercial WorldView-3 data is available with much higher spatial resolution (1 - 3 m) and higher spectral resolution (16 bands in VNIR-SWIR).
2	Pixel size and mixed pixels	The pixel size is largely dependent on the satellite/sensor used. This also has an influence on mapping results, as discussed in this paper. With higher spatial resolution WorldView-3 satellite, more hematite minerals can be detected, which is also due to the pixel size. Mixed pixels always occur. Since the method presented here does not unmix the endmembers, mixed pixels are inevitably classified. This cannot be avoided, especially when rock/surfaces with mineral mixtures are present. Therefore, this has to be considered in an analysis. In Dataset 2, spectral overlays of individual mineral classes were therefore discussed.
3	Linkage of spectral and geochemical analysis	In this work, the spectral information was evaluated based on geochemical information of XRD analysis of one sample set. The problem emerged that spectrally a correlation of the mineral phases goethite and limonite took place. Since limonite is not a pure mineral phase, this mineral is not distinguishable in the XRD analysis. This made the linking of the two types of data more difficult, especially with regard to the interpretation of the results. Also, a reduction of minerals/ mineral groups, in this case to three SIMs, can lead to difficulties in the evaluation. This is because XRD is not limited to pre-selective class selection. It must be expected that classes excluded for spectral reasons may reappear in XRD Results.
4	Properties of the material	<u>Colour</u> In the VNIR, the colour of the material has spectral influences. Different colours can be found in the laboratory data, e.g., the hematite samples are more reddish, the goethite samples more yellowish and the jarosite samples more whitish. To a certain extent, this can influence the spectral signature. Still, colours and spectra belong closely together, and are part of a spectral signature. Care should be taken to ensure that the classifier does not use these features to distinguish spectrally between classes. However, this does not necessarily apply to the surfaces in the field. This laboratory bias can

		<p>possibly be improved by using more samples with different colours, so that this has an influence on the RF model.</p> <p><u>Texture</u></p> <p>The texture and grain size of the material can have an influence on the spectral resonance, e.g. the absorption feature depth. Including samples with different textures and grain sizes in the sample selection could incorporate this into the RF model.</p>
5	Size of the investigated area	<p>For representative results, the size of the study area plays a considerable role. In this paper, this becomes clear when comparing the smaller Apliki mine with the larger Skouriotissa mine. It is clear that a large mine provides significantly more information. Thus, the smaller the mine, the fewer pixels cover the area and the fewer pixels remain in a classification. As a result, it can happen that for areas that are smaller than a certain threshold, no or very little information can be obtained about an investigated area. This problem is further increased if the spatial resolution of the satellite data that is available is low.</p>
6	Geological and spectral expert knowledge input	<p>The approach presented here provides the possibility to use multispectral satellite data to generate predictions on the distribution of occurring SIMs. With the approach applied here, no site-specific spectral library is prepared, which would have to be checked for spectral suitability of the data and inputs for the classification on the basis of geological expertise (Koerting, 2021b). However, the classification of the site should always be accompanied by on-site investigations. This scope depends on the outcome of the classification. Therefore, this should again be based on expert knowledge. Also, possible biases and misclassifications, such as in predictions being in favour of the hematite class in dataset 2, need to be evaluated with expert knowledge and taken into account later when applied to the field data.</p>
7	Water vapour bands	<p>A general problem is that there is a water vapour band located around 940nm. This feature caused by water overlaps a large wavelength range with the prominent iron feature. In laboratory data this may be an insignificant factor, but the influence is stronger in field images because of more atmosphere between sensor and surface. Distinguishing hematite from goethite, for example, is made more difficult because the nanometer shift is in this range. WorldView-3 has no spectral band in this range and with Sentinel-2 this is excluded in the band selection. This reduces the influence.</p>

4.5 The use of different wavelength ranges: VNIR vs. SWIR

The analysis and work with both satellites (WorldView-3 and Sentinel-2) has clearly shown which wavelength ranges are important for the analysis using RF-models demonstrated here. If it is then considered that the selection of the most important bands for the RF-models (based on the MDG index, Table 11, page 38), with the exception of band 11 and 12 for WorldView-3 (1661 nm and 1730 nm) and band 8 for Sentinel-2 (1139 nm), these consist only of bands in the VNIR wavelength range. Of the five indices used here, those that require values from the SWIR, namely *ferrous iron*, *ferric oxides* and *ferrous silicates*, would be no longer possible to include. But these proved to be important layers in distinguishing the classes of the RF-analysis (see Table 11, page 38).

However, it can be assumed that a solid RF-model is also achievable with the remaining 8 VNIR bands and that it is possible to obtain comparable classification and monitoring results. Especially when considering that the Jarosite typical feature in the SWIR range showed almost no influence for mineral identification in the application shown here. The ferric iron, NDVI and IFBR indices can still be used with VNIR information and are applicable for the masking methods. Considering the spatial resolution, the restriction to the VNIR has no effect on Sentinel-2. However, it affects the WorldView-3 sensor in various ways. Data would be cheaper to order on demand, more often than note archive data is available for time series and the resolution could improve from 3 x 3 m to 1.7 x 1.7 m comparable to the WV3-SWIR data. The feasibility, though, would have to be checked before an application.

Over the course of this thesis, it became apparent that a reduction of the classes was necessary. It should be kept in mind that an improvement of the method, e.g., by an improved and larger sample selection, would bring further approaches. Although Hematite, Goethite and Jarosite are the main representatives and most abundant in this environment, a broader range of acidity indications can be obtained by looking at other SIMs. For example, Copiapite, which can indicate a very strongly acidic pH value of less than 1.5. Of additional interest is Schwertmannite, which like Jarosite is a Fe-hydroxysulphate. Schwertmannite has similar pH-value aggregation as Jarosite (2.8 vs. 2.3) but can also indicate higher pH-values up to 6.5.

4.6 The use of data from different dates (WorldView-3)

As already described in the method section, the WorldView-3 data set was produced synthetically. It was not possible to record VNIR and SWIR data at the same time, as the VNIR data was taken from the archive and the SWIR data was taken after a new recording order. The investigation of the mines has shown how fast local conditions can change. The question arises what the impact of using SWIR data

4 Discussion

4.6 The use of data from different dates (WorldView-3)

from 2019 and VNIR data from 2020 was. Figure 41 shows a comparison of the two satellite images in a RGB representation.

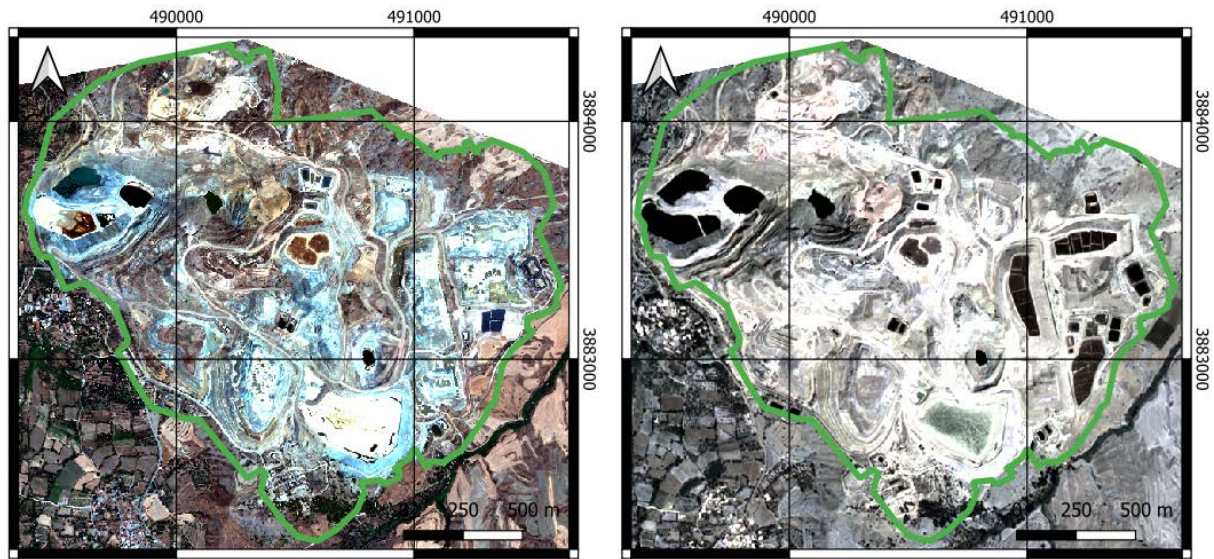


Figure 41 Left: VNIR dataset from 2019, Right: SWIR dataset from 2020

The influence is mainly depended on how much data is used/ mixed from the two different dates for the RF-model. By reducing the bands according to their importance for differentiation (MDG index), only one band remained from the SWIR dataset (band 12). This means that data from the SWIR image had very little influence on the contents of the RF-model in comparison to the VNIR data. In addition, it is also the band with the least influence according to MDG index. Nevertheless, it can be assumed that, in general, combining this information will weaken the analysis. Therefore, it is recommended to shorten the time between dates when combining data from different dates. More preferable is the option to only use one of the two satellite data sets (VNIR or SWIR).

5 Conclusion

This work proposed an application-based method for monitoring mining areas and waste tailings. This was achieved by detecting areas where potentially SIMs have formed and are currently aggregated. These mapping results are presented pixel-based as classification maps. Based on the strength of the indices used, the confidence of these pixels can also be estimated. Furthermore, a differentiation into different SIMs is possible, as well as the representation of the "certainty" of the assignment in the RF-model to assess possible pH-value conditions.

The distinction between specific SIMs offers conclusions about the acidity of the material and can be used as an indicator for the occurrence of AMD. Furthermore, based on the detected pixels, an estimation of the size of these areas is possible. However, this can only be an estimation, as the detected pixels depend strongly on the intensity of the applied indices.

Altogether, this work demonstrates an interesting and promising approach to the development of a method for monitoring mines and tailings surfaces. The method developed in this work is not sensor-specific and can therefore be applied widely if similar spectral bands are available.

In the comparison of the publicly available 9-channel sensor (Sentinel-2) and the commercial 16-channel sensor (WorldView-3) with higher-resolution both showed good and comparable performances in the laboratory analysis. In the field, the WorldView-3 sensor has a clear spatial resolution advantage. However, due to the open and free availability of the Sentinel-2 data, an easy and fast monitoring and classification over several years is possible (see Outlook, page 66). Therefore, a combination of both methods could be most applicable. Sentinel-2 data first and then examine particularly potentially polluted hotspots more closely with WorldView-3 data. Consequently, an application proposal can be implemented as following:

Periodic monitoring of mines is carried out using freely available and high temporal resolution Sentinel-2 data. This monitoring consists of mineral classification, change analysis and area estimation. If results indicate changes or areas with uncertain results, an analysis with high-resolution WorldView-3 data and field measurements is recommended.

In addition to multispectral satellites, other data acquisition systems will also be able to make progress in monitoring in the future. Hyperspectral satellites are on the rise and will also be able to provide free data with the EnMAP and PRISMA satellite, for example. Expectations for these data are better mineral

5 Conclusion

4.6 The use of data from different dates (WorldView-3)

discrimination based on smaller visible wavelength shifts and other possible detection methods such as the EnGeoMAP mineral characterisation algorithm (Boesche et al., 2016; Mielke et al., 2016; Rogaß et al., 2013). More local applications can already be captured at high spatial resolution with UAV overflights. Numerous data bases and methods are therefore available for monitoring waste tailings.

6 Outlook

6.1 Application on Sentinel Time series

The Sentinel-2 sensor convinces for its use in time series analysis. The cost-free availability of the satellite images and the high temporal resolution allow observations of change on an annual, monthly or even five days basis, if the cloud coverage is low.

The time series (Figure 42) shows very clearly how Jarosite forms/ accumulates over time in the large "basin" in the south of the mine. It begins with a classification of low confidence Jarosite pixels which change over time to a high confidence.

In the southern water body of the Phoenix Pit, barely any pixels were classified centrally in 2021 compared to 2019. If we follow this up, it is noticeable that a NDVI is calculated here (Figure 57, page 84). Therefore, it can be assumed that vegetation is growing on the contaminated areas here. In the eastern part of the image, the number of classified pixels is also reduced, and mainly low confidence pixels are present.

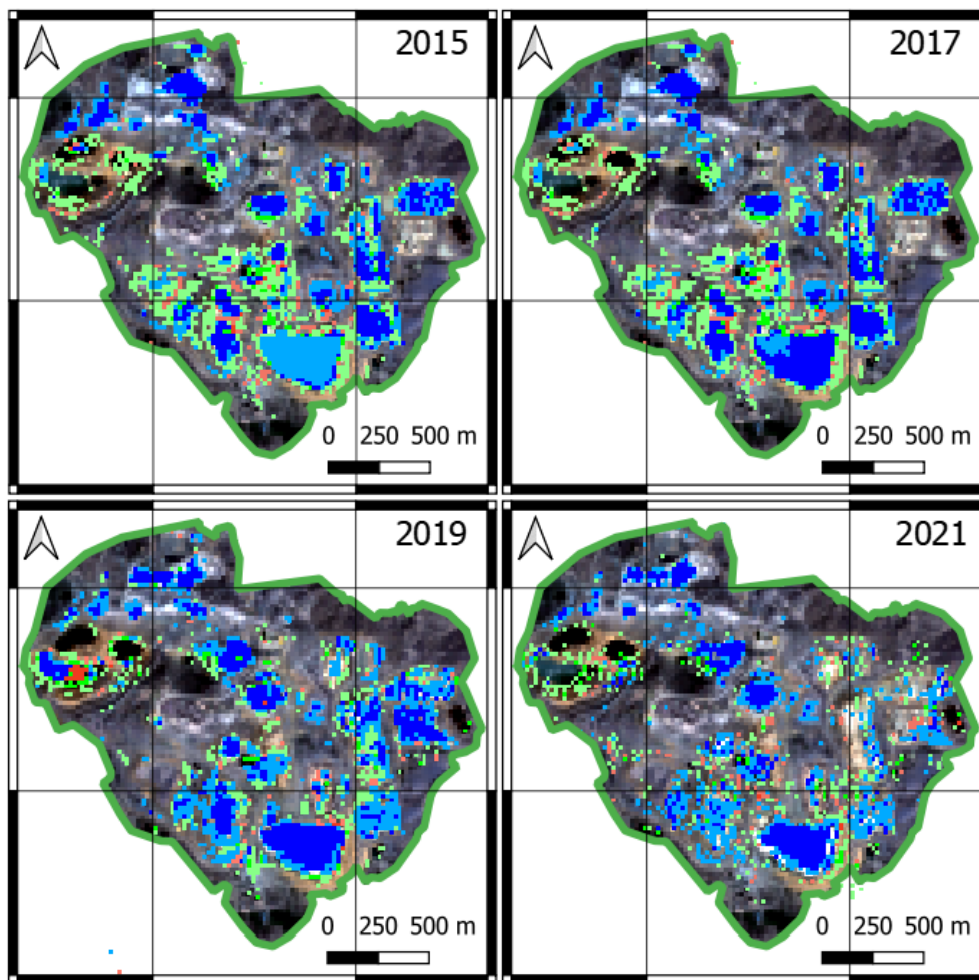


Figure 42 Time series analysis of Sentinel-2 images (in a 2-year sequence) of the years 2015, 2017, 2019 and 2021. The same classification method was applied as for the previous Sentinel-2 datasets of this work.

7 Literature

- Aasen, H., Bendig, J., Bolten, A., Bennertz, S., Willkomm, M., Bareth, G., 2014. Introduction and preliminary results of a calibration for full-frame hyperspectral cameras to monitor agricultural crops with UAVs. *Int. Arch. Photogramm. Remote Sens. Spat. Inf. Sci. - ISPRS Arch.* 40, 1–8. <https://doi.org/10.5194/isprsarchives-XL-7-1-2014>
- Adamides, N.G., 2010a. 2Mafic-dominated volcanogenic sulphide deposits in the troodos ophiolite, Cyprus Part 2 - A review of genetic models and guides for exploration. *Trans. Institutions Min. Metall. Sect. B Appl. Earth Sci.* 119, 193–204. <https://doi.org/10.1179/1743275811Y.0000000011>
- Adamides, N.G., 2010b. 1Mafic-dominated volcanogenic sulphide deposits in the troodos ophiolite, Cyprus part 1-the deposits of the Solea graben. *Trans. Institutions Min. Metall. Sect. B Appl. Earth Sci.* 119, 65–77. <https://doi.org/10.1179/1743275811Y.0000000001>
- Antivachis, N.D., 2015. The geology of the northern part of the apliki Cyprus-type ore deposit. *Bull. Geol. Soc. Greece* 49, 4. <https://doi.org/10.12681/bgsg.11047>
- Bade, M., 2016. Hyperspektrale Fernerkundung zur Prospektion von Lithiumglimmern in Tørdal, Norwegen. Masterarbeit, Universität Potsdam.
- BBC news, 2021. Vale dam disaster: \$7bn compensation for disaster victims.
- Bishop, J.L., Murad, E., 2005. The visible and infrared spectral properties of jarosite and alunite. *Am. Mineral.* 90, 1100–1107. <https://doi.org/10.2138/am.2005.1700>
- Blahwar, B., Srivastav, S.K., de Smeth, J.B., 2012. Use of high-resolution satellite imagery for investigating acid mine drainage from artisanal coal mining in North-Eastern India. *Geocarto Int.* 27, 231–247. <https://doi.org/10.1080/10106049.2011.628761>
- Blume, H.-P., Brümmer, G.W., Horn, R., Kandeler, E., Kögel-Knabner, I., Kretzschmar, R., Stahr, K., Wilke, B.-M., 2010. Scheffer/Schachtschabel: Lehrbuch der Bodenkunde, Scheffer/Schachtschabel: Lehrbuch der Bodenkunde. <https://doi.org/10.1007/978-3-662-49960-3>
- Boesche, N., Mielke, C., Rogass, C., 2016. EnGeoMAP Manual for Application : EnGeoMAP (1 . 0).
- Borsdorf, R., 1996. Moderne methoden in der spektroskopie. *Zeitschrift für Phys. Chemie Vol.* 194, 131–131.
- Breiman, L., 2001. Random forests, in: *Machine Learning*. pp. 5–32. <https://doi.org/10.1023/A:1010933404324>
- Breiman, L., 1996. Out-of-Bag Estimation. *N. Z. Med. J.* 128, 97–100.
- Byrne, P., Wood, P.J., Reid, I., 2012. The impairment of river systems by metal mine contamination: A review including remediation options. *Crit. Rev. Environ. Sci. Technol.* 42, 2017–2077. <https://doi.org/10.1080/10643389.2011.574103>
- Charalambos, P., 2016a. A Digital Elevation Model for Cyprus based on the Advanced Land Observing Satellite World 3D Topographic Data (ALOS 2 W3D30) Digital Surface Model.
- Charalambos, P., 2016b. A Digital Elevation Model for Cyprus based on the Advanced Land Observing Satellite World 3D Topographic Data (ALOS 2 W3D30) Digital Surface Model.
- Clark, R., Swayze, G., Livo, K.E., Kokaly, R.F., Sutley, S.J., Dalton, J.B., McDougal, R.R., Gent, C.A., 2003. Imaging spectroscopy: Earth and planetary remote sensing with the USGS Tetracorder and

- expert systems. *J. Geophys. Res. Planets.* <https://doi.org/10.1029/2002je001847>
- Clark, R.N., 1999a. Spectroscopy of rocks and minerals, and principles of spectroscopy, in: *Remote Sensing for the Earth Sciences: Manual of Remote Sensing.* <https://doi.org/10.1111/j.1945-5100.2004.tb00079.x>
- Clark, R.N., 1999b. Spectroscopy of rocks and minerals, and principles of spectroscopy, in: Rencz, A.N. (Ed.), *Manual of Remote Sensing, Remote Sensing for the Earth Sciences.* John Wiley and Sons, New York, pp. 3–58. <https://doi.org/10.1111/j.1945-5100.2004.tb00079.x>
- Cohen, D., Rutherford, N., 2011. Technical Report on the Development of a Geochemical Atlas of Cyprus. Volume 1 – Text.
- Crowley, J.K., Williams, D.E., Hammarstrom, J.M., Piatak, N., Chou, I.M., Mars, J.C., 2003. Spectral reflectance properties (0.4–2.5 μm) of secondary Fe-oxide, Fe-hydroxide, and Fe-sulphate-hydrate minerals associated with sulphide-bearing mine wastes. *Geochemistry Explor. Environ. Anal.* 3, 219–228. <https://doi.org/10.1144/1467-7873/03-001>
- Cudahy, T., 2016. Mineral Mapping for Exploration: An Australian Journey of Evolving Spectral Sensing Technologies and Industry Collaboration. *Geosciences* 6, 52. <https://doi.org/10.3390/geosciences6040052>
- Dalm, M., Buxton, M.W.N., van Ruitenbeek, F.J.A., 2017. Discriminating ore and waste in a porphyry copper deposit using short-wavelength infrared (SWIR) hyperspectral imagery. *Miner. Eng.* 105, 10–18. <https://doi.org/10.1016/j.mineng.2016.12.013>
- Dalm, M., Buxton, M.W.N., Van Ruitenbeek, F.J.A., Voncken, J.H.L., 2014. Application of near-infrared spectroscopy to sensor based sorting of a porphyry copper ore. *Miner. Eng.* 58, 7–16. <https://doi.org/10.1016/j.mineng.2013.12.016>
- Dennison, P.E., Halligan, K.Q., Roberts, D.A., 2004. A comparison of error metrics and constraints for multiple endmember spectral mixture analysis and spectral angle mapper. *Remote Sens. Environ.* 93, 359–367. <https://doi.org/10.1016/j.rse.2004.07.013>
- Elements.visualcapitalist.com/, 2022. Elements Visual Capitalist. Available at: <https://elements.visualcapitalist.com/visualizing-the-size-of-mine-tailings/> (Accessed: May 3, 2022).
- Ernst & Young Global Limited, 2018. EY top 10 business risks facing mining and metals in 2019 - 20. © 2018 EYGM Limited., EYG no. 012357-18Gbl. Available at: ey.com/miningmetals.
- ESA, 2022. <https://sentinels.copernicus.eu/web/sentinel/technical-guides/sentinel-2-msi/msi-instrument>. <https://doi.org/10.1111/j.1945-5100.2004.tb00079.x> Available at: <https://sentinels.copernicus.eu/web/sentinel/technical-guides/sentinel-2-msi/msi-instrument> (Accessed: May 10, 2022)
- Flores, H., Lorenz, S., Jackisch, R., Tusa, L., Cecilia Contreras, I., Zimmermann, R., Gloaguen, R., 2021. Uas-based hyperspectral environmental monitoring of acid mine drainage affected waters. *Minerals* 11, 1–25. <https://doi.org/10.3390/min11020182>
- Fonseca, R.O.C., Kirchenbaur, M., Ballhaus, C., Munker, C., Zirner, A., Gerdes, A., Heuser, A., Botcharnikov, R., Lenting, C., 2017. Fingerprinting fluid sources in Troodos ophiolite complex orbicular glasses using high spatial resolution isotope and trace element geochemistry. *Geochim. Cosmochim. Acta* 200, 145–166. <https://doi.org/10.1016/j.gca.2016.12.012>
- Gibson, R., Danaher, T., Hehir, W., Collins, L., 2020. A remote sensing approach to mapping fire severity in south-eastern Australia using sentinel 2 and random forest. *Remote Sens. Environ.* 240, 111702. <https://doi.org/10.1016/j.rse.2020.111702>

- Global Tailings Review, 2020. Global Tailings Review Consultation on the Draft Global Tailings Standard 5 August 2020.
- Gupta, R.P., 2003. Remote sensing geology. Springer Science & Business Media, Vol. 2.
- Hadjipanagiotou, C., Christou, A., Zissimos, A.M., Chatzitheodoridis, E., Varnavas, S.P., 2020. Contamination of stream waters, sediments, and agricultural soil in the surroundings of an abandoned copper mine by potentially toxic elements and associated environmental and potential human health-derived risks: a case study from Agrokipia, Cyprus. *Environ. Sci. Pollut. Res.* 27, 41279–41298. <https://doi.org/10.1007/s11356-020-10098-3>
- Herrmann, E., Jackisch, R., Lorenz, S., Zimmermann, R., Dr. Gloaguen, R., Günther, L., 2018. Machbarkeitsstudie zur Nutzung multi- und hyperspektraler Verfahren für Kippenzustandsbeschreibung und Tagebaurestseemonitoring Abschlussbericht zum TP 2.7 85.
- Herrmann, S., 2019. Capacity of Imaging Spectroscopy for the characterisation of REO , REE bearing minerals & primary REE-deposits. <https://doi.org/http://doi.org/10.2312/GFZ.b103-19089>
- Herrmann, S., 2015. Capacity of imaging spectroscopy for the characterisation of reo, ree bearing minerals & primary ree-deposits.
- Hong Han, Xiaoling Guo, Hua Yu, 2016. Variable selection using Mean Decrease Accuracy and Mean Decrease Gini based on Random Forest, in: 2016 7th IEEE International Conference on Software Engineering and Service Science (ICSESS). IEEE, pp. 219–224. <https://doi.org/10.1109/ICSESS.2016.7883053>
- Humphreys, D., 2020. Mining productivity and the fourth industrial revolution. *Miner. Econ.* 33, 115–125. <https://doi.org/10.1007/s13563-019-00172-9>
- Hunt, G.R., 1989. Spectroscopic Properties of Rocks and Minerals, in: Carmichael, R.S. (Ed.), *Practical Handbook of Physical Properties of Rocks and Minerals*. CRC Press, pp. 599–669.
- Hunt, G.R., Ashley, R.P., 1979. Spectra of altered rocks in the visible and near infrared. *Econ. Geol.* 74, 1613–1629. <https://doi.org/10.2113/gsecongeo.74.7.1613>
- Hypex.no/products/disc.php, 2019. Norsk Elektro Optikk AS HySpex VNIR1600 and SWIR320 m-e. Available at: <https://www.hypex.no/products/disc/vnir-1600.php> (Accessed: June 25, 2021).
- Indexdatabase.de/, 2022. index data base. Available at: <https://www.indexdatabase.de/>, (Accessed: May 5, 2022).
- Jackisch, R., Lorenz, S., Zimmermann, R., Möckel, R., Gloaguen, R., 2018a. Drone-borne hyperspectral monitoring of acid mine drainage: An example from the Sokolov lignite district. *Remote Sens.* 10, 385. <https://doi.org/10.3390/rs10030385>
- Jackisch, R., Lorenz, S., Zimmermann, R., Möckel, R., Gloaguen, R., 2018b. Drone-borne hyperspectral monitoring of acid mine drainage: An example from the Sokolov lignite district. *Remote Sens.* 10. <https://doi.org/10.3390/rs10030385>
- Jensen, J.R., 2010. *Remote Sensing of the Environment An Earth Resource Perspective*, 2nd ed. Pearson Education.
- Jordanova, N., 2017. Magnetism of materials occurring in the environment—Basic overview, in: *Soil Magnetism*. Elsevier, pp. 1–28. <https://doi.org/10.1016/B978-0-12-809239-2.00001-2>
- Kirsch, M., Lorenz, S., Zimmermann, R., Tusa, L., Möckel, R., Hödl, P., Booysen, R., Khodadadzadeh, M., Gloaguen, R., 2018. Integration of terrestrial and drone-borne hyperspectral and photogrammetric sensing methods for exploration mapping and mining monitoring. *Remote Sens.* 10. <https://doi.org/10.3390/rs10091366>

- Koerting, F., 2021a. Hybrid imaging spectroscopy approaches for open pit mining - Applications for virtual mine face geology 299. <https://doi.org/https://doi.org/10.25932/publishup-49909>
- Koerting, F., 2021b. Applications for virtual mine face geology. University of Potsdam.
- Kokaly, R.F., 2011. PRISM: Processing Routines in IDL for Spectroscopic Measurements (Installation Manual and User's Guide, Version 1.0=, U.S. Geological Survey Open-File Report 2011-1155.
- Kokaly, R.F., Clark, R.N., Swayze, G.A., Livo, K.E., Hoefen, T.M., Pearson, N.C., Wise, R.A., Benzal, W.M., Lowers, H.A., Driscoll, R.L., Klein, A.J., 2017. USGS Spectral Library Version 7, Data Series. <https://doi.org/https://doi.org/10.3133/ds1035>.
- Köllner, N., Volkmer, G., 2021. Remote Monitoring of Tailings Using Satellites and Drones - Meilenstein 1.
- Kopačková, V., 2014. Using multiple spectral feature analysis for quantitative pH mapping in a mining environment. *Int. J. Appl. Earth Obs. Geoinf.* 28, 28–42. <https://doi.org/10.1016/j.jag.2013.10.008>
- Kopačková, V., Chevrel, S., Bourguignon, A., Rojik, P., 2012. Mapping hazardous low-pH material in mining environment: Multispectral and hyperspectral approaches. *Int. Geosci. Remote Sens. Symp.* 2695–2698. <https://doi.org/10.1109/IGARSS.2012.6350372>
- Kopácková, V., Koucká, L., 2017. Integration of absorption feature information from visible to longwave infrared spectral ranges for mineral mapping. *Remote Sens.* 9, 8–13. <https://doi.org/10.3390/rs9101006>
- Körting, F., 2016. Development of a 360° hyperspectral drill core scanner: Test of technical conditions and validation of high-resolution near-field analysis of crystalline basement rocks using cosc-1 core samples. Masterarbeit, Universität Potsdam.
- Krupnik, D., Khan, S., 2019. Close-range, ground-based hyperspectral imaging for mining applications at various scales: Review and case studies. *Earth-Science Rev.* 198, 102952. <https://doi.org/10.1016/j.earscirev.2019.102952>
- Kruse, F.A., Bedell, R.L., Taranik, J. V., Peppin, W.A., Weatherbee, O., Calvin, W.M., 2011. Mapping alteration minerals at prospect, outcrop and drill core scales using imaging spectrometry. *Int. J. Remote Sens.* 33, 1780–1798. <https://doi.org/10.1080/01431161.2011.600350>
- Kruse, F.A., Lefkoff, A.B., Boardman, J.W., Heidebrecht, K.B., Shapiro, A.T., Barloon, P.J., Goetz, A.F.H., 1993. The spectral image processing system (SIPS)—interactive visualization and analysis of imaging spectrometer data. *Remote Sens. Environ.* 44, 145–163. [https://doi.org/10.1016/0034-4257\(93\)90013-N](https://doi.org/10.1016/0034-4257(93)90013-N)
- Kurz, T.H., 2011. Integration of ground-based hyperspectral and lidar scanning in virtual outcrop geology. PhD Diss. 187.
- Laier, P., 2019. Vale stock plunges after Brazil disaster; \$19 billion in market value lost.
- Lorenz, S., Kirsch, M., Zimmermann, R., Tusa, L., Möckel, R., Gloaguen, R., Str, C., 2018. LONG-WAVE HYPERSPECTRAL IMAGING FOR LITHOLOGICAL MAPPING : A CASE STUDY Helmholtz-Zentrum Dresden-Rossendorf , Helmholtz Institute Freiberg for Resource Technology , TELOPS Inc ., 100-2600 St-Jean-Baptiste Avenue , Quebec City , Quebec G2E 6J5 1620–1623.
- Lottermoser, B., 2010. Mine Wastes, Paper Knowledge . Toward a Media History of Documents. Springer Berlin Heidelberg, Berlin, Heidelberg. <https://doi.org/10.1007/978-3-642-12419-8>
- Louis, J., Debaecker, V., Pflug, B., Main-Knorn, M., Bieniarz, J., Mueller-Wilm, U., Cadau, E., Gascon, F., 2016. Sentinel-2 SEN2COR: L2A processor for users. *Eur. Sp. Agency, (Special Publ. ESA SP SP-*

740, 9–13.

- Lumbroso, D., Davison, M., Body, R., Petkovšek, G., 2021. Modelling the Brumadinho tailings dam failure, the subsequent loss of life and how it could have been reduced. *Nat. Hazards Earth Syst. Sci.* 21, 21–37. <https://doi.org/10.5194/nhess-21-21-2021>
- Mielke, C., Boesche, N.K., Rogass, C., Kaufmann, H., Gauert, C., de Wit, M., 2014. Spaceborne mine waste mineralogy monitoring in South Africa, applications for modern push-broom missions: Hyperion/OLI and EnMAP/Sentinel-2. *Remote Sens.* <https://doi.org/10.3390/rs6086790>
- Mielke, C., Rogass, C., Boesche, N., Segl, K., Altenberger, U., 2016. EnGeoMAP 2.0-automated hyperspectral mineral identification for the German EnMAP space mission. *Remote Sens.* <https://doi.org/10.3390/rs8020127>
- Murphy, R.J., Taylor, Z., Schneider, S., Nieto, J., 2015. Mapping clay minerals in an open-pit mine using hyperspectral and LiDAR data. *Eur. J. Remote Sens.* 48, 511–526. <https://doi.org/10.5721/EuJRS20154829>
- Naden, J., Herrington, R., Jowitt, S.M., McEvoy, F., Williamson, J., Monhemius, J., 2006. BGS Cyprus Report. New methodologies for volcanic- hosted copper sulphide mineralization on Cyprus: A GIS-prospectivity analysis-based approach. *Econ. Miner. Program. Intern. Rep.* CR/06/129 242.
- Nembrini, S., König, I.R., Wright, M.N., 2018. The revival of the Gini importance? *Bioinformatics* 34, 3711–3718. <https://doi.org/10.1093/bioinformatics/bty373>
- Neo.no/, 2022. Norsk Elektro Optikk AS. Available at: <https://neo.no/home/>, (Accessed: May 6, 2022).
- Nordstrom, D.K., 2015. Aqueous Pyrite Oxidation and the Consequent Formation of Secondary Iron Minerals. pp. 37–56. <https://doi.org/10.2136/sssaspecpub10.c3>
- Notesco, G., Kopačková, V., Rojík, P., Schwartz, G., Livne, I., Dor, E. Ben, 2014. Mineral classification of land surface using multispectral LWIR and hyperspectral SWIR remote-sensing data. A case study over the sokolov lignite open-pit mines, the Czech Republic. *Remote Sens.* 6, 7005–7025. <https://doi.org/10.3390/rs6087005>
- Petschick, R., 2002. Röntgendiffraktometrie in der Sedimentologie (K5), in: *Schriftenreihe Der DGG*. pp. 99–118.
- Pieters, C.M., Englert, P.A., 1994. C. M. Pieters and P. A. Englert, Eds. *Remote Geochemical Analysis; Elemental and Mineralogical Composition*. Cambridge (Cambridge University Press), 1993. xxiv + 594 pp., 22 colour plates. Price £60.00. ISBN 0-521-40281-6. *Mineral. Mag.* <https://doi.org/10.1180/minmag.1994.058.393.23>
- Pour, A.B., Hashim, M., 2012. The application of ASTER remote sensing data to porphyry copper and epithermal gold deposits. *Ore Geol. Rev.* 44, 1–9. <https://doi.org/10.1016/j.oregeorev.2011.09.009>
- Prior, T., Giurco, D., Mudd, G., Mason, L., Behrisch, J., 2012. Resource depletion, peak minerals and the implications for sustainable resource management. *Glob. Environ. Chang.* 22, 577–587. <https://doi.org/10.1016/j.gloenvcha.2011.08.009>
- Qian, Y., Zhou, W., Yan, J., Li, W., Han, L., 2014. Comparing Machine Learning Classifiers for Object-Based Land Cover Classification Using Very High Resolution Imagery. *Remote Sens.* 7, 153–168. <https://doi.org/10.3390/rs70100153>
- Richter, R., Schläpfer, D., 2011. Atmospheric / Topographic Correction for Satellite Imagery. *Aerospace* 202.

- Rogass, Christian, Koerting, F.M., Mielke, C., Brell, M., Boesche, N.K., Bade, M., Hohmann, C., 2017. Translational imaging spectroscopy for proximal sensing. *Sensors (Switzerland)*. <https://doi.org/10.3390/s17081857>
- Rogass, C, Koerting, F.M., Mielke, C., Brell, M., Boesche, N.K., Bade, M., Hohmann, C., 2017. Translational imaging spectroscopy for proximal sensing. *Sensors (Switzerland)* 17. <https://doi.org/10.3390/s17081857>
- Rogaß, C., Segl, K., Mielke, C., Fuchs, Y., Kaufmann, H., 2013. Engeomap – a Geological Mapping Tool Applied To the Enmap Mission 1, 94–100. <https://doi.org/10.12760/01-2013-2-02>
- Rouse, J.W., Haas, R.H., Schell, J.A., Deering, D.W., 1973. Monitoring Vegetation Systems in the Great Plains with ERTS. NASA. Goddard Sp. Flight Cent. 3d ERTS-1 Symp. 1, 48–67.
- Safari, M., Maghsoudi, A., Pour, A.B., 2018. Application of Landsat-8 and ASTER satellite remote sensing data for porphyry copper exploration: a case study from Shahr-e-Babak, Kerman, south of Iran. *Geocarto Int.* 33, 1186–1201. <https://doi.org/10.1080/10106049.2017.1334834>
- Silva Rotta, L.H., Alcântara, E., Park, E., Negri, R.G., Lin, Y.N., Bernardo, N., Mendes, T.S.G., Souza Filho, C.R., 2020. The 2019 Brumadinho tailings dam collapse: Possible cause and impacts of the worst human and environmental disaster in Brazil. *Int. J. Appl. Earth Obs. Geoinf.* 90. <https://doi.org/10.1016/J.JAG.2020.102119>
- Swayze, G. a, Clark, R.N., Livo, K.E., Pearson, R.M., 1996. Mapping acid-generating minerals at the California Gulch Superfund site in Leadville, Colorado using imaging spectroscopy. *Nasa* 19980201655 231–234.
- Swayze, G.A., Smith, K.S., Clark, R.N., Sutley, S.J., Pearson, R.M., Vance, J.S., Hageman, P.L., Briggs, P.H., Meier, A.L., Singleton, M.J., Roth, S., 2000. Using imaging spectroscopy to map acidic mine waste. *Environ. Sci. Technol.* 34, 47–54. <https://doi.org/10.1021/es990046w>
- T. Cocks, R. Jenssen, A. Stewart, I.W. and T.S., 1998. The HyMap. October 1–6.
- van der Meer, F., Kopačková, V., Koucká, L., van der Werff, H.M.A., van Ruitenbeek, F.J.A., Bakker, W.H., 2018. Wavelength feature mapping as a proxy to mineral chemistry for investigating geologic systems: An example from the Rodalquilar epithermal system. *Int. J. Appl. Earth Obs. Geoinf.* 64, 237–248. <https://doi.org/10.1016/j.jag.2017.09.008>
- Van der Meer, F.D., De Jong, S.M., 2001. Imaging spectrometry: basic principles and prospective applications, *LibTuDelftNet*. <https://doi.org/10.1007/978-0-306-47578-8>
- van der Werff, H., van der Meer, F., 2015. Sentinel-2 for mapping iron absorption feature parameters. *Remote Sens.* 7, 12635–12653. <https://doi.org/10.3390/rs71012635>
- Yucel, D.S., Yucel, M.A., Baba, A., 2014. Change detection and visualization of acid mine lakes using time series satellite image data in geographic information systems (GIS): Can (Canakkale) County, NW Turkey. *Environ. Earth Sci.* 72, 4311–4323. <https://doi.org/10.1007/s12665-014-3330-6>

ERKLÄRUNG

Ich erkläre, dass ich die vorliegende Arbeit oder Teile davon nicht für andere Prüfungs- und Studienleistungen eingereicht, selbständig und nur unter Verwendung der angegebenen Literatur und Hilfsmittel angefertigt habe. Sämtliche fremde Quellen inklusive Internetquellen, Grafiken, Tabellen und Bilder, die ich unverändert oder abgewandelt wiedergegeben habe, habe ich als solche kenntlich gemacht. Mir ist bekannt, dass Verstöße gegen diese Grundsätze als Täuschungsversuch bzw. Täuschung geahndet werden.

Berlin, den _____

Unterschrift _____

8 Appendix

8.1 Further Methods

8.1.1 The HySpex camera system

The hyperspectral images of the laboratory data sets were taken using the HySpex spectrometer system from the company *Norsk Elektro Optikk AS* (Neo.no/, 2022). The system is a line scanner that records a surface line by line. By using two sensors, the imaging system can generate an image that represents the spectrum of the wavelength range 400 - 2500 nm in each pixel. The configuration and sensor settings were determined via the associated *HySpex Ground* and *HySpex Rad* software for the measurements. The following technical information and functionalities have been taken from the *Norsk Elektro Optikk AS HySpex VNIR1600* (measuring range 400 - 1000 nm) and *SWIR320 m-e* (measuring range 1000 - 2500 nm) user manual (Hyspex.no/products/disc.php, 2019).

The laboratory setup (Figure 43) of the HySpex system consists of a framework in which the two hyperspectral sensors *HySpex-VNIR 1600* and *HySpex-SWIR 320m-e* are aligned vertically facing downwards. The measuring field of the line scanners points to a table that allow lateral motion of the samples underneath the cameras (translation stage). This translation stage moves slowly underneath the sensors during the recording, so that they can record the objects on the translation stage line by line.

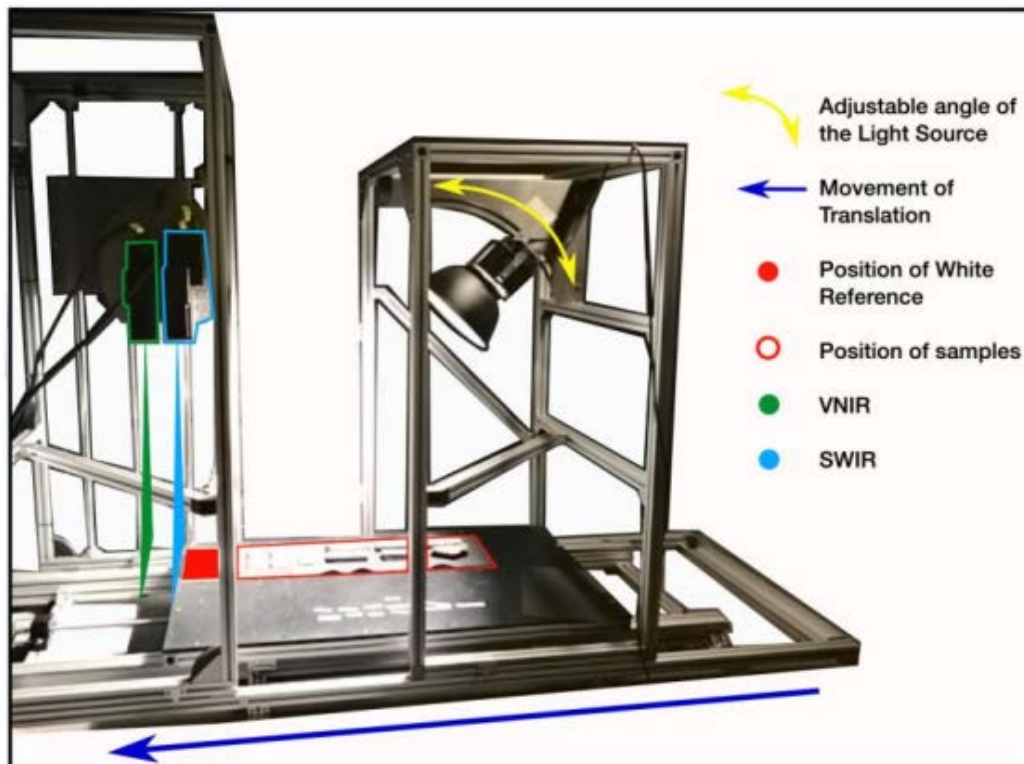


Figure 43 Laboratory setup of the spectrometer with HySpex sensor technology, from Körting, 2016

8 Appendix

The samples are arranged on the translation stage. Depending on the quantity and size of the samples to be measured, the distance of the sensors to the object under examination can also be changed. This, and appropriate lenses, ensure sufficient spatial resolution. Uniform illumination is ensured by a light source mounted at a 45° angle, which is placed at a distance of 1 m. Next to the samples, a white reference plate is positioned that is used as a reflectance calibration target. With the help of the white reference in the image, the radiance data can be converted into reflectance data in the subsequent processing procedure. Due to the high reflection behaviour of the white reference, it should be positioned as far away as possible from the samples in order to prevent influences on the samples. The reflectance factor of the white reference is selected depending on the albedo of the sample (reflectance of a diffuse surface) is selected. Reference targets with the following percentages of reflection factor were available: 5%, 20%, 50%, 90% and 95%.

In order to achieve a good measurement, the integration time of the scan should be as high as possible to allow for optimal illumination of the sample and a high energy flux from the sample surface to the sensor. However, there should be no oversaturation of the area (Bade, 2016). To protect against external factors such as stray light from windows, the room is darkened, surfaces painted in black, and the samples themselves are positioned on foam rubber of low reflectivity and low spectral albedo. This dark foam rubber plate reflects only weakly (Herrmann, 2015). Detailed descriptions of the laboratory settings and experimental procedures were presented in papers by Herrmann, 2019; Körting, 2016; C Rogass et al., 2017.

8.1.2 Principle of X-ray diffractometry (XRD)

The field samples were analysed by X-ray diffractometry for mineral identification. This was done at the Institute of Geosciences at the University of Potsdam. In the following, the principle of XRD analysis will be briefly explained. The samples must be processed into homogenised rock powders before measurement. With XRD analysis, crystalline substances can now be made visible. The crystal grids of the samples diffract the X-rays in a characteristic way when irradiated (Petschick, 2002). The radiation source is an X-ray tube (Figure 44). The diffraction angle is recorded at different angles of the radiation entrance (theta angle) (Figure 44). To make all phases of the rock powder visible, the diffracted radiation is measured at all angles. The result is a diffractogram ("diffraction angle dispersive XRD profile") (Figure 46 - Figure 53).

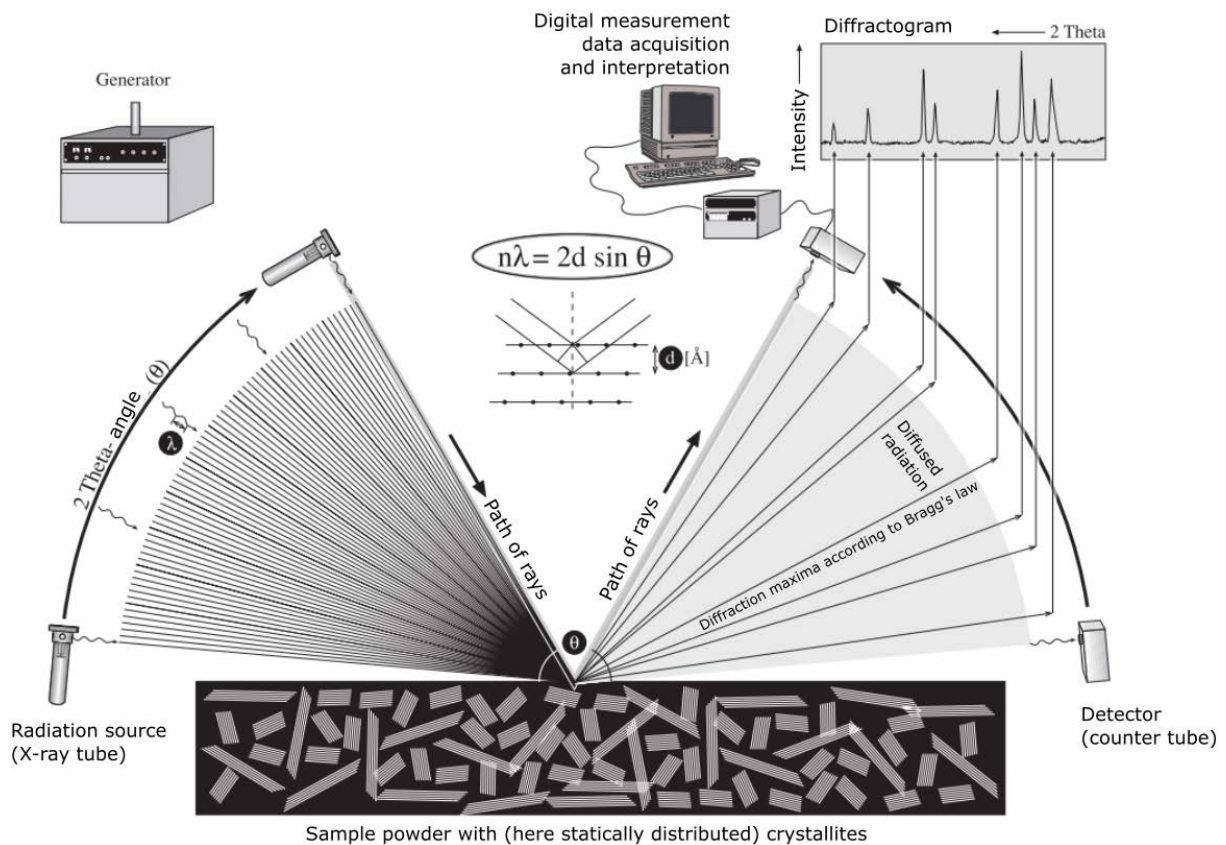


Figure 44 Principle of diffractometry and Bragg's relation in the optical path of a diffractometer and derivation of a diffractogram, from Petschick, 2002

8.1.3 XRD diffractograms of validation samples

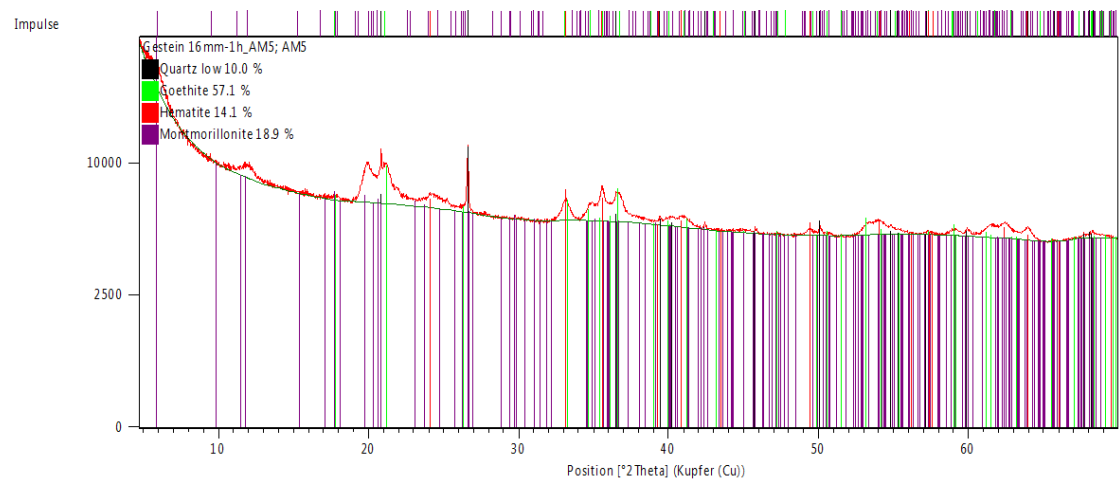


Figure 45 XRD results of sample AM5

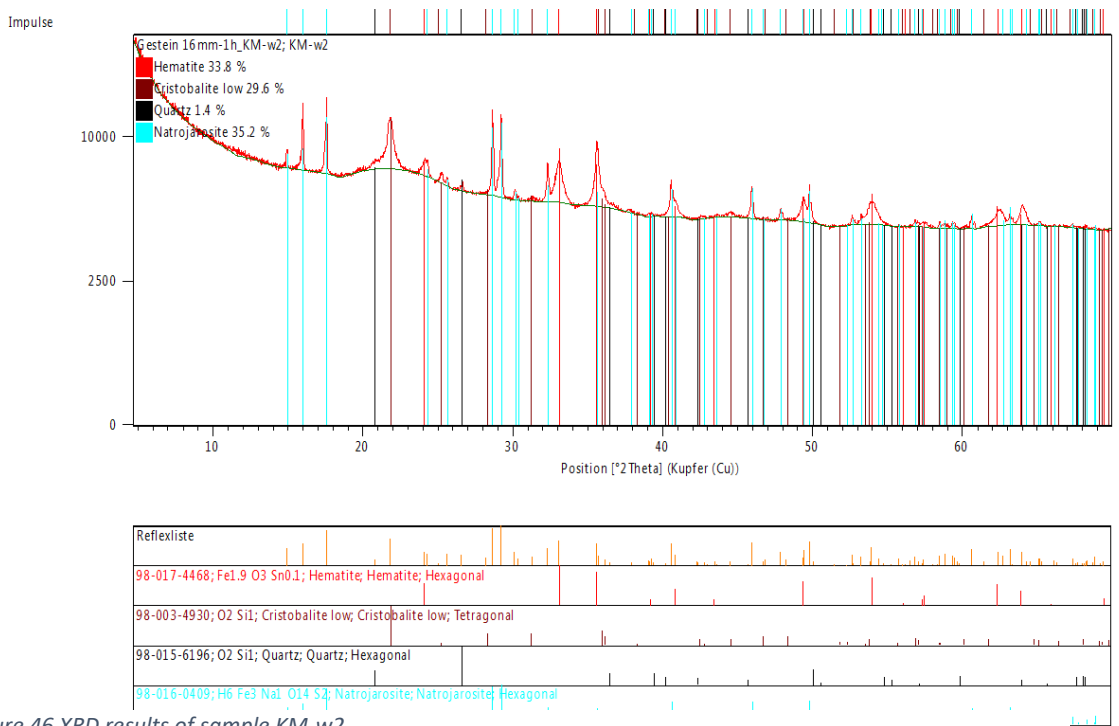


Figure 46 XRD results of sample KM-w2

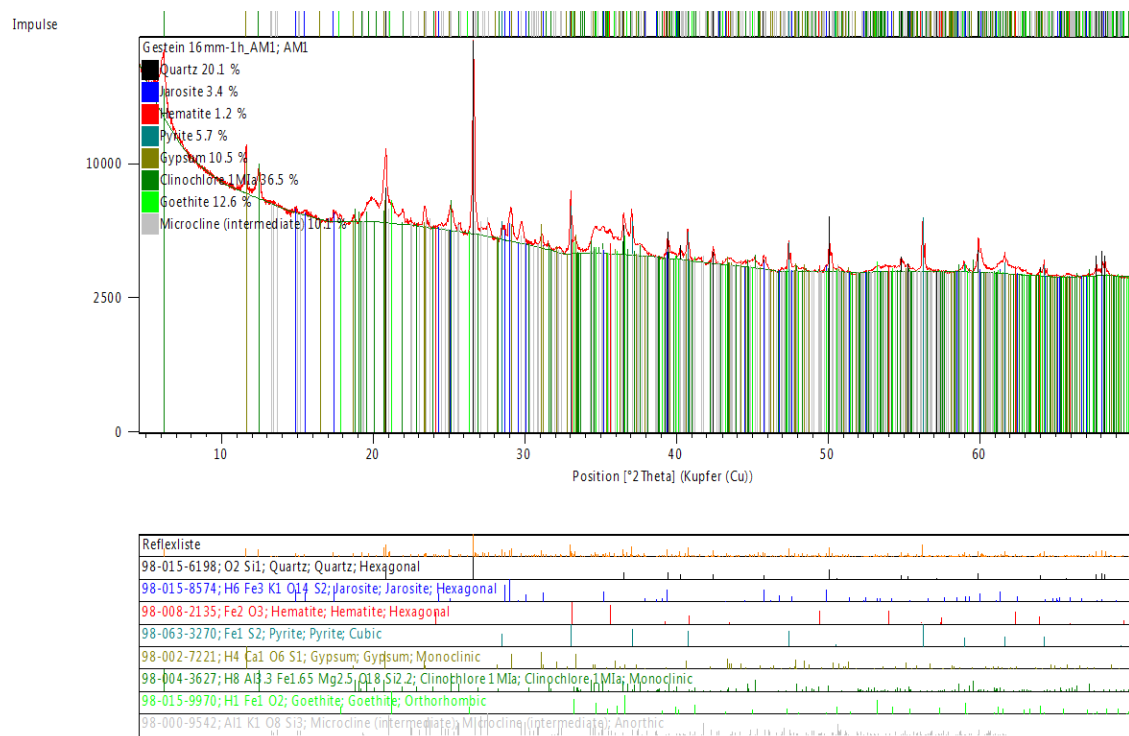


Figure 47 XRD results of sample AM1

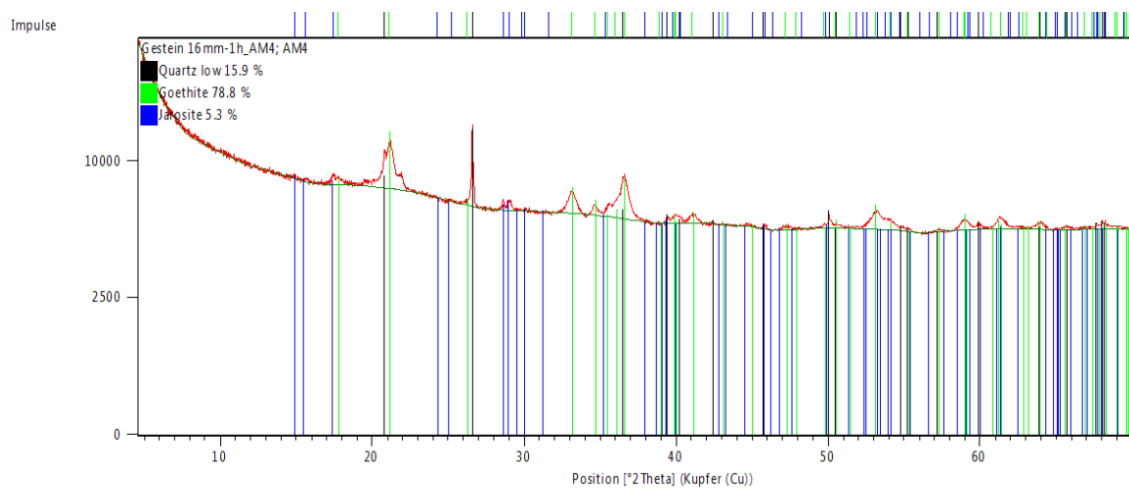


Figure 48 XRD results of sample AM4

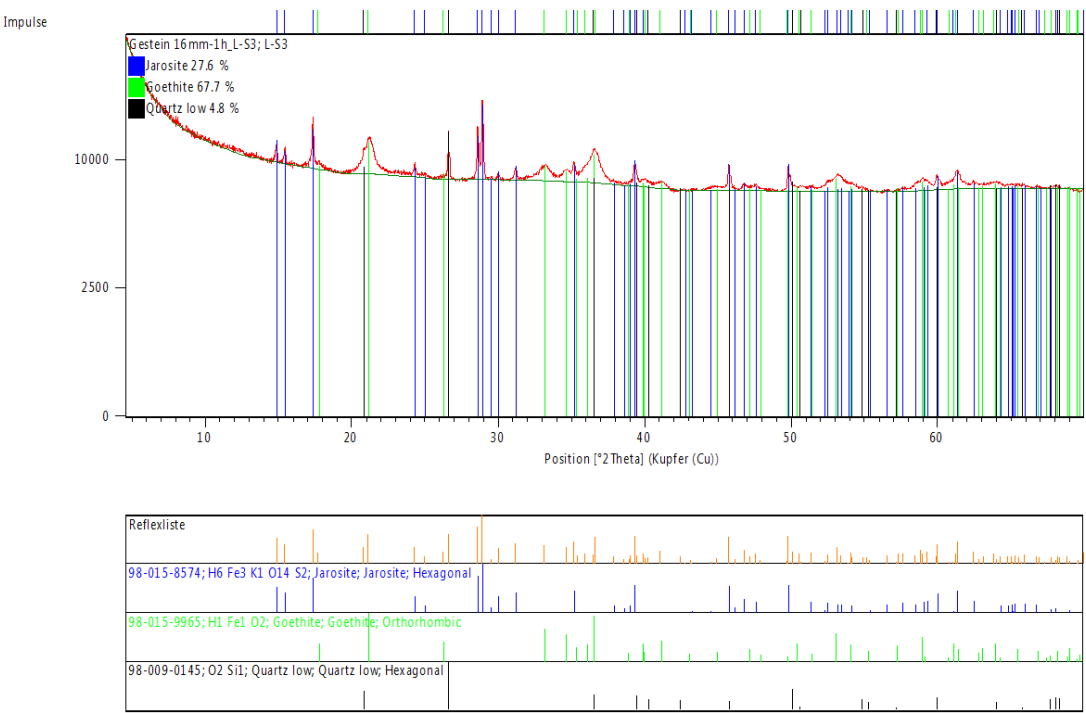


Figure 50 XRD results of sample L-S3

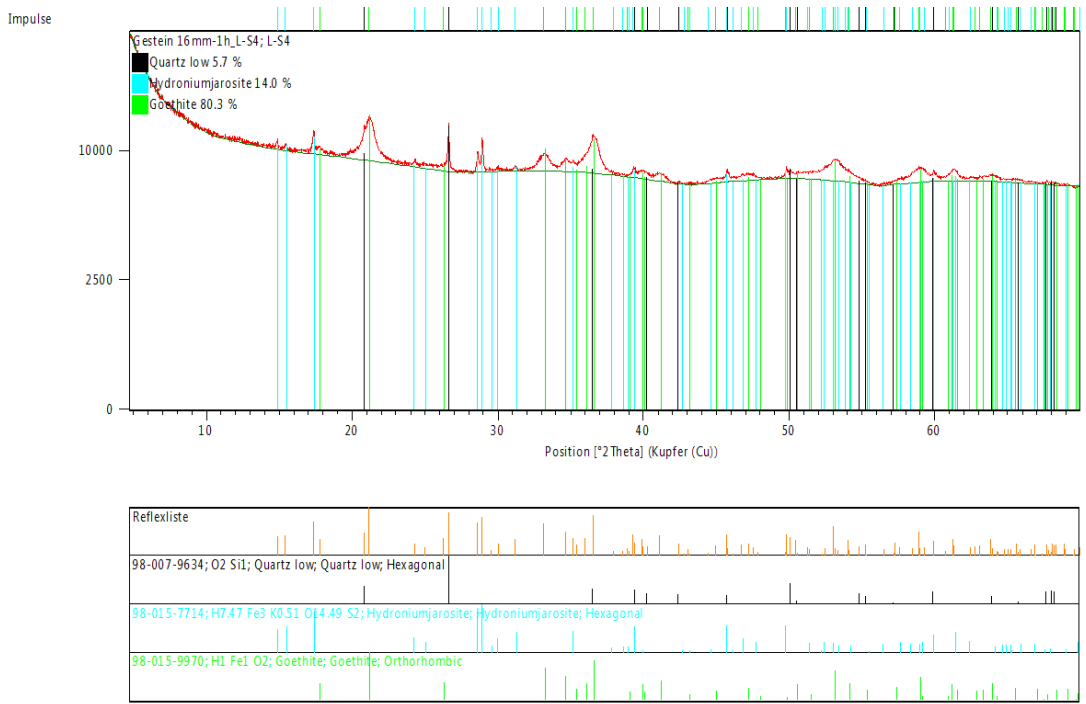


Figure 49 XRD results of sample L-S4

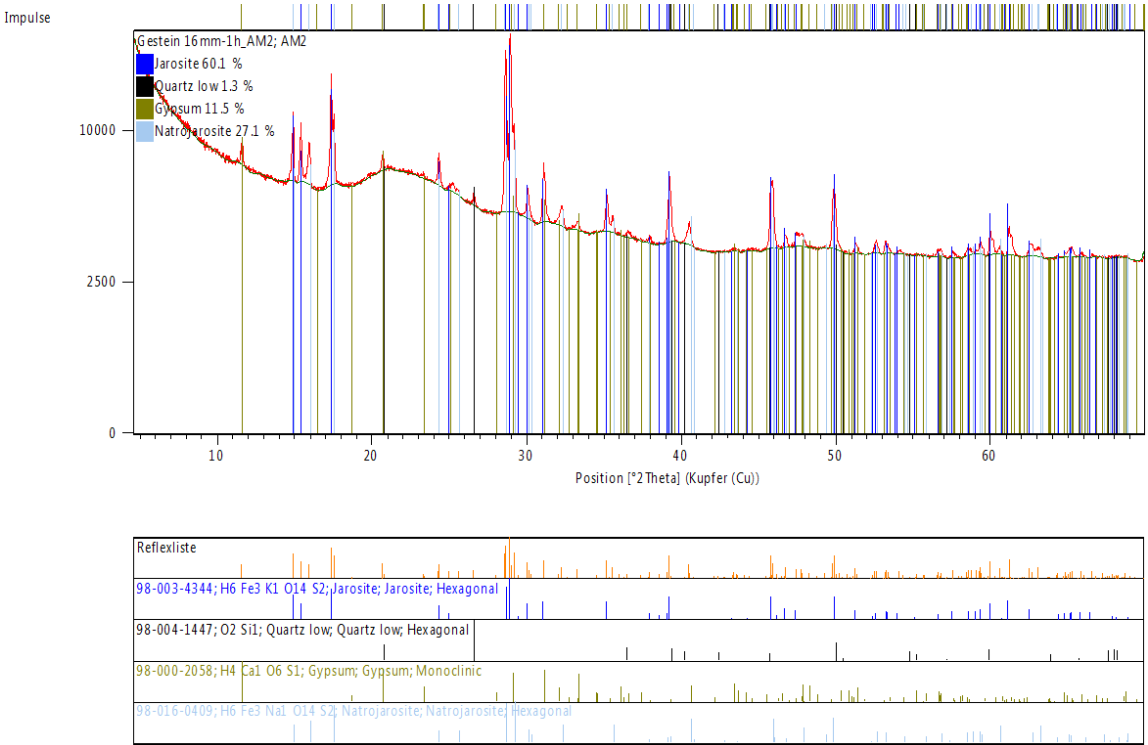


Figure 52 XRD results of sample AM2

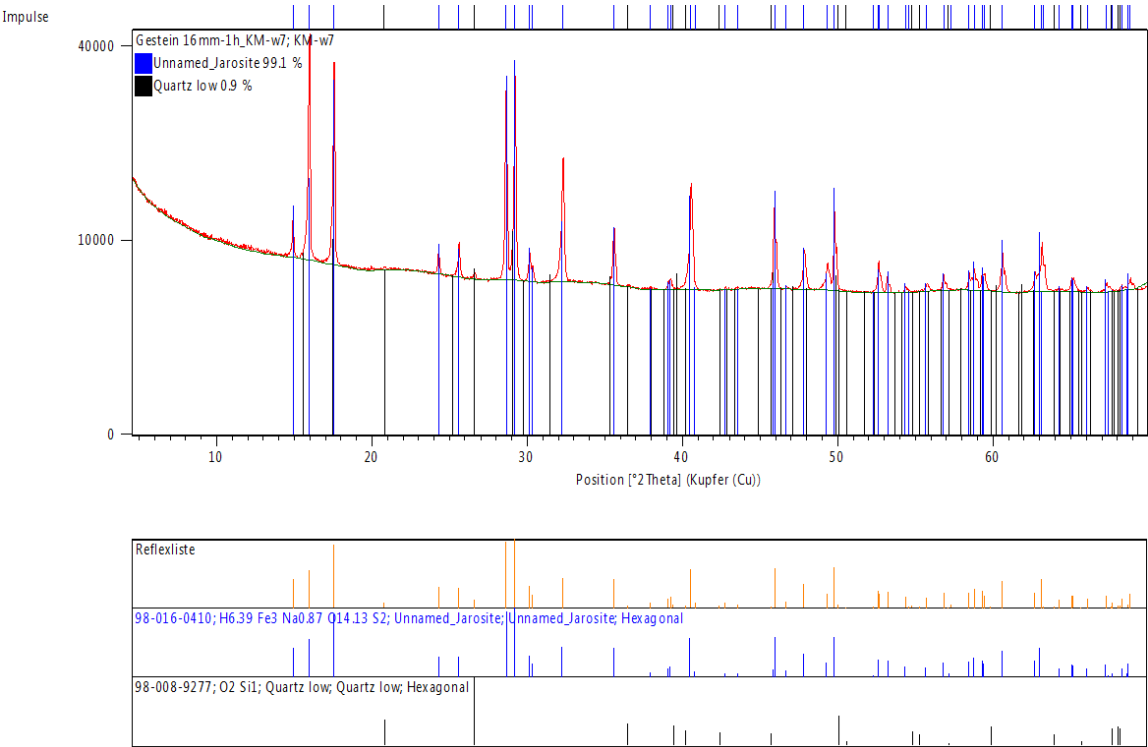


Figure 51 XRD results of sample Km-w2

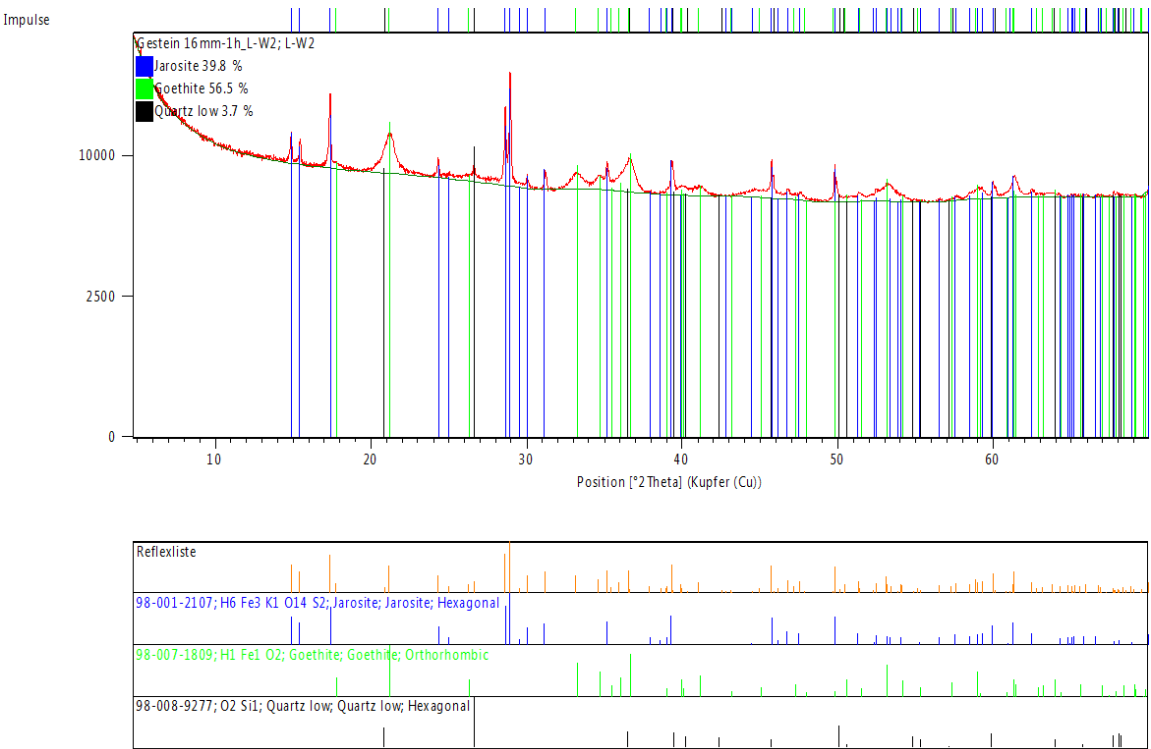


Figure 53 XRD results of sample L-w2

8.2 Additional Datasets

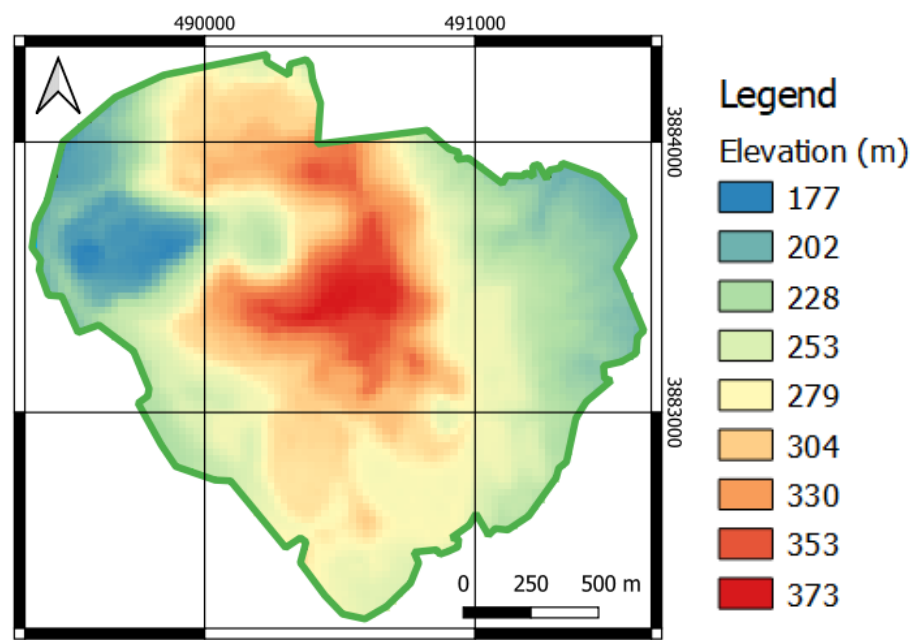


Figure 54 Digital Elevation Model (DEM) of the Skouriotissa mine. From: Charalambos, 2016a

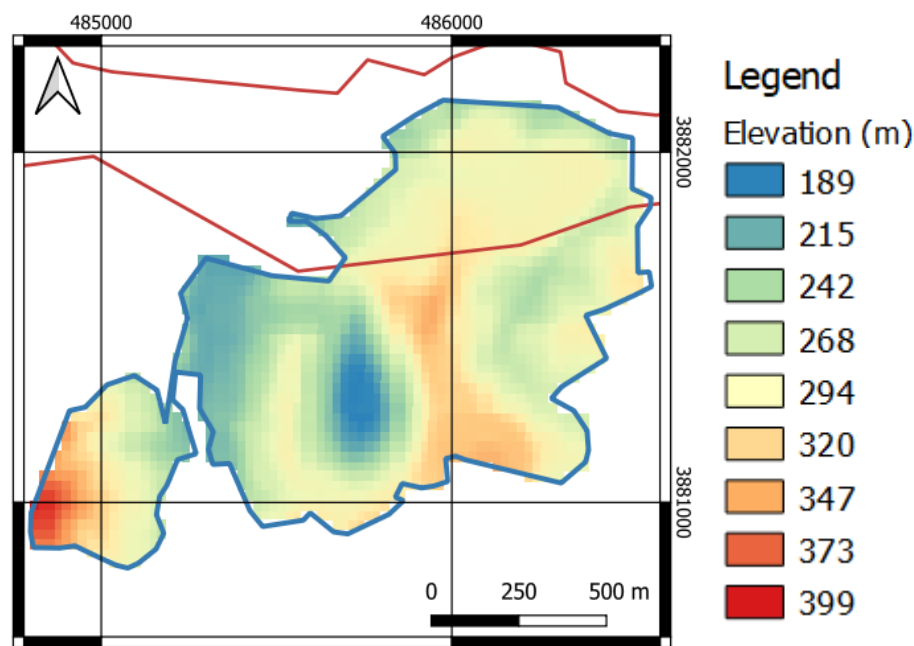


Figure 55 Digital Elevation Model (DEM) of the Apliki mine. From: Charalambos, 2016b

8.3 Additional Data (Results)

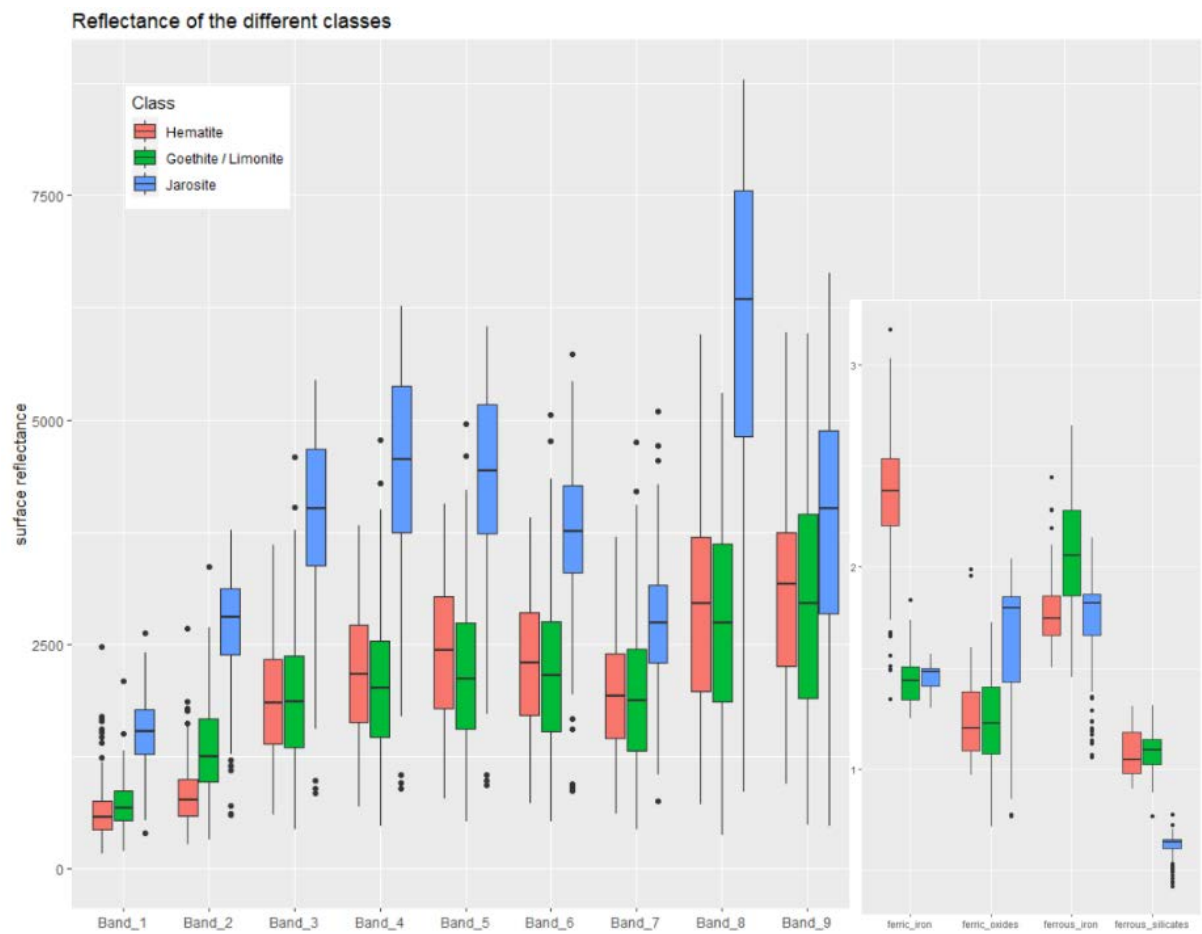


Figure 56 Boxplots of the reflectance of the different sensor bands and indice layers for the three chosen classes for Sentinel-2 resolution (9 Bands + 4 layers).

Table 16 Overview of estimated area sizes of the different classes and sensors, displayed as pixel count per class.

	Total area			Skouriotissa area			Apliki area		
WorldView-3	low	high	total	low	high	total	low	high	total
Hematite	11448	5263	16711	7943	3871	11814	1858	568	2426
Goethite/Limonite	12518	6475	18993	8315	5149	13464	2874	762	3636
Jarosite	20713	12578	33291	13804	11141	24945	2359	448	2807
Sentinel-2	low	high	total	low	high	total	low	high	total
Hematite	114	22	136	93	20	113	14	1	15
Goethite/Limonite	803	153	956	509	69	578	197	52	249
Jarosite	1493	683	2176	1416	664	2080	42	8	50

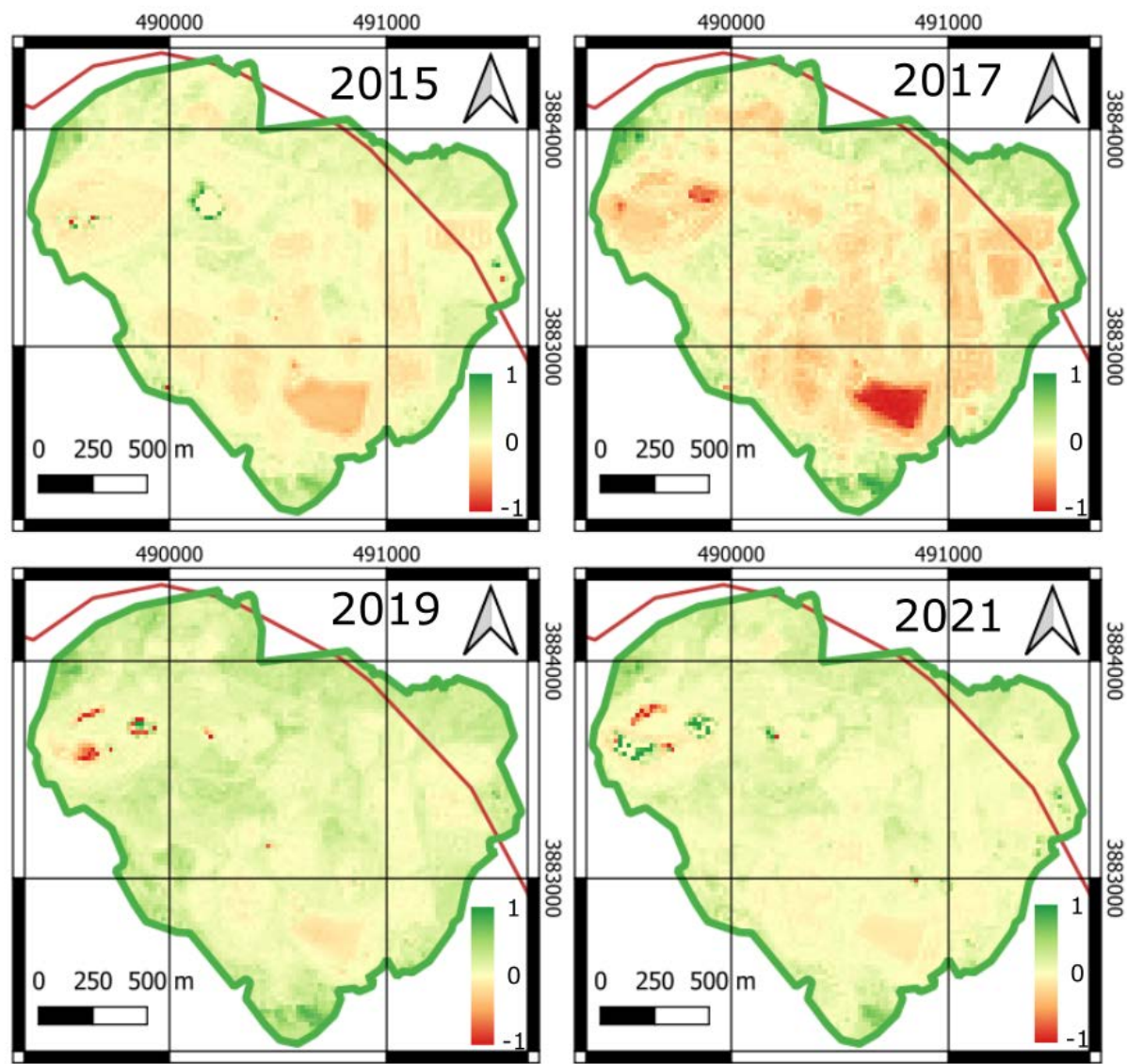


Figure 57 NDVI of the Sentinel-2 images from the years 2015, 2017, 2019 and 2021

8.4 Additional Data (Outlook)

Table 17 List of metadata for the Sentinel-2 satellite images used in the time series analysis

Year	Date	Tile Number	File Name / Tile Name
2015	12.08.2019	T36SVD	L1C_T36SVD_A000733_20150813T083848
2017	12.08.2017	T36SVD	L1C_T36SVD_A011172_20170812T083633
2019	12.08.2019	T36SVD	L1C_T36SVD_A021611_20190812T083557
2021	11.08.2021	T36SVD	L1C_T36SVD_A032050_20210811T083527



ISSN 2190-7110